Polymer dye lasers

Balslev, Søren; Kristensen, Anders

Publication date:
2006

Document Version
Publisher's PDF, also known as Version of record

Polymer dye lasers

Søren Balslev
Ph.D. Thesis

MIC – Department of Micro and Nanotechnology,
Technical University of Denmark (DTU),
Building 345east, Ørsteds Plads,
DK-2800 Kongens Lyngby.
www.mic.dtu.dk/research/NIL
E-mail: sba@mic.dtu.dk

January 31, 2006

Abstract

The purpose of this project has been to develop miniaturized polymer dye lasers that can be integrated on microchips containing other polymer "laboratory on a chip" circuitry. The envisioned function of the polymer dye lasers has been to deliver light for sensing purposes, either for wavelength dependent absorption or for interference based sensing, for example with integrated Mach-Zehnder interferometers.

In order to develop this kind of lasers, the project has focused on using a single transparent type of resist (SU-8) that can be patterned via several methods. The methods that have been tried on this resist are UV lithography, electron beam lithography and X-ray lithography. Apart from SU-8, a few alternative polymer types have also been used for forming laser structures via nanoimprint lithography.

Throughout the work, several laser resonator types have been fabricated in polymer materials. The resonators range from simple parallel mirror types to first order Bragg grating distributed feedback resonators. Through the optical characterization of the laser type range, the possibilities for forming such miniaturized polymer dye lasers are revealed.

Some techniques for modelling micro-optical structures are presented as a suggestion of how to predict the behavior of miniaturized polymer dye lasers and micro-optical structures in general.

Both lasers operating in multi-mode and single polarization lasers operating on pre-determined single mode wavelengths are demonstrated. The mode structure of the lasers are controlled by the design of the laser resonators.

Integration of a miniaturized polymer dye laser is demonstrated in two examples where the laser delivers light to an absorption cell, which makes it possible to measure the wavelength selective absorption of the fluid in the cell.

The findings presented in the thesis forms a basis for selection of laser design for new applications both with respect to integration and to further development of polymer dye laser light sources.

Resumé

Formålet med dette projekt har været at udvikle miniaturiserede polymerfarvestoflasere som kan integreres med andre polymer-komponenter på chips indeholdende laboratoriefunktioner, også kaldet "laboratorie-på-en-chip". Funktionen med farvestoflaserne skal være at levere lys til sensorer, enten til bølgelængdeafhængig absorptionsmåling eller til inteferensbaserede sensorer, som for eksempel med et Mach-Zehnder interferometer.

For at udvikle denne type lasere, har projektet fokuseret på at anvende en bestemt type transparent resist (SU-8) hvori strukturer kan defineres med flere forskellige metoder. De metoder som har været anvendt i udviklingen er UV-litografi, elektronstråle-litografi og Röntgenstråle-litografi. Bortset fra SU-8, er et par andre alternative polymertyper afprøvet i forbindelse med fabrikering af lasere via "nanoimprint"-lithografi.

Gennem arbejdet, er adskillige lasertyper blevet fabrikeret i polymer materialer. Resonatorerne strækker sig fra simple typer som baserer sig på to parallele spejle, til typer som baserer sig på distribueret tilbagekobling fra første ordens Bragg-gitre. Gennem den optiske karakterisering af de forskellige lasere, er mulighederne for at fabrikere miniaturiserede polymer-farvestoflasere blevet afdækket.

Teknikker til at modellere mikro-optiske strukturer er præsenteret som foreslag til hvordan opførselen af laserne kan forudsiges. Teknikkerne er for en del også anvendelige til andre mikro-optiske strukturer.

Både lasere som fungerer på flere bølgelængder samtidig (multi-mode) og lasere som fungerer på en enkelt bølgelængde demonstreres. Alle laserlyskilderne er enkeltpolariseret. Den spektrale struktur af de optiske resonatorer kontrolleres via designet af resonatorerne for at opnå lasing på en enkelt bølgelængde.

Integration af de miniaturiserede farvestoflasere er vist i to eksempler, hvor laseren leverer lys til en vædskeabsorptioscelle. Disse systemer gør det muligt at måle absorptionen af en nyblandet vædske ved en enkelt bølgelængde.

Resultaterne danner et grundlag for at vælge hvilken type laser som vil være optimal i nye applikationer, og danner også grundlag for yderligere udvikling af miniaturiserede polymer-farvestoflasere.

Preface

This thesis is submitted as a partial fulfillment of the requirements for obtaining the Ph.D. degree from the Technical University of Denmark (DTU). The research reported has been conducted at the Department of Micro- and Nanotechnology (MIC) at DTU in the period from February 2003 to January 2006. The project has been supervised by Associate Professor Anders Kristensen and financed by a grant from the Danish Technical Research Council (Statens Teknisk-Videnskablige Forskningsråd (STVF) (grant No. 26-02-0064)).

This project would not have been possible without the help from numerous people. First of all I would like to thank my supervisor Anders Kristensen who through enthusiasm, encouragement and insight into physics has been an outstanding $\mu\alpha\acute{\iota}\epsilon\upsilon\sigma\iota\varsigma$.

I would like to thank my fellow Ph.D. students, Brian Bilenberg, Mads Brøkner Christiansen, Morten Gersborg-Hansen, Søren Jensen, Theodor Nielsen and Daniel Nilsson for good collaboration in our different projects and for a pleasurable atmosphere in the offices.

During the Ph.D. work I have co-supervised a number of student projects. All students have worked hard end enthusiastically and have contributed significantly to lift the workload within the research group under Anders Kristensen.

I would like to thank Niels Asger Mortensen for many discussions on optical behavior of microstructures.

Everyone at MIC should be thanked for making the stay at the department enjoyable and for providing a free and open atmosphere with many fruitful interdisciplinary discussions.

The people at DANCHIP have shown excellent service and ever-readiness to offer help and advice.

From outside MIC, I would especially like to thank Filippo Romanato for his helpfulness, enthusiasm and knowledgeable advice regarding X-ray lithography, and for making it possible for me to perform experiments at the ELETTRA synchrotron light source in Trieste, Italy.

Finally, I would like to thank my family and friends for all their support.

Lyngby, 31.01.2006

Søren Balslev

Contents

Chapter 1

Introduction

1.1 Micro-devices

Micro-devices have penetrated consumer products especially within the field of electronics, but also lately within the field of electro-mechanical sensors, such as acceleration sensors and flow and pressure sensors, some of which are now found as common elements in everyday automobiles. In micro-technology, products are reduced to components that may comprise new products with complex functionality. The revolution of micro-devices in consumer or medical products that has extended to the successful field of micro-electronics and micro-mechanics, has not yet involved micro-fluidics and opto-fluidics. Several research groups around the world, are currently engaged in projects focusing on examining the possibilities within the areas of micro-fluidics and opto-fluidics (for example [1]). Only few have turned their attention to laser light sources for integration with such systems.

Parallel planar fabrication techniques are being developed in order to fabricate micro fluidic and optical circuits in polymer with good success [2, 3]. This development relies on new materials, such as optically transparent resists [4, 5], and new fabrication methods, in particular nano-imprint lithography using thermoplastic polymers [6]. The new materials and methods, allow for fast parallel fabrication of micro and nano-structures in polymer, without using mechanical machining or slow serial processing, such as in electron-beam lithography.

"Lab-on-a-chip" (LOC) systems is a concept developed to describe chip size systems that can perform a similar function as would normally be carried out in a standard full size laboratory (see Figure 1.1) [7]. Usually the chips are dedicated to a specific process, such as for example DNA amplification [8]. The rationale behind such a miniaturization is the improvement in efficiency that would be achieved in many medical and biological laboratory functions if the laboratory – in effect – could be brought to the point of care, instead of shipping biological samples to geographically fixed laboratories. The advantage is obvious when considering disaster areas where the normal infrastructure is damaged, or health care in remote locations. For these kinds of applications however, it is of paramount

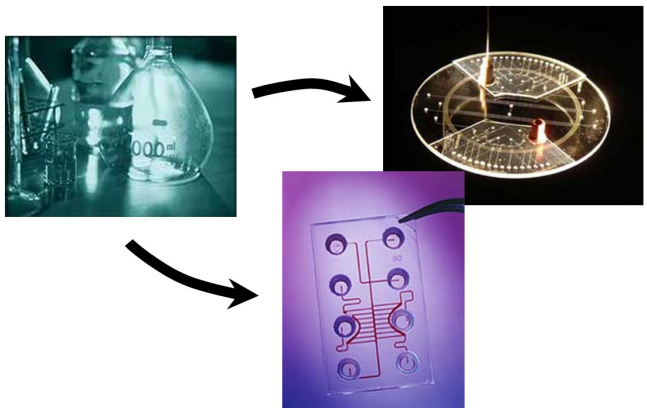

Figure 1.1: The concept of lab-on-a-chip systems is to replace laboratory equipment such as beakers etc. with small chips that has the same functionality as a macroscale laboratory procedure.

importance that the LOC devices are easy to manufacture and therefore cheap. Also they must be easy to use, and not require lengthy training of the users.

There are two practical ways to apply LOC circuitry; as a fixed part of an apparatus or as a short lifetime exchangeable component. Fixed integrated micro components are found in common electronic equipment such as computers in the form of microchips, while exchangeable components with short lifetimes are found for example in ink-jet printers, where the disposable ink-cartridge contains a complete micro-structured print head. A third way of application of the LOC principle is found in completely self-contained LOC circuits that include components for sample input and read-out of the result of the analysis. This last system type is not practically realizable with today's state of the art LOC technology.

Since laboratory procedures often involve many kinds of equipment, a good toolbox for LOC circuits should contain transducers of many kinds, along with tools for guiding energy and matter flow (fluids). In order to keep production cost low, it is advantageous to form these components in polymer, so to avoid the higher cost of working with silicon or other hard materials. If possible, the components should be definable in a single layer of polymer. Energy and material flow can be handled by wave guides and micro fluidic channels, which are fairly easy to fabricate in polymer. Many other component tools for LOC circuits are under development, such as micro pumps, light absorption cells, valves, mixers, heaters etc.

A component which has found widespread use in laboratory equipment for sensing purposes is the laser. It has found its use in for example flow cytometers. Therefore developing lasers for integration in LOC circuits, is an obvious step to expand the LOC toolbox. Access to high quality laser light on-chip, opens up a range of possible sensing methods than can be used in LOC circuits, from spectrally resolved absorption measurements to highly sensitive interference based sensing.

When choosing the type of lasers to use with lab-on-a-chip devices based on polymer, the demand for very low price and ease of use excludes semiconductor lasers

due to two factors. Firstly, hybridizing semiconductor lasers with polymer LOC circuits requires alignment in the hybridization step, along with the need to fabricate electrodes on the chip (if the semiconductor laser is pumped electrically). This increases the price considerably compared to an all polymer system, since an alignment process step for each component device is costly in production. Secondly, another obvious solution is to couple semiconductor laser light into the chip via butt coupling of fiber wave guides or provide other means of coupling the light into wave guides on the chip, for example by using a grating coupler or a prism coupler. However, both methods require minute alignment in the micrometer range in situ when the chip is to be used. This violates the requirement of ease of use, if the chip has to be replaced at any point.

The challenge which has been addressed in the work described in this thesis has been to design and investigate lasers for polymer LOC circuits. Some of the main challenges that have been addressed are: How to fabricate a laser in a simple planar fabrication process; how to define the optical resonator solely in polymer and how to ensure lateral output from the laser. Finally, the lifetime of the devices and the ease of operation has been addressed.

Designing the lasers so they can be fabricated in a planar process is important since this makes it possible to fabricate the devices in parallel. Parallel processing is a key point for all micro fabrication, since it allows a low production price for each individual device. The type of lab-on-a-chip circuits with which the lasers should be integrated are themselves fabricated with planar processes.

In order to make as simple laser light sources as possible, the laser resonators should optimally be defined in a single layer of polymer. The feedback in the resonator should not be owed to metallic or dielectric layer mirrors, as is often a good solution for macroscopic lasers and optics, since such mirrors require more process steps in fabrication. This thesis examines the use of different feed back mechanisms using structures formed in a single layer of polymer.

Light guides on typical LOC circuits allow for lateral propagation of light along the chip plane. Therefore it is necessary that the laser light source emits laterally and that the output from the laser is of a suitable nature for coupling into wave guides on the chip. This issue will be discussed for the different laser architectures.

Considering that the objective has been to develop laser light sources for simple use on cheap LOC circuits, operating the laser in the field should be easy and not require expensive and large equipment. With the organic dye lasers concerned in this thesis, the method of pumping the lasers is the main issue regarding ease of use in the field, since the lasers must be pumped optically. However, optical pumping of the lasers also has advantages with respect to component price, since no on-chip electrical circuitry or electrodes are required.

The approach taken in this Ph.D. work has been to examine various kinds of laser resonator types, and various lithographic techniques, in order to identify practical solutions for on-chip LOC lasers. This work was ab initio based on the work done by B. Helbo [9], S. Kragh [10], B. Bilenberg [11] and A. Kristensen at MIC – Department for Micro and Nanotechnology at the Technical University of

Denmark (DTU). The foregoing work by B. Helbo, S. Kragh, B. Bilenberg and A. Kristensen concerned the demonstration of multimode miniaturized dye lasers based on metallic mirrors and total internal reflection.

1.2 The path to miniaturized polymer dye lasers

The first laser was made by Theodore H. Maiman in 1960 by using a flash lamp pumped rubidium rod with mirrors at each end (see Figure 1.2) [12]. Since then, laser technology has developed enormously and is today both used in everyday household items and in fundamental research laboratories. The importance of the laser is immense, and lies in the nature of the emitted light, which is in general collimated, intense, coherent and monochromatic.

The realization of the laser has enabled entirely new kinds of light-based sensors based on interference, such as the Mach-Zehnder interferometer, and based on monochromaticity, such as polarization spectroscopy. These kind of sensing techniques are impossible or at best, rather cumbersome to perform using incandescent or arc light. Using lasers, the techniques have made it possible to determine minute changes in length, refractive index, details in molecular electronic transitions and the distance to the moon. The widespread use of lasers today is a testimony to the usefulness of laser based detection systems, which is also the motivational foundation for the work dedicated to develop cheap polymer based light sources for LOC type systems.

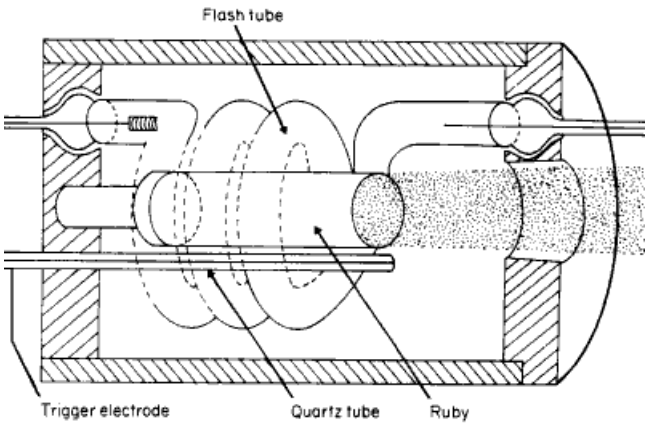

Figure 1.2: Sketch of the first laser which was based on a flash lamp pumped ruby rod with metallized end faces (reproduced from [12]).

After the demonstration of the first laser, the field quickly developed in multiple directions, giving rise to a wide range of laser types. Below are given some main milestones within the field of experimental laser physics, that has formed the path to miniaturized polymer dye lasers.

In 1966 Sorokin and Lankard demonstrated the first lasing from a dye (chloroaluminum-phthalocyanine) pumped by a Q-switched ruby laser (see Figure 1.3) [13]. The laser operated at 755 nm and used an ethanolic solution of the dye in a glass

cell. The fluid cell was placed in a macroscopic optical resonator consisting of two flat dielectric mirrors. Later, in 1967, Sorokin and Lankard also demonstrated lasing with an organic dye solution pumped by a flash lamp [14]. The demonstration of direct flash lamp pumping of dye lasers is an important step, since dye laser systems thus can become much simpler, when they do not need to be pumped by another laser.

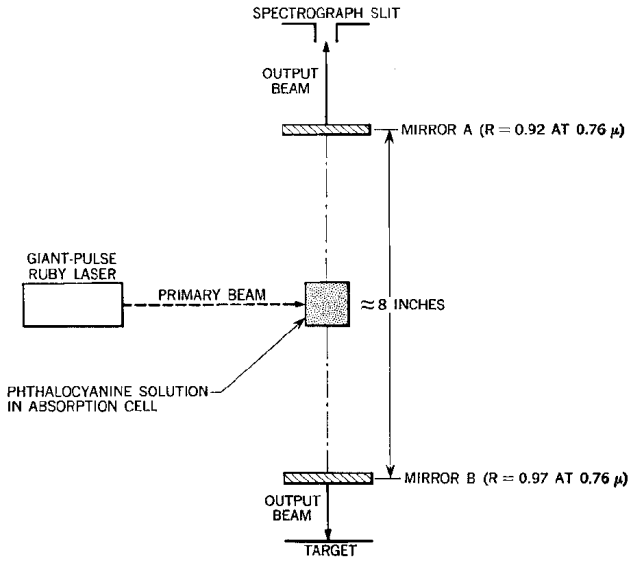

Figure 1.3: Sketch of the first organic dye laser using a phthalocyanine solution (reproduced from [13]).

Soffer and McFarland obtained stimulated emission of Rhodamine embedded in PMMA in 1967 [15], and shortly thereafter Peterson and Snavely demonstrated lasing in a flash lamp excited Rhodamine 6G doped PMMA rod [16]. The external laser resonator consisted of two flat aluminum mirrors. The fact that dyes embedded in solid polymer matrices such as PMMA still are optically active with respect to stimulated emission, opens up possibilities for laser resonator designs that are not possible if the gain medium has to be a fluid.

Using dye doped polymer for a miniaturized resonator on a chip, was done only much later by Hu and Kim in 1976 [17]. The laser by Hu and Kim was formed in a Si wafer by etching a rectangular hole in the Si and spin-coating a dye doped polymer (Rhodamine 6G in polyurethane) onto the wafer. The resonator was formed by the reflective Si surfaces and the light coupled out of the resonator through a thin film covering the structure (see Figure 1.4). The laser was multimode and was pumped by a Nitrogen laser (337 nm). This important early work demonstrated the feasibility of using small chip based optical resonators and organic dye as gain material to make lasers.

Free standing hexagonal micro resonators based on the refractive index difference between air and the dye doped polymer itself (PMMA), was only demonstrated as late as the year 2000 by Sasaki et al. (see Figure 1.5) [18]. In their work, Sasaki et al. used the total internal reflection originating from the polymer-air interface to create the feedback. A year later (2001) the same group demonstrated lasing

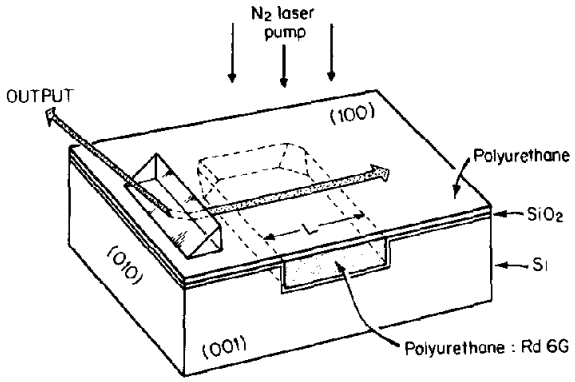

Figure 1.4: Sketch of the first laser based on a miniaturized resonator defined on a silicon chip. L is 1.05 mm and the resonator is 8.4 µm thick (reproduced from [17]).

in squares of dye doped polymer based on the same principle as their previous work (see Figure 1.6) [19]. However the polymer micro cavities were not created with an integrated out-coupling mechanism for the light, and the measurements were carried out on scattered light from the devices.

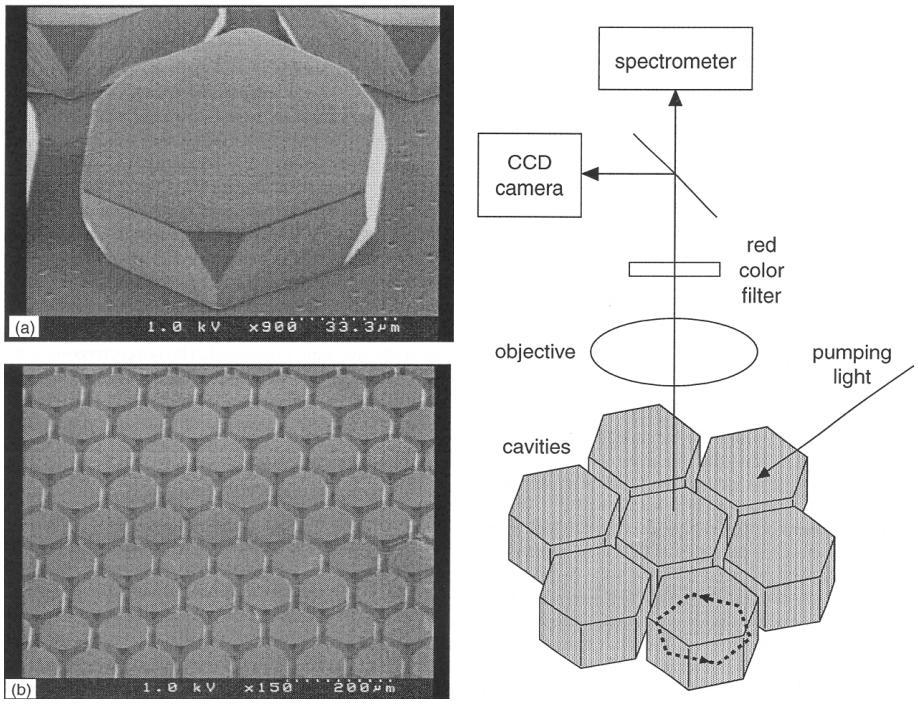

Figure 1.5: Left: Microstructured hexagonal resonators formed in dye doped PMMA. Right: Principle of operation and measurement the hexagonal resonators (reproduced from [18]).

The few publications to have come out on this type of lasers, reflect the waning interest in solid state polymer lasers. The lack of interest stems mainly from the realization that the lifetime of individual components is limited due to bleaching of the dye, and from the fact that the lasers need to be pumped optically in pulsed mode which requires an intense pulsed light source. These are drawbacks that

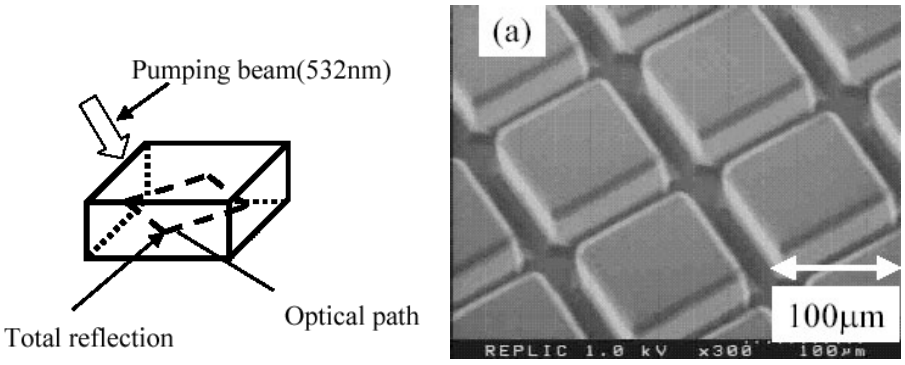

Figure 1.6: Left: Operational principle of square resonators in dye doped polymer. Right: Electron microscope image of realized dye doped PMMA resonator array (reproduced from [19]).

semiconductor laser diodes do not have. However, laser diodes have drawbacks that remain hidden if not viewed in a production and integration scenario, where the factors of hybridization and alignment has a large influence on component cost, if the component is otherwise cheap in fabrication by polymer technology.

Another line of development, that was not as lately and rarely addressed as using the total internal reflection in the polymer, consists of distributed feedback (DFB) optical resonators formed in the dye doped polymer itself.

The concept of a laser oscillator based on distributed feedback from a Bragg grating formed along the gain medium was first demonstrated in 1970 (published 1971) by Kogelnik and Shank [20]. In order to demonstrate the principle, they used a 14 μm thick gelatine film doped with the organic dye Rhodamine 6G (see Figure 1.7). The Bragg grating on the film had a period of about 300 nm and was formed by interference lithography, and the size of the grating was 10 mm x 0.1 mm. The laser emitted light at a single wavelength (within the observational limit) when pumped by a UV Nitrogen laser (337 nm). However, the grating was continuous and did not contain a phase-shift to accommodate for the grating stop band. It is therefore possible that the laser operated on two narrowly spaced wavelengths simultaneously.

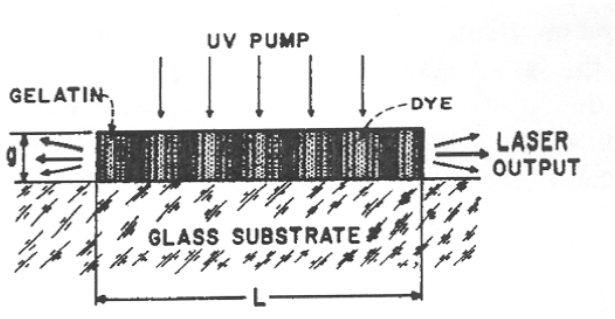

Figure 1.7: Sketch of the first DFB laser (reproduced from [20]).

Later in 1971 Shank, Bjorkholm and Kogelnik demonstrated another type of DFB

laser [21]. In this laser, the grating was not formed by periodic structural corrugation of the material, instead a periodic variation of the gain was introduced in the material by using two interfering pump beams to create the grating pattern during the pumping itself (see Figure 1.8). The gain medium was a bulk volume of liquid dye solution and the grating was thus formed only during pumping in a thin layer of the liquid. This method enabled wavelength tuning of the dye laser, simply by changing the angle of the two interfering pump beams. The gain grating further has the advantage that no phase shift is needed in the grating in order to obtain a single resonance at the Bragg reflection wavelength [22].

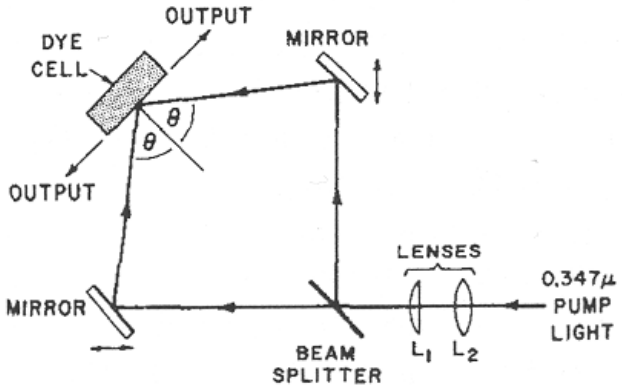

Figure 1.8: Optical setup for creating a gain grating in a dye cell (reproduced from [21]).

Since the demonstration of the tunable gain grating based DFB laser by Shank et al., several types of dye lasers based on the same principle have been demonstrated. However, all of them rely on a coherent pump source and bulk optics to create the pump beam grating pattern. This is not desirable features for lasers that are to be integrated in LOC systems, since both the pump setup and the laser should be as simple as possible and require as little alignment as possible. Therefore interference pumped gain grating lasers are not particularly suited for LOC integration. In addition, using a patterned pump beam, allows for light absorbing volumes of dye in the laser, where the pump beam does not excite the molecules and this increases the lasing threshold.

Fixed grating DFB lasers defined by surface corrugation (or by other means of variation of the real part of the refractive index) on the other hand, are well suited for LOC systems, on the condition that the fabrication of the grating is cheap and easy. Since low order gratings require high resolution of the lithography (in particular in order to incorporate any phase shifts of the gratings that may be desired), the method of lithography becomes an important issue.

Adequate theory for grating based lasers were developed alongside the experimental progress. Coupled mode theory for thick holographic gratings with large depletion of the forward propagating wave was developed by H. Kogelnik in 1969 and presented in [23]. Later the coupled mode theory was presented specifically for distributed feedback lasers in 1972, in the excellent presentation [24], where both real and imaginary refractive index modulation is considered. This article also concerns why gain gratings in principle always operate in a single mode

as opposed to index gratings. However, it appears to be only somewhat later, in 1984, that the concept of introducing a phase shift in the real refractive index grating was introduced. The phase shift ensures the resonator to have only a single resonance at the Bragg reflection wavelength (in the stop-band of the grating) [22].

To the knowledge of the author a solid state polymer dye DFB laser containing a phase shift was first demonstrated in the work covered in this thesis [25]. The work is described in Chapter 6.

Yet another line of development, apart from solid state DFB lasers and total internal reflection based solid state lasers, lies within the field of microfluidic dye lasers. To the knowledge of the author, the first microfluidic dye laser was demonstrated and characterized at MIC, DTU by B. Helbo and A. Kristensen [9]. Chapter 6 describes an adaption of this microfluidic laser type suitable for investigating certain gain material parameters.

1.3 Overview of this thesis

This thesis aims to present the examination of a range of different polymer dye laser architectures, in order to determine candidates for use in LOC systems. In addition, different fabrication methods are examined.

The first chapter gives an overview of the area of polymer dye lasers, including a first introduction to the laser types concerned in this thesis.

Chapter 2 gives an overview of some basic principles that are central for the function of the laser types discussed.

Chapter 3 gives a description of the modelling methods used to understand the optical structures and dynamics of the laser architectures in the thesis.

Chapter 4 gives an overview of the fabrication techniques that have been examined and used for fabrication of the polymer laser devices.

Chapter 5 first gives an overview of the laser types investigated and thereafter a more detailed view on the devices.

Chapter 6 describes various implementations of the dye polymer lasers. The aim of this chapter is to give examples of the possibilities with respect to integration and applications.

Chapter 7 concerns alternative micro resonator types.

Chapter 8 contains a discussion and outlook for the laser types, with particular emphasis on possible real-life applications.

Chapter 2

Materials

The three types of material that are used to build the laser structures are; polymer, silicate glass and mono crystalline silicon. All lateral structure in the laser devices is patterned in the polymer, while the hard materials, glass and silicon, only function as substrates and sealing lids.

This chapter aims to give a brief introduction to the materials that form the basis for the fabrication of the laser devices presented in this thesis. The section on polymers will briefly describe the nature of the polymers and touch on some of the relevant optical properties.

2.1 Polymers

In this section, the polymers that have been used to fabricate the laser devices are described. The first polymer, is more accurately described as a resist which polymerizes in a thermosetting process during the lithographic procedure. The two last polymers are thermoplasts.

2.1.1 SU-8 resist

The epoxy based resist SU-8 was developed for use in high aspect ratio UV-LIGA processes that requires the definition of thick resist layers. The resist was originally developed at IBM [26]. In Europe, the supplier of SU-8 resist is Microchem Corp. [27].

SU-8 is relatively transparent to allow UV light during the lithography step to penetrate deeply without too much absorption, this ensures that thick layers (up to 2 mm) can be used in the lithographic process. The transparency to UV light depends a lot on the wavelength (see Figure 2.1) therefore the right light source has to be used. SU-8 was developed for the Hg I-line (365 nm), but any radiation capable of triggering the photo-initiator can be used. SU-8 is a negative tone resist, meaning that radiation exposed areas will remain after the lithographic steps are completed (described in Chapter 5). SU-8 resist film thicknesses from

30 nm to 2 mm can be used.

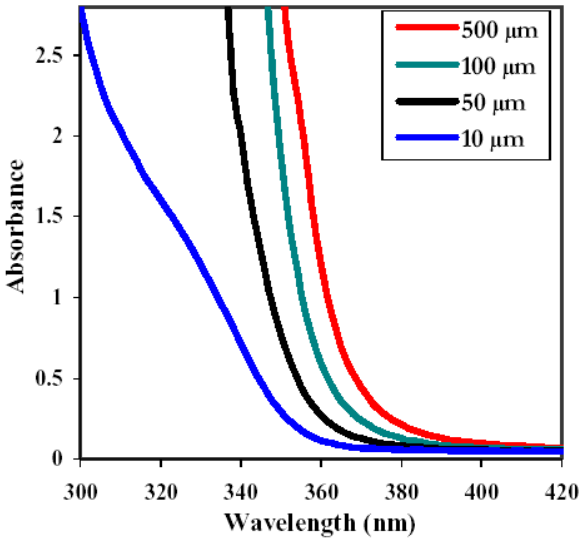

Figure 2.1: Absorption in the short-wavelength range for varying thin-film thicknesses of unexposed and uncured (but pre-exposure baked) SU-8 (reproduced from [28]).

The cross-linked resist is biologically unaggressive, and it has a high chemical resistance. It withstands organic solvents such as ethanol, acetone and methanol. This resistance makes the resist a candidate for LOC applications, since it can accept a wide range of substances. Only strong acids and bases etch away the cross-linked polymer. Being a thermosetting polymer, the polymer is naturally heat resistant but begins to degrade at 380°C.

SU-8 resist comes premixed in varying concentrations in GBL (gamma butyrolactone) or in cyclopentanone from the supplier [27]. The solutions can be further diluted to obtain thinner layers in spin processes, or foreign substances can be added to functionalize or alter the properties of the resist. In the work described in this thesis, the resist is doped with the laser dye Rhodamine 6G to render the cross linked resist optically active.

When using a polymer for optical purposes, the absorption loss is a concern. Apparently not much systematic data exist for the absorption of SU-8 as function of wavelength in the visible part of the spectrum, perhaps due to the influence of process parameters on this optical property. Some groups have manufactured waveguides using SU-8 as core material. Data are reproduced below from two articles on the measured propagation loss for SU-8 waveguides. Figure 2.2 shows the loss of SU-8 measured by back-cutting of a SU-8 waveguide with a core size of 30 µm by 100 µm post exposure baked at two different temperatures (see [29] for details).

Figure 2.3 shows a loss measurement on 10 µm thick and 30 µm wide waveguides fabricated by Bilenberg et al. [30]. It is not determined for either of the two loss measurements if the loss is occurring mainly due to the absorption in SU-8 or is due to imperfections in the waveguide structure.

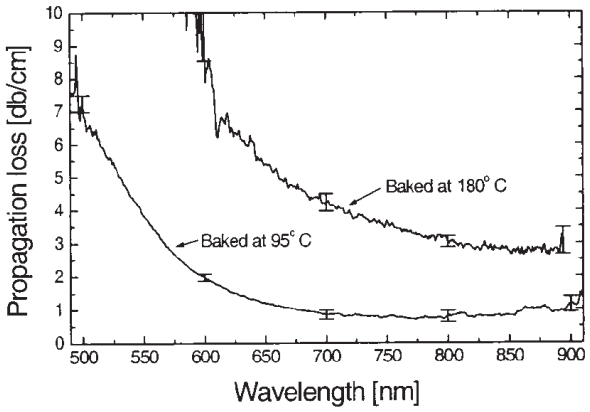

Figure 2.2: Propagation loss measured on a SU-8 waveguide 100 µm thick and 30 µm wide. The distribution of loss contributions between the SU-8 absorption and imperfections in the waveguide structure is unknown (reproduced from [29]).

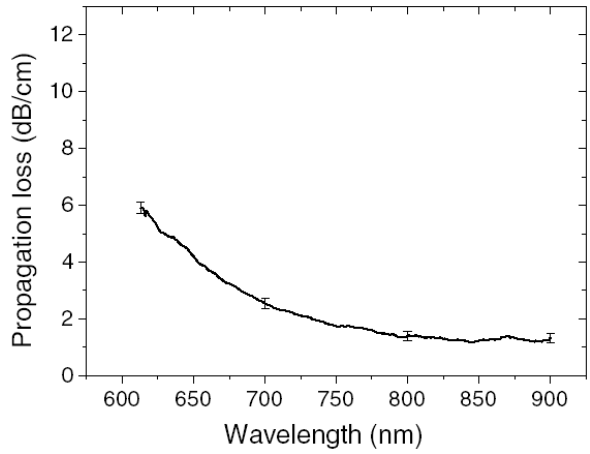

Figure 2.3: Propagation loss measured on a SU-8 waveguide 10 µm thick and 30 µm wide. The distribution of loss contributions between the SU-8 absorption and imperfections in the waveguide structure is unknown (reproduced from [30]).

Figure 2.4 shows a measurement of the absorption over a wide wavelength range (the method of measurement is not mentioned in the reference) [31]. It is apparent that the loss rises towards short wavelengths, which may also be reflected in the previous loss graphs in Figure 2.2 and Figure 2.3.

It is interesting that the loss at 633 nm for a 5 µm high and 5 µm wide SU-8 waveguide was reported to be as low as 0.19±0.03 dB/cm by Sum et al. in [32], determined by measuring the intensity of light scattered along the waveguide. The intrinsic loss in SU-8 has not been investigated in this thesis. In the authors opinion, the SU-8 related loss does not influence the functionality of the devices significantly.

For optical purposes, also the refractive index is a concern. The refractive index varies with wavelength (dispersion), as shown in the measurement illustrated in Figure 2.5 where the refractive index is measured down to 600 nm. From data

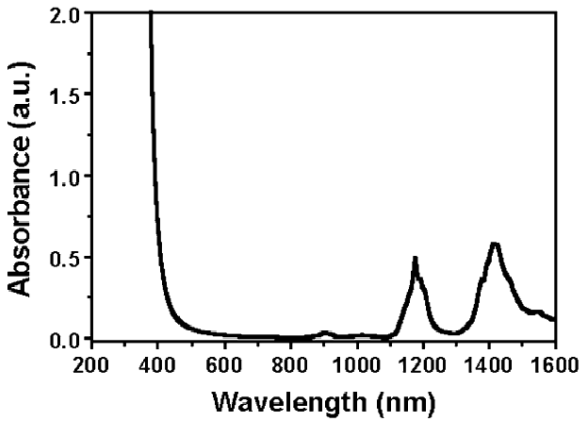

Figure 2.4: Absorbance of SU-8 as function of wavelength (reproduced from [31])

supplied from the manufacturer [27], the dispersion at 600 nm is $-1 \cdot 10^{-4}$ nm^{-1}.

The refractive index (and expectedly the dispersion) depends on the process parameters, as measured for example by [33]. In addition to this, addition of foreign substances (for example of Rhodamine 6G) to the resist may alter the refractive index.

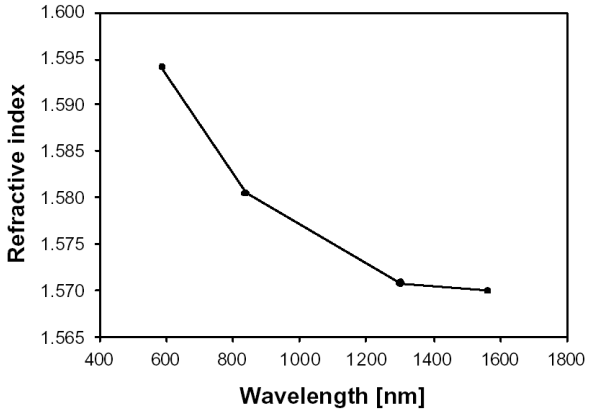

Figure 2.5: Refractive index of SU-8 film as a function of wavelength (reproduced from [34]).

2.1.2 PMMA

PMMA (poly-methyl methacrylate) is a well known highly transparent thermoplast. It is cheap and widely used, also in everyday items where it is also known under the name of plexiglass. PMMA comes dissolved for example in anisole, and is available with well controlled chain lengths. The chain length determines the viscosity of the polymer above the glass transition temperature, where the polymer changes from a glassy state where the polymer is elastic to a state where it can be deformed permanently [35]. This is an important parameter for nanoimprint

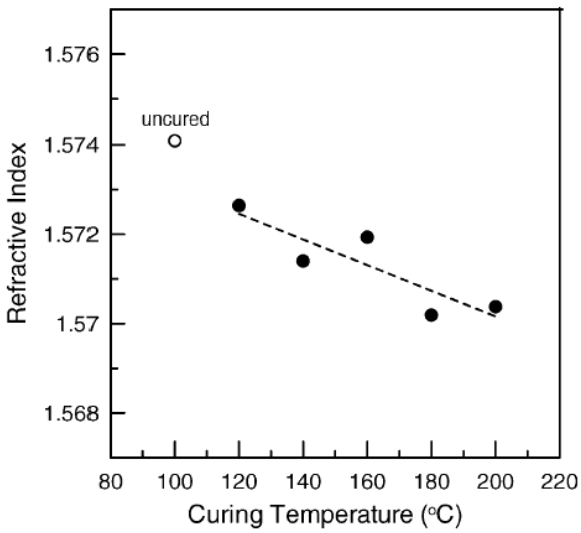

Figure 2.6: The refractive index of SU-8 as function of post-exposure bake temperature. The SU-8 film was baked for 3 minutes (the reference does not state at which wavelength, but it may have been 633 nm) (reproduced from [33]).

or bonding applications. The chain length of the PMMA used in this thesis for bonding is 950 k and the chain length for imprint was 50 k. The building block for PMMA is shown in Figure 2.7.

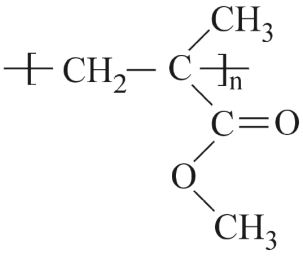

Figure 2.7: The monomer building block of PMMA. The subscript n indicates that the monomer inside the square brackets is repeated in the polymer chain.

The transmission at short wavelengths for PMMA is shown in Figure 2.8.

Figure 2.9 show the transmission loss of a fiber waveguide made in PMMA [37]. The loss in the visible is around 0.1 dB/m.

2.1.3 Cyclo-olefin copolymer (COC)

Cyclo-olefin copolymer (COC) is a highly transparent and chemically resistant thermoplast. It consists of chains of ethylene and norbonene (see Figure 2.10), and the relative amount of the two constituents determines the glass transition temperature. The chain length determines the refractive index. The different "grades" that are available of COC makes it possible to fabricate devices with a

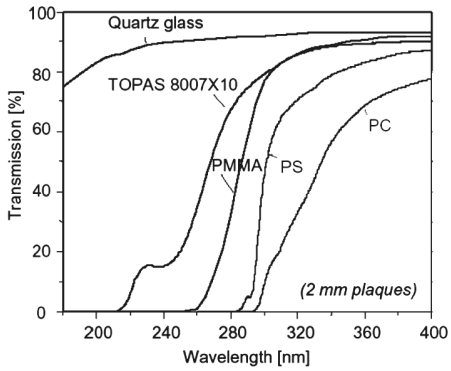

Figure 2.8: Figure showing optical transmissions of four common polymers, note PMMA and Topas. (Reproduced from [36])

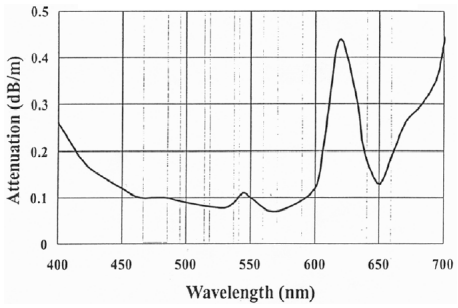

Figure 2.9: Figure showing optical transmissions of a PMMA fiber. (Reproduced from [37])

combination of grades with different refractive indices and glass transition temperatures, which can be exploited in the fabrication. It must be noticed however, that the different grades of COC have different behaviors, specifically relating to the formation of cracks in advanced fabrication steps (this has been examined by Dan Johansen in [38]). The optical loss for short wavelengths is illustrated in Figure 2.8, further measurements on loss can be found in [39].

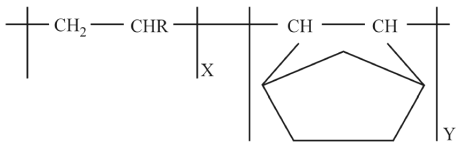

Figure 2.10: Figure showing the structure of the cyclo-olefin copolymer. The polymer consists of ethylene (left) and norbornene (right). The X and Y subscripts indicates that any of the two monomers may be followed by either of the two monomers in a random fashion.

2.2 The laser dye Rhodamine 6G

The organic laser dye that has been used throughout the work described in this thesis is Rhodamine 6G. Use of this dye as amplifying medium in lasers goes back to the 1970'ties, and the dye has remained a preferred laser dye due to its large quantum efficiency and relatively long lifetime before bleaching, compared to other dyes. Even today it is used extensively in tunable lasers for visible wavelengths in research laboratories for many applications such as spectroscopy. Rhodamine 6G has an organic molecular structure with the feature of conjugated double bonds. The structure is depicted in Figure 2.11.

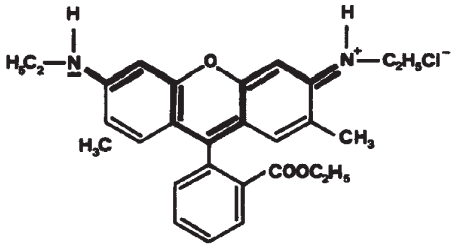

Figure 2.11: Rhodamine 6G molecule structure (reproduced from [40]).

Pure Rhodamine 6G comes in powders with a dark red color and liquid solutions of the dye are colored strongly in red, wherefore caution should be exerted during handling. It comes in various grades of which the laser grade is the most expensive. Cheaper grades have been used in this thesis, as the purity was not deemed important for the demonstration of the lasers described in this thesis.

The conjugated double bond structure of the molecule lowers the HOMO/LUMO gap (the energy level gap between the Highest Occupied Molecular Orbital and the Lowest Unoccupied Molecular Orbital) to allow for electronic transitions that interact with visible wavelength photons. A Rhodamine 6G dye molecule has an energy level diagram that is helium-like (see [41] p. 255), and the molecular electronic states are separated into singlet (denoted S_0, S_1...) and triplet states (denoted T_1, T_2 ...), according to the spin state of the electrons. The helium-like energy levels has a direct influence on how the dye can be used.

Figure 2.12 shows a representation of a part of the energy level diagram for Rhodamine 6G. The individual electronic state levels are broadened by molecular rotational and vibrational states along with collisional broadening due to the medium in which the dye is dissolved. Since the electronic levels themselves are broadened by the short excited state lifetime of a few nanoseconds, the molecular energy levels are in effect completely smoothed out in continuous bands. This smearing (which is also characteristic of other organic dyes) allows the molecule to have transitions in a continuous optical wavelength range. This is advantageous for making either tunable lasers, or lasers with a wide choice of wavelengths (see also [40]).

Apart from broadening the optical transitions, the energy bands have an important influence on the spectral response which is critical for obtaining gain with

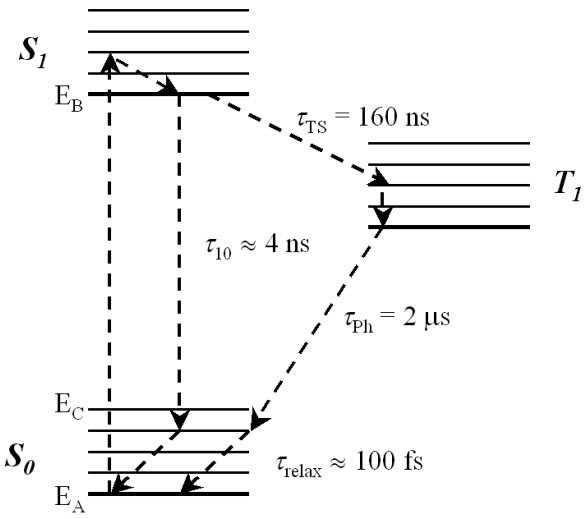

Figure 2.12: Simplified Rhodamine 6G energy level diagram. Time constants from [42].

the organic dye. Consider a single molecule: at room temperature, the molecule will rest at the lowest vibrational and rotational states in the S_0 band (thermally distributed). In order to excite the molecule to a state in the S_1 band, a minimum energy of $E_B - E_A$ must be used. When the molecule has been excited to the S_1 band, it will decay on a picosecond timescale to the lowest states in the band via non-radiative decay. When the molecule decays to the S_0 band, however, the smallest possible energy difference will be $E_B - E_C$, and the emitted photon may have a wavelength that is long enough not to be reabsorbed by other dye molecules. In the S_0 band, the molecule will decay non-radiatively on a picosecond timescale to the lowest states in the S_0 band. This mechanism separates the absorption and emission spectrally, and the shift of the spectra is denoted Stokes shift [40]. The shifted absorption and fluorescence cross sections are illustrated in Figure 2.13.

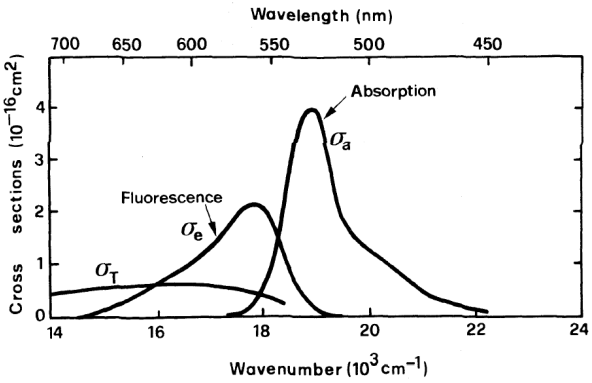

Figure 2.13: Cross sections for singlet-singlet absorption (σ_a) and fluorescence (σ_e), and triple-triplet (σ_T) absorption for Rhodamine 6G in ethanol. (from [43]).

The mechanism described above leading to the Stokes shift, enables the two energy

level bands S_0 and S_1 to function as a four level laser system. The basic four level lasing transition cycle is shown in Figure 2.14 for reference.

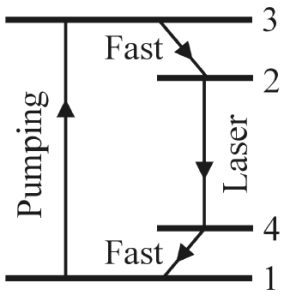

Figure 2.14: Principle of four level laser energy level diagram.

Considering the dye molecule as functioning in this four level manner, it is noteworthy that it is not necessary to invert the population of the molecular electronic states with respect to the bands S_0 and S_1 in order to obtain gain, only the laser transition has to be inverted. Inverting the laser transition is obviously easier than inverting the electronic state of the molecules, since the laser transition has a lifetime of a few nanoseconds and the state in the lower laser level decays on a pico-second timescale. Transparency on a certain wavelength for an ensemble of molecules however, demands an inversion larger than equality of states in the lower and the upper laser level, since the absorption cross section of the molecules that are not excited, extends far beyond the central absorption peak, and tails off in a manner close to exponentially (determined by inspection of absorption cross section data from [44, 45]). As a tool for modelling, the absorption and emission cross sections can be expressed by the following formulas, which are found by fitting to data from [44, 45]:

$$\sigma_{\mathrm{ab}}(\lambda) = 0.79288e^{-(\lambda[\mathrm{nm}]-550)/6.32731}10^{-16}\ [\mathrm{cm}]^2 \tag{2.1}$$

$$\sigma_{\mathrm{em}}(\lambda) = (178.6581 - 0.56165\lambda[\mathrm{nm}] + 4.4370110^{-4}\lambda^2[\mathrm{nm}^2])10^{-16}\ [\mathrm{cm}]^2 \tag{2.2}$$

The formulas are fitted with the measured cross section spectra in the wavelength range from 550 nm to 700 nm. The expressions should not be used uncritically, since the cross sections depend on the circumstances to which the dye is subjected.

The helium-like energy level diagram also contains triplet states that can be accessed by the molecules via a spin flip event. Since the molecules are embedded in a substrate, such an event is quite likely due to the influence of the surrounding material on the dye molecule, transferring angular momentum. Considering an ensemble of Rhodamine 6G molecules, approximately 3% of the molecules will end up in the triplet state T_1 after one pump cycle of the molecules. The fraction of molecules in the T_1 state is a result of the difference in transition rate from the excited state to the triplet and the ground state band, respectively (see Figure 2.12). The lifetime of the T_1 state itself is quite long, about 2 μs, and it is obvious that by pumping an ensemble of Rhodamine 6G molecules continuously, nearly all will quickly end up in the T_1 state. Besides "loosing" molecules from

the ensemble into a state that does not contribute to gain, the T_1-T_2 transition will absorb light and thus induce loss at the wavelengths where the dye would otherwise be able to amplify light. The cross section for this transition is depicted in Figure 2.13.

Due to the tendency to accumulate in the triplet state, the dye must be optically pumped in pulsed mode. All applications of the dye as gain medium must accommodate for this fact in one way or another. However, the pump pulses do not need to be as short as a few nanoseconds (as is used in the experiments described in this thesis), just as long as the rise-time of the pump pulse is steep enough (a few microseconds) so that gain is achieved before the molecules accumulate in the triplet state [46]. On considerations on rise-time, see for example [47]. However, short pump pulses have the advantage that more energy from the pulse can be used for stimulated emission to create laser light.

Rhodamine 6G molecules also have other channels of decay than through an optical transition. The optical excitation can cause the molecule to stop being optically active, either by decomposing the molecule directly through one or two photon processes or indirectly by (local) heating of the molecule. The local heating is caused by the non-radiative transitions of the molecule, dissipating the excess energy as heat. The combined effect of such processes is referred to as photobleaching, and results in rendering the dye optically inactive. High temperatures can also bleach the dye and through investigations done by D. Nilsson et al. [48], it turns out that the type of Rhodamine 6G ion that is used (Cl or ClO_4) has a large influence on the thermal stability. The chloride ion degrades at 140°C when embedded in SU-8, while the perchlorate ion does not degrade at temperatures up to (at least) 220°C. The thermal stability is particularly important when subjecting a dye doped polymer to process steps such as imprint lithography, where high temperatures may be used in order to exceed the glass temperature of the polymer to be shaped.

Rhodamine 6G may also loose its efficiency if the concentration is too high, due to interaction between the molecules. Figure 2.15 shows measurements of the quantum yield of Rhodamine 6G in ethanol at varying concentration at a temperature of 20°C. This drop in efficiency can also be expected to occur when doping solid matrices with Rhodamine 6G.

The solvent also has an influence on Rhodamine 6G. The strong polarity of water lowers the efficiency of the dye significantly, which is why Rhodamine 6G is nearly always used in ethanolic solution or dissolved in ethylene glycol.

It is noteworthy that doping a medium with Rhodamine 6G will change the refractive index of the medium. This effect can be used to tune the refractive index of polymers (or fluids) to create optical structures based on slight changes in refractive index.

It is important to be aware that the spectral profile of the gain varies with the inversion of the dye molecule ensemble, this is also well described in [40]. The net-gain is a result of the gain from the excited molecules and the absorption from the unexcited molecules. As the ensemble of molecules are pumped, the contributions

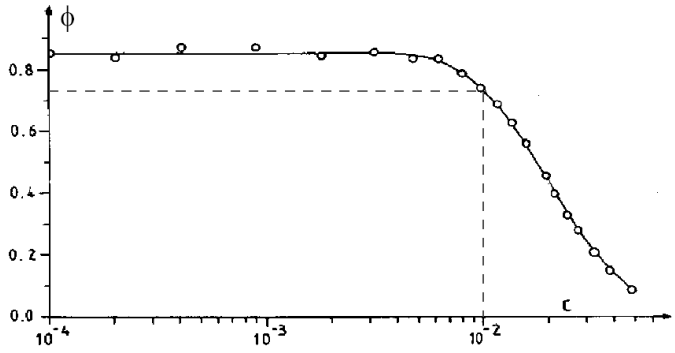

Figure 2.15: Quantum yield ϕ of Rhodamine 6G dissolved in ethanol as function of concentration. The measurements were taken at 20°C. The concentration c is in mol/L. A rapid drop of ϕ is observed at c$\approx 10^{-2}$ mol/L (reproduced from [49])

to the loss and the gain will change - thus shifting the net-gain maximum (see Figure 2.16).

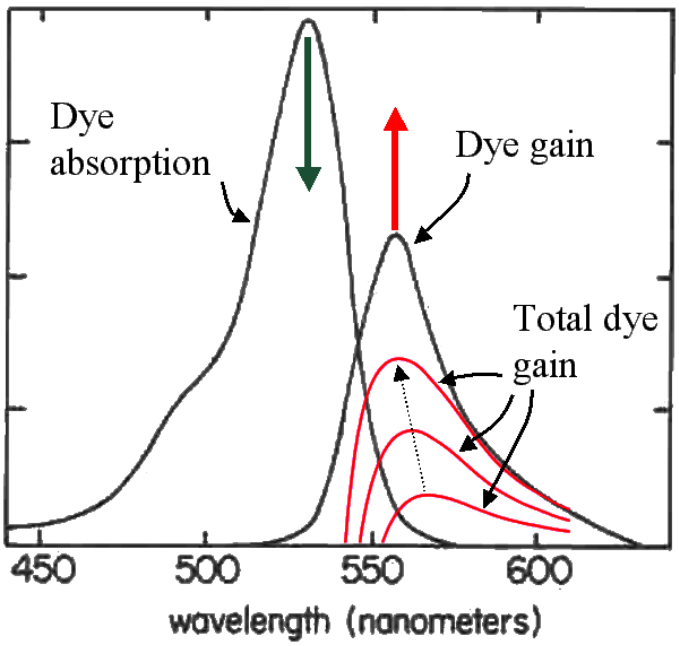

Figure 2.16: Sketch of the behavior of the fluorescence and absorption spectra during pumping (dotted arrows). As pumping is increased the gain increases and the peak of the gain moves to shorter wavelengths.

This has implications for the laser operation wavelength, since the size of the laser, the round-trip loss and the concentration of laser dye determines at which inversion level the lasing operation begins and thus clamps the inversion (gain).

The Rhodamine 6G powder from the manufacturer can be relatively easily dissolved in ethanol and ethylene glycol up to concentrations of ∼0.02 Mol/L. The powder is also readily dissolvable in SU-8 resist solutions. When doping PMMA, it is advantageous to dissolve the powder in ethanol first, and then add this solu-

tion to the anisole PMMA solution. It is advisable to use a magnetic stirrer in all cases.

Chapter 3

Optical principles and microfluidics

This chapter describes a few common optical principles that are essential for the functionality of the laser devices. The descriptions aim to provide the reader with a reminder or a brief introduction to the concepts. A more detailed description of the principles can be obtained in standard textbooks.

3.1 Stimulated emission, absorption and fluorescence

The interaction between the photon field and matter forms the basis for optical gain. In this thesis, the light interacts with molecules of the laser dye Rhodamine 6G. Although the energy levels for this dye molecule are quite complex, the most basic functionality of the molecule can be likened to an atomic two-level system. Consider such a system having two energy levels, E_1 and E_2, where $E_2 > E_1$. In the Einstein picture, there are three ways in which the system can change its state. A photon with an energy corresponding to $E_2 - E_1$, can be absorbed by the system and raise the energy level from E_1 to E_2. After a characteristic time the system will decay spontaneously to the lower state, emitting the excess energy as a photon. If the system is in its excited state (E_2), the decay can be stimulated by another photon, also with an energy $E_2 - E_1$. In the latter case of stimulated emission, the emitted photon will have the same direction, frequency and phase as the stimulating photon. The process of stimulated emission is the foundation of optical gain.

The Rhodamine 6G dye molecules used to obtain optical gain in the lasers described in this thesis operate along the same principle of absorption, fluorescence and stimulated emission as the two-level system. Only, the dye molecule has more energy levels. The energy levels were described in Section 2.2.

3.2 Total and partial internal reflection

Light impinging a dielectric surface (i.e. a surface between materials with different refractive indices), will experience reflection and refraction. In case of light

impinging a dielectric surface from the side of high refractive index, the reflection can be total. The common phenomenon of reflection (total or non-total) on a dielectric surface is used in most of the lasers described in this thesis to obtain the feedback in the resonator.

Snell's law describes the relation between the ray angles for refracted light [50]. The relation is

$$n_{\mathrm{i}} \sin(\Theta_{\mathrm{i}}) = n_{\mathrm{t}} \sin(\Theta_{\mathrm{t}}) \tag{3.1}$$

where n_{i} and n_{t} are the refractive indices of the "incident" and the "transmitted" medium and the angles Θ_{i} and Θ_{t} are given in Figure 3.1.

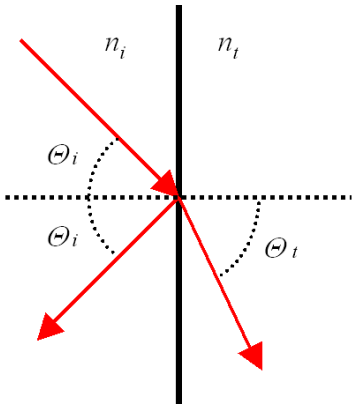

Figure 3.1: Illustration of reflection and refraction of an incident beam of light travelling in a material with refractive index n_{i} and impinging on the dielectric interface where the refractive index changes to n_{t}. Part of the beam is refracted with an exit angle of Θ_{t} and part of the beam is reflected with.

The critical angle of incidence, for and above which there is no transmitted ray is given by the situation where $\Theta_{\mathrm{t}} = 90°$. The critical angle Θ_{C} is given by

$$\Theta_{\mathrm{C}} = \arcsin \frac{n_{\mathrm{t}}}{n_{\mathrm{i}}} \tag{3.2}$$

Above this angle of incidence the phenomenon of total internal reflection occurs.

The reflected power from the dielectric interface depends on the polarization of the incident light. If the electric field vector of the electro-magnetic wave is parallel with a plane that is perpendicular to the dielectric interface plane (for example the picture plane in Figure 3.1), the polarization is termed p (from german: parallel), and the perpendicular polarization to this is termed s (from german: senkrecht). The power reflectances, R_{p} and R_{s}, for the two polarizations p and s are

$$R_{\mathrm{p}} = \frac{\tan^2(\Theta_{\mathrm{i}} - \Theta_{\mathrm{t}})}{\tan^2(\Theta_{\mathrm{i}} + \Theta_{\mathrm{t}})} \tag{3.3}$$

$$R_{\mathrm{s}} = \frac{\sin^2(\Theta_{\mathrm{i}} - \Theta_{\mathrm{t}})}{\sin^2(\Theta_{\mathrm{i}} + \Theta_{\mathrm{t}})} \tag{3.4}$$

The reflection at normal incidence is given by

$$r = \frac{n_{\mathrm{i}} - n_{\mathrm{t}}}{n_{\mathrm{i}} + n_{\mathrm{t}}} \tag{3.5}$$

The power reflectance, R, is given from the reflection r relating to the electric field, by $R = |r|^2$. In this thesis R is always termed power reflectance to avoid confusion, since there exists different nomenclatures in the literature with respect to R and r.

3.3 Waveguiding

In a ray picture, waveguiding occurs due to successive total internal reflection on dielectric surfaces (see Figure 3.2), and the phenomenon serves to confine and direct light (or other waves) within the waveguide structure. In order to obtain total internal reflection, the refractive index of the so-called core of the waveguide must be higher than the cladding (the material surrounding the core).

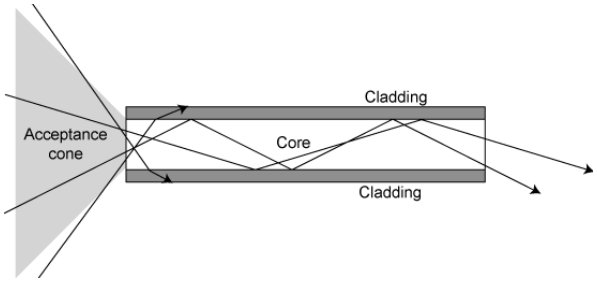

Figure 3.2: Principle drawing of waveguide. Light with incidence angles above the critical angle is reflected successively on the dielectric interface between the core and the cladding. This dependence on the angle leads to a restriction on how light can be coupled into the waveguide – the angle must lie within the acceptance cone (reproduced from [51]).

In most laser structures described in this thesis, the waveguiding takes place in a slab waveguide which essentially consists of three plane layers of dielectric material with refractive indices n_1, n_2 and n_3 – see Figure 3.3.

In this thesis the compound term "semi-plane slab wave" will refer to an electromagnetic wave guided by a slab waveguide, where the wave has a constant phase in the direction normal to the direction of propagation and normal to the slab plane. The semi-plane slab wave is thus a slab waveguide version of the free space plane wave.

For thin slab waveguides, the ray picture is no longer appropriate, and the propagation constant must be considered discrete. For a certain wavelength, the different possible propagation constants are denoted as TE-TM modes (or transverse

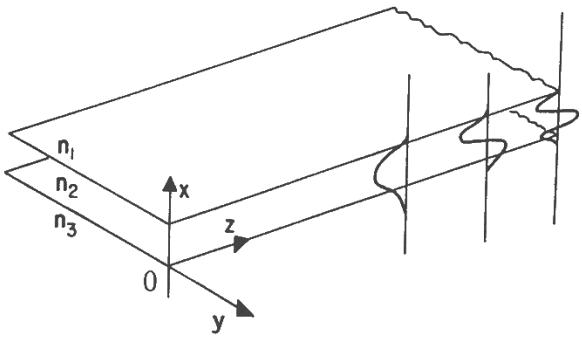

Figure 3.3: Basic three-layer planar waveguide structure. Three modes are shown, representing distributions of electric field in the x-direction. The planes illustrate the dielectric interfaces between the three materials (reproduced from [52]).

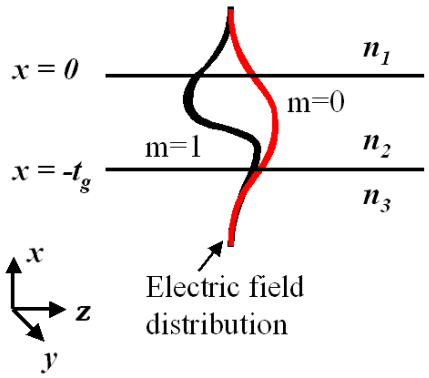

Figure 3.4: Illustration of the electric field distribution for the first two transverse modes (m=0 and m=1) in a planar waveguide.

modes, as later chapters will refer to in this thesis) and the lowest mode is termed the fundamental mode.

The electric field distribution across the waveguide has a number of nodes. The fundamental mode has no nodes, the next mode $m = 1$ has one node, etc. (see Figure 3.4). How to find the electric field distribution and propagation constants is described in Section 4.1.1.

3.4 Anti-guiding

In some cases the refractive index of the core of the waveguide must be lower than the upper and lower part of the cladding due to design necessities. In such structures, where the core has a lower refractive index than the cladding, light can still be guided, albeit not with the same efficiency as for normal waveguiding, as anti-guiding is lossy by nature.

3.5 Bragg gratings

Bragg reflection (or diffraction) is used in some devices presented in this thesis, in order to obtain a wavelength dependent reflection. The principle of Bragg diffraction was first described for X-rays on crystals by W.H. Bragg and his son W.L. Bragg in 1913, but also extends to radiation with visible wavelengths impinging on periodic dielectric structures.

The reflection from periodic dielectric structures is sensitive to the wavelength, since the total reflection is composed of the reflections from each period of the structure, and thus the phase must add up constructively to obtain a net-reflection.

A grating has maximum reflection of light impinging at normal incidence when the Bragg condition

$$2d = m\lambda \tag{3.6}$$

is satisfied, where the period of the grating is d, $m = 1, 2, ...$ is the mode number and λ is the wavelength in the material. However, in actuality, for each individual mode, m, the reflection occurs for a certain wavelength interval depending on the grating parameters. Section 4.1.2 and Section 4.1.3 describe methods to calculate the reflection spectrum for a grating.

3.6 Fluidic resistance for microfluidic channel

This last section is concerned with the fluidic resistance posed by a microfluidic channel which is much broader than it is high. This type of channel is common, since the lithographically structured polymer layer is often thin ($\sim$10 µm), while the channels are wide ($\gtrsim$100 µm).

The flow rate, Q, through a straight microfluidic channel of length, L, and with a rectangular cross section, where the height, H, is smaller than the width, W, is given by the following expression, assuming a linear pressure gradient Δp across the full length of the channel [53] (η is the viscosity of the fluid):

$$Q = \frac{HW^3}{12\eta}\frac{\Delta p}{L}\Big[1 - \frac{192W}{\pi^5 H}\sum_{m=1,3,5...}^{\infty}\frac{1}{m^5}\tanh\Big(\frac{m\pi H}{2W}\Big)\Big] \tag{3.7}$$

Which can be rewritten as:

$$\Delta p = \frac{96\eta L}{HW^3}\Big[1 - \frac{192W}{\pi^5 H}\sum_{m=1,3,5...}^{\infty}\frac{1}{m^5}\tanh\Big(\frac{m\pi H}{2W}\Big)\Big]^{-1}\cdot Q = R\cdot Q \tag{3.8}$$

The aspect of fluid resistance for the devices presented in this thesis have not been investigated in detail. The fluid resistance should be taken into account when designing small channels, as the pressure needed to drive the requested flow may be impractically high.

Chapter 4

Modelling methods

This chapter describes different techniques to model optical phenomena associated with miniaturized polymer dye lasers, in order to give the reader an introduction to important considerations that are relevant when designing laser devices. The chapter consists of two sections: The first section concerns the propagation of light and the second section concerns the interaction between pump light and dye molecules in dense dye solutions.

In order to be able to predict and optimize the behavior of laser structures, modelling of behavior of light in the resonator structures, and modelling the behavior of the gain material in the resonator is of much use. Many phenomena cannot readily be penetrated by intuition alone, and do not subject themselves to analytical or approximate solutions. Therefore, a plethora of methods to model optical behavior has been developed, each method with its own merits. This chapter reviews some methods which are particularly useful to model the behavior of miniaturized polymer lasers. These tools are intended as easy-to-use instruments for the interested reader. Rigid descriptions of the methods should be obtained from the literature (see references).

The conventions for the mathematical descriptions are adapted from the references in order to make it easy for the reader to refer to the references. The downside to this is that the convention changes from model to model described below, and combining results from the different methods must take this into account.

4.1 Light propagation in micro-optical structures

4.1.1 Wave guide mode solving

Finding the number of possible transverse modes (TE-TM modes) and their nature in a wave guide is important since the modes are usually non-degenerate with respect to their propagation constant. This non-degeneracy implies that individual modes with different propagation constants will be reflected from Bragg gratings at different wavelengths. Furthermore the different transverse modes will

give rise to complex mode patterns in Fabry-Pérot like resonators, since the Fabry-Pérot-mode spacing depends on the propagation constant of the mode. The mode patterns and the Bragg reflection wavelengths are essential to control in order to obtain single mode laser operation.

Below are given a few tools to predict the number of transverse modes in a planar waveguide, and a method to find the electric and magnetic field distribution throughout a waveguide. These tools are intended as easy-to-use instruments for the reader. It is highly recommendable however, to consult the work by Yariv [54] or Hunsperger [52], on which this section is based.

Consider a planar waveguide, as in Figure 4.1, consisting of three layers with refractive indices, n_1, n_2 and n_3 respectively, where the core layer thickness is t_g. Consider the field in the waveguide as described by $E_\mathrm{y}(x,z,t) = \mathcal{E}_\mathrm{y}(x)e^{i(\omega t-\beta z)}$, and let this be defined as the TE mode, for which the non-zero components are E_y, H_x and H_z. This fundamental type of waveguide is the one most commonly encountered in the polymer dye lasers concerned in this thesis. The planar waveguide approach is a good approximation in most cases where, for example, a waveguide defined by a strip of sandwiched polymer is much wider than it is high. Especially when the waveguide strip is so wide that the optical transverse modes in the horizontal direction (TE or TM) are so closely spaced with respect to their propagation constant that they are effectively degenerate, the approximation is good.

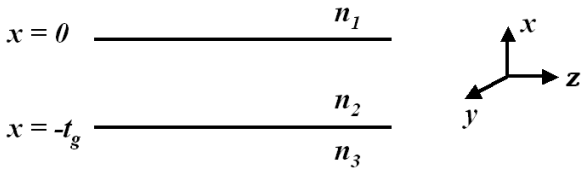

Figure 4.1: Sketch of planar waveguide consisting of three layers of dielectric material with refractive indices n_1, n_2 and n_1. The thickness of the middle layer is t_g and the surrounding layers extend to infinity.

The so-called cutoff condition determines how high mode orders can be guided in a planar waveguide. The mode order can be denoted by a mode number, m, which is a measure of how many nodal points the propagating field has in the direction normal to the direction of propagation (and normal to the waveguide plane). This is advantageous for a quick estimation of the TE mode structure of a waveguide without having to solve the transcendental equation (see below, equation (4.4)). There are three cases where the cutoff condition can be found with good approximation. In the case of a symmetric waveguide where $n_1 = n_3$ and $n_2 \cong n_1$, and Δn is the refractive index difference between the core and the cladding, a mode can exist when the following condition is satisfied [52]:

$$\Delta n = (n_2 - n_1) > \frac{m_\mathrm{s}^2 \lambda_0^2}{8 t_\mathrm{g}^2 n_2} \tag{4.1}$$

for the mode number $m_\mathrm{s} = 0, 1, 2, 3, ...$ In the case of a symmetric waveguide where $n_2 \gg n_1$, a mode can exist when [52]

$$\Delta n = (n_2 - n_1) > \frac{m_\mathrm{s}^2 \lambda_0^2}{4 t_\mathrm{g}^2 n_2} \tag{4.2}$$

is satisfied, also for $m_\mathrm{s} = 0, 1, 2, 3, ...$

In the case of an asymmetric waveguide, where $n_3 \gg n_1$, the cutoff condition becomes,

$$\Delta n = (n_2 - n_3) > \frac{m_\mathrm{a}^2 \lambda_0^2}{16(n_2 + n_3) t_\mathrm{g}^2} \tag{4.3}$$

with $m_\mathrm{a} = (2m + 1)$, $m = 0, 1, 2, 3, ...$

In cases where the exact number of modes is required, both for TE and TM modes, the so-called transcendental equation can be solved. The transcendental equation arises from a condition of continuity of the electric field at the dielectric interfaces between the three layers in Figure 4.1 [54]. Solving this, also yields the propagation constants of each mode, along with the electric or magnetic field distributions across the waveguide. For TE modes this equation can be written

$$\tan(h t_\mathrm{g}) = \frac{p + q}{h(1 - pq/h^2)} \tag{4.4}$$

where q, h and p are given by

$$\begin{aligned} q &= (\beta^2 - n_1^2 k^2)^{1/2} \\ h &= (n_2^2 k^2 - \beta^2)^{1/2} \\ p &= (\beta^2 - n_3^2 k^2)^{1/2} \end{aligned}$$

and $k \equiv \omega/c$. The propagation constant is β, which is the only unknown, and can be found by solving the transcendental equation. The number of solutions for β depends on the number of possible modes in the structure. The effective refractive index of the mode is related to β via $n_\mathrm{eff} = \beta/k$, using $k \equiv \omega/c$.

The transverse distribution is described by

$$\mathcal{E}_\mathrm{y}(x) = \begin{cases} C e^{-qx}, & \text{for } (0 \le x \le \infty); \\ C(\cos(hx) - (q/h)\sin(hx)), & \text{for } (-t_\mathrm{g} \le x \le 0); \\ C(\cos(h t_\mathrm{g}) + (q/h)\sin(h t_\mathrm{g})) e^{p(x + t_\mathrm{g})}, & \text{for } (-\infty \le x \le -t_\mathrm{g}) \end{cases}$$

for the structure in Figure 4.1. C is an arbitrary constant determining the strength of the field.

In the case of TM modes where the non-zero components are H_y, E_x and E_z, the transcendental equation is derived from continuity of the field $\mathcal{H}_\mathrm{y}(x)$, and reads

$$\tan(ht_{\mathrm{g}}) = \frac{h(\bar{p}+\bar{q})}{h^2 - \bar{p}\bar{q}} \tag{4.5}$$

where

$$\bar{q} = \frac{n_2^2}{n_1^2} q \tag{4.6}$$

and

$$\bar{p} = \frac{n_2^2}{n_3^2} p \tag{4.7}$$

Otherwise, q, h and p are the same as for the previous case. The transverse magnetic component $\mathcal{H}_{\mathrm{y}}(x)$ is given by

$$\mathcal{H}_{\mathrm{y}}(x) = \begin{cases} -C'((h/\bar{q})\cos(ht_{\mathrm{g}}) + \sin(ht_{\mathrm{g}}))e^{p(x+t_{\mathrm{g}})}, & \text{for } (-\infty \leq x \leq -t_{\mathrm{g}}); \\ C'(-(h/\bar{q})\cos(hx) + \sin(hx)), & \text{for } (-t_{\mathrm{g}} \leq x \leq 0); \\ -C'(h/\bar{q})e^{-qx}, & \text{for } (0 \leq x \leq \infty) \end{cases}$$

4.1.2 Transfer matrix method

In cases where a uniform periodic perturbation on a waveguide is weak, i.e. the scattering of light from a single period of a grating perturbation is small, it can be advantageous to model the system by using the versatile segmented transfer matrix method [55]. Here it is assumed that there exists two distinct modes in the perturbed waveguide; one for each direction of propagation. The modes are coupled to each other via a coupling constant, κ, that describes the amount of light that is coupled into the counter-propagating mode per length of waveguide.

In the transfer matrix approach, a non-uniform grating is sliced into sufficiently many uniform parts. Each part is represented by a transfer matrix and the final response from the grating is found by simple multiplication of the series of matrices for the individual parts of the grating, in the same succession as the parts appear in the grating. In the case of a uniform grating, such as is encountered in Chapter 6 the grating can simply be "divided" into one piece.

Consider the electrical field propagating in a waveguide represented by (the following is adapted from [55])

$$E = ae^{-j\beta z} + be^{j\beta z} = A + B \tag{4.8}$$

where a and b are the amplitudes of the forward and backward propagating field respectively. A and B represents the z-dependent field (for a fixed time). The boundary conditions that are used (see Figure 4.2) are: B_0=0 and A_1 is normalized to 1. Figure 4.2 illustrates a segment $\mathbf{T}$ of a grating.

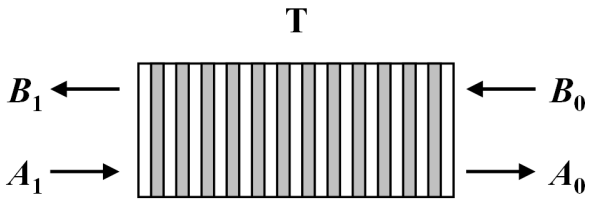

Figure 4.2: Segment of a grating in the transfer matrix approach. The forward and backward propagating waves are denoted with the letters A and B respectively. The relationship between the wave amplitudes can be expressed by a matrix.

The relation between the forward and backward propagating waves for the i'th segment of a grating can be represented by a matrix, $T_{\text{element},i}$, such that

$$\begin{bmatrix} B_1 \\ A_1 \end{bmatrix} = T_{\text{element},i} \cdot \begin{bmatrix} B_0 \\ A_0 \end{bmatrix} = \begin{bmatrix} t_{11} & t_{12} \\ t_{21} & t_{22} \end{bmatrix} \cdot \begin{bmatrix} B_0 \\ A_0 \end{bmatrix} \tag{4.9}$$

where t_{11}, t_{12}, t_{21} and t_{22} are the elements of $T_{\text{element},i}$. The combined matrix for a series of m grating sections is simply calculated by

$$T = \prod_{i=1}^{m} T_{\text{element},i} \tag{4.10}$$

The matrix T_{element} for a segment takes the form

$$T_{\text{element}} = \begin{bmatrix} \left(\cosh(ql) + \frac{j\delta}{q}\sinh(ql)\right) e^{-j\beta_0 l} & \frac{j\kappa}{q}\sinh(ql) e^{j\phi} e^{j\beta_0 l} \\ -\frac{j\kappa}{q}\sinh(ql) e^{-j\phi} e^{-j\beta_0 l} & \left(\cosh(ql) - \frac{j\delta}{q}\sinh(ql)\right) e^{j\beta_0 l} \end{bmatrix} \tag{4.11}$$

where

$$q = \sqrt{\kappa^2 - \delta^2} \tag{4.12}$$

and l is the length of the uniform grating section.

The detuning factor, δ, is an expression for the deviation of the light wavelength from the Bragg condition, and can be expressed as

$$\delta = \beta - \beta_0 = \frac{2\pi n_{\text{eff}}}{\lambda} - \frac{2\pi}{2\Lambda_{\text{grat}}} \tag{4.13}$$

where Λ_{grat} is the period of the grating. Furthermore, $\beta = 2\pi n_{\text{eff}}/\lambda_{\text{vac}}$ and $\beta_0 = \pi/\Lambda_{\text{grat}}$. The i'th segment of a grating is given by $T_{\text{element},i}$, where the local parameters of the grating are used.

If no discrete spatial phase shifts of the grating perturbation are present in the structure, the accumulated phase, ϕ, through the grating is, for each grating segment i:

$$\phi_i = \sum_{s=1}^{i-1} 2\beta_{0,s} l_s \tag{4.14}$$

where $\beta_{0,s}$ is β_0 for the s'th grating section and l_s is the length of the s'th section. In case phase shifts are present, they should be added to the sum at the grating segment where they appear. A spatial phase shift could for example consist of a translation of $\lambda/4$ at the middle of the grating.

The reflectance is given by the relation between the backward propagating wave at the input and the forward propagating wave at the input, such that

$$R = \left| \frac{B_1}{A_1} \right|^2 = \left| \frac{t_{12}}{t_{22}} \right|^2 \tag{4.15}$$

The transmittance is found as the relation between the forward propagating wave at the output and the forward propagating wave at the input, such that

$$T = \left| \frac{A_0}{A_1} \right|^2 = \left| \frac{1}{t_{22}} \right|^2 \tag{4.16}$$

From this, the response from a grating is fairly simple to calculate, as long as the grating is only a perturbation of the refractive index. However, the coupling constant must be found for the grating, before any response can be calculated.

In the case of a sinusoidal variation of the local effective refractive index caused by the grating perturbations, such that [55]

$$n_{\text{eff}}(z) = \overline{n_{\text{eff}}} + n_{\text{mod}} \cos\left(\frac{2\pi}{\Lambda_{\text{grat}}} z + \phi(z) \right) \tag{4.17}$$

where $\overline{n_{\text{eff}}}$ is the average effective refractive index, and n_{mod} is the amplitude of the refractive index modulation, then the coupling constant for the grating can be found from [54]

$$\kappa = \frac{\pi n_{\text{mod}}}{\overline{n_{\text{eff}}} 2\Lambda_{\text{grat}}} \tag{4.18}$$

The above expression can be used when the modulation n_{mod} concerns the modulation of the effective refractive index.

In case of a square-wave like variation of the materials as illustrated in Figure 4.3, where the modulation peak-to-peak height is a, the coupling constant can be expressed by [54]

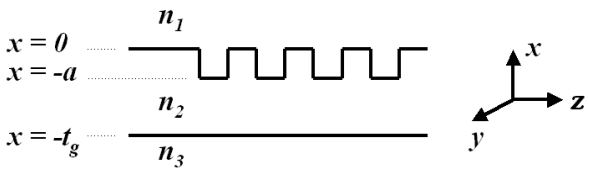

Figure 4.3: Sketch of a planar waveguide with a square formed corrugation on the surface between the dielectric mediums with refractive indices n_1 and n_2. The height of the corrugation is a.

$$\kappa = \frac{2\pi^2}{3l\lambda_0}\frac{(n_2^2 - n_1^2)}{n_2}\left(\frac{a}{t_g}\right)^3\left[1 + \frac{3(\lambda_0/a)}{2\pi(n_2^2 - n_1^2)^{1/2}} + \frac{3(\lambda_0/a)^2}{4\pi^2(n_2^2 - n_1^2)}\right] \tag{4.19}$$

where t_g is the thickness of the waveguiding layer with index n_2 and n_1 is the refractive index of the top layer. Also $l = 1, 2, 3...$ is the order of the harmonic responsible for the coupling, given by

$$l \cong \frac{\beta_m \Lambda}{\pi} \tag{4.20}$$

where β_m is the propagation constant of the mode, m, under consideration.

The coupling constant can be found for arbitrary corrugations by considering the spatial Fourier components of the corrugation, see [56] chapter 3, 6 and A7.

4.1.3 Transmission matrix method

Optical structures, such as laser resonator structures, containing abrupt refractive index differences poses a challenge with respect to finding the spectrally dependent reflection and transmission of the structure. An array of abrupt refractive index changes can for example make up a Bragg grating, as in the laser described in Chapter 6.

Due to the large refractive index differences used in certain devices (in Section 6.5), the transfer matrix method (Section 4.1.2), which is a commonly used method for distributed feedback grating resonators made with small refractive index perturbations, is not readily applicable. Instead, the transmission matrix formalism is a strong tool to find the spectral response, also of non-grating based devices.

The following explanation is based on [56] chapter 3.

The transmission matrices operate with normalized field amplitudes A_1, B_1, A_2 and B_2. The normalized field amplitude has the same phase as the electric field, and the absolute square of the normalized field amplitude is equal to the power flow.

Assume that the amplitude of the electric field of a plane monochromatic wave travelling in the z direction is (ignoring the polarization vector in the equation)

$$\mathrm{E}(x,y,z,t) = E_0 \mathcal{U}(x,y) e^{i(kz-\omega t)} \tag{4.21}$$

where $\mathcal{U}(x,y)$ is the field intensity distribution across the direction of propagation, such that $\int\int |\mathcal{U}(x,y)|^2 dxdy = 1$. The power of the electro-magnetic field is given by

$$P = \frac{1}{2}\epsilon_0 nc|E_0|^2 \int\int |\mathcal{U}(x,y)|^2 dxdy = \frac{1}{2}\epsilon_0 nc|E_0|^2 \tag{4.22}$$

where c is the speed of light, n is the refractive index of the medium and ϵ_0 is the permittivity of vacuum. The normalized field amplitude denoted A (or B, for the wave propagating in the opposite direction) is defined as

$$A \equiv \sqrt{\frac{1}{2}\epsilon_0 nc} \quad E_0 e^{ikz} \tag{4.23}$$

A_1 and A_2 denote the normalized field amplitudes of the waves propagating to the right at the ports of a system $\mathbf{T}$ (see Figure 4.4), while B_1 and B_2 are the normalized field amplitudes of leftward propagating waves.

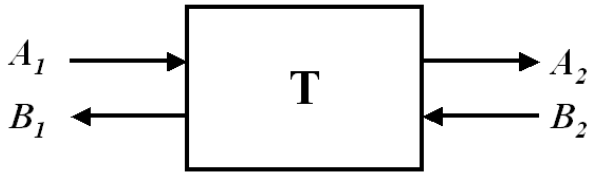

Figure 4.4: Sketch of a system $\mathbf{T}$, with input and output ports denoted by the letters A and B.

The system $\mathbf{T}$ relates the four field amplitudes to each other with a complex coupling coefficient for each pair. The system $\mathbf{T}$ is represented by a 2 by 2 matrix T, such that

$$\begin{bmatrix} A_1 \\ B_1 \end{bmatrix} = T \begin{bmatrix} A_2 \\ B_2 \end{bmatrix} \tag{4.24}$$

Transmission matrices for two fundamental structures are given below. For light incident on a surface with an abrupt change of refractive index, the transmission matrix is:

$$\frac{1}{t_{12}} \begin{bmatrix} 1 & r_{12} \\ r_{12} & 1 \end{bmatrix} \tag{4.25}$$

with

$$r_{21} = -r_{12}\ ,\ \ t_{21} = t_{12} \ \text{ and } \ r_{12}^2 + t_{12}^2 = 1 \tag{4.26}$$

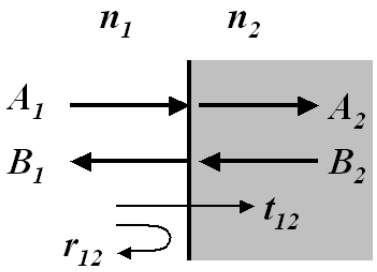

Figure 4.5: Dielectric interface between two materials with refractive indices n_1 and n_2. The interface has a reflection and transmission denoted by r_{12} and t_{12}. A_1, A_2, B_1 and B_2 represents the ports of the system.

where r_{12} is the reflectivity of the dielectric interface in Figure 4.5 for light impinging from the left side. The reflectivity is given by

$$r_{12} = \frac{n_1 - n_2}{n_1 + n_2} \tag{4.27}$$

and is thus negative if the light is reflected from the surface of a material with higher refractive index than the original medium, corresponding to a π change of phase.

Choose $\tilde{\beta}$ as the complex propagation constant, such that $\tilde{\beta} = 2\pi n_{\text{eff}}/\lambda_{\text{vac}}$, where n_{eff} is the effective refractive index, the value of which can be complex in case of the presence of gain or loss

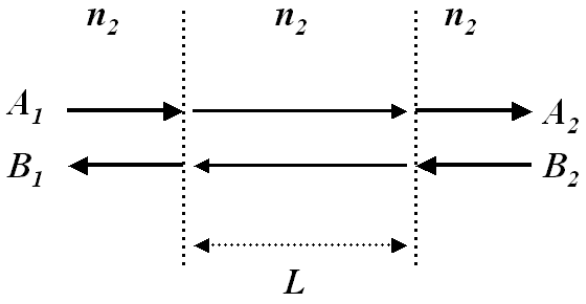

Figure 4.6: Transmission line of length L in a dielectric material of refractive index n_2. A_1, A_2, B_1 and B_2 represents the ports of the system.

The transmission matrix for light travelling a distance L in a medium where the propagation constant is $\tilde{\beta}$ is given by

$$\begin{bmatrix} e^{j\tilde{\beta}L} & 0 \\ 0 & e^{-j\tilde{\beta}L} \end{bmatrix} \tag{4.28}$$

The reflection from a system described by a transmission matrix T, is given by

$$r_{12} = \frac{T_{21}}{T_{11}} \tag{4.29}$$

and the transmission is given by

$$t_{12} = \frac{1}{T_{11}} \tag{4.30}$$

The key advantage of the transmission matrix method is that transmission matrices for large structures consisting of a series of the two fundamental elements described above can be found by simply multiplying the transmission matrices together in the order the structures appear in the system to be modelled. In this way a combined single 2 by 2 transmission matrix is formed, which can be used to calculate the reflection and transmission of the electro-magnetic wave due to the structure.

In this fashion, the functionality of a system can be judged by inspection of the system response in the form of reflection and transmission. However, other physical properties, such as the round trip loss of a resonator at a certain wavelength can also be found.

4.1.4 Using FEMLAB to solve electro-magnetic problems

Many commercial computer programs are available to help solving optical problems. COMSOL Multiphysics is a commercial program that uses the finite element method (FEM) to solve complex problems (the program was previously known as FEMLAB). An "electromagnetic module" is available for COMSOL Multiphysics, which makes it fairly easy to set up 2D and 3D geometrical structures of refractive index distributions, and calculate either the electromagnetic field in a structure as a response to a source, or solve for the electromagnetic eigenmodes of a structure. The finite element method is based on a mesh discretization of a continuous domain into a set of discrete sub-domains [57].

The major drawback of the finite element method is its need for large memory space and cpu time. The large computational demand is caused by the fact that the FEM needs to resolve the electromagnetic waves with 5 to 10 points per wavelength throughout the geometry. This leads to enormous data structures for only moderately sized structures, in particular for 3D calculations, and demands large computational resources. The limit of the structure size that can be practically calculated depends on the structure itself, and the computer at hand. As a rule of thumb, 2D calculations on structures up to an area of 10 by 10 µm should be easy to perform, and COMSOL Multiphysics may be the preferred tool for modelling the electromagnetic field.

Figure 4.7 shows a screen shot from a result screen in COMSOL Multiphysics. The colors in the image depict the electric field strength at a fixed time for an electromagnetic field with a vacuum wavelength of 570 nm. The 2D model consists of a SU-8 waveguide terminating in a triangle and was used to predict the power reflectance of the structures presented in Section 8.1. The surrounding material is air. In the model, a waveguide mode is injected on the left side into the waveguide. This mode is reflected at the triangle, albeit with some scattering loss which can

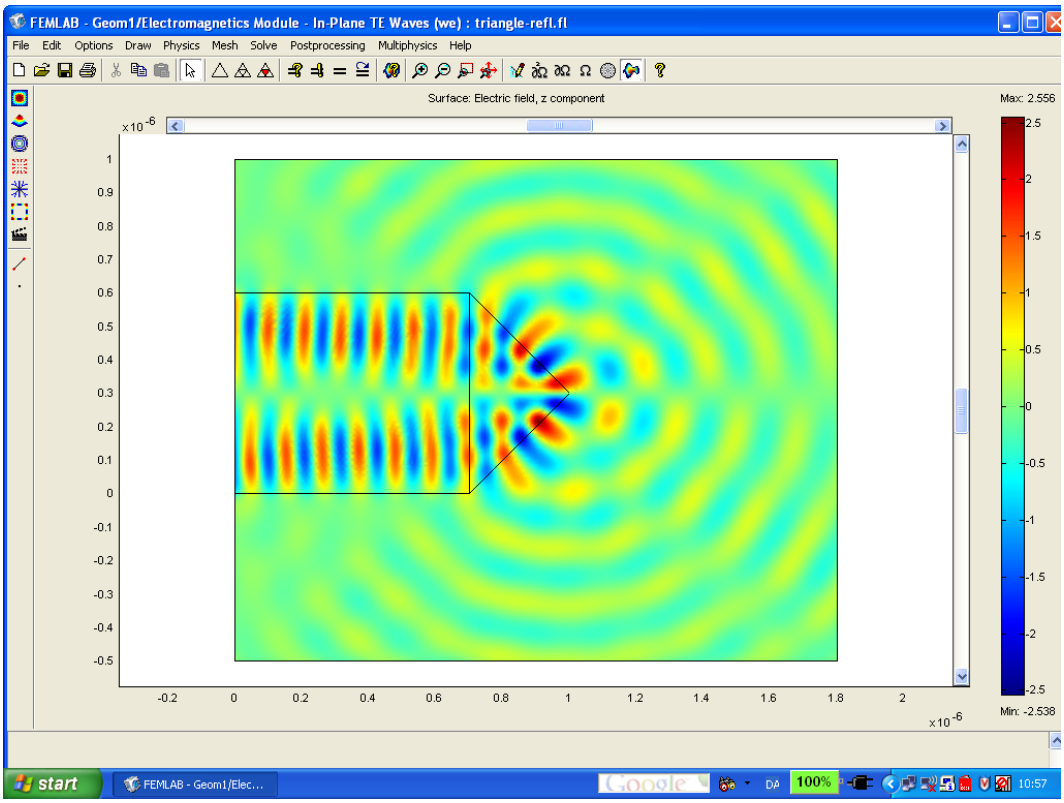

Figure 4.7: Screenshot from COMSOL Multiphysics showing the result of a simulation of an electromagnetic wave travelling in a waveguide that terminates in a triangle. The color scale depicts the magnitude of the electric field out of the plane. The scale is given in meters and the wavelength of the light is 570 nm. The model shows how light in the reflection is scattered.

be clearly discerned from the image of the electric field in the figure.

4.1.5 The Finite Difference Beam Propagation Method

The question of how light, that propagates through a medium, will be affected, is an often encountered problem in optics. For uniform media, solutions have been developed that readily yields the amplitude and phase of the electro-magnetic field at an arbitrary distance from an aperture (see for example [58] chapter 25).

However, for an arbitrary distribution of material (2D or 3D) with varying complex refractive index, prediction of how light will propagate through the structure is not a trivial problem and is often somewhat computationally demanding. Several approaches to solve the problem exist. For example, the Maxwell equations can be solved numerically in an arbitrary structure via the powerful finite element method, as utilized in the commercial program FEMLAB described in the previous section. For structures larger than a few micrometers however (for visible light wavelengths), the amount of grid points needed grows so large, that only extraordinarily large computers can solve the system of equations.

In order to avoid the very large data structures associated with solvers using, for example, the finite element method, a group of beam propagation methods (BPM's) have been developed. These methods assume paraxial propagation of the light, whereby the problem of propagation can be solved by following the phase front of the light along a fixed axis. This severely lowers the amount of data to be held in memory during calculation, as compared to the full solution using the finite element method, since only one slice at a time of the structure and field is used for calculation. Another method used in some BPM's in order to limit computation time, consists of an equivalent of shifting coordinate system, so that the coordinate system follows the light as it propagates, this makes it possible to make the step size in the calculation along the axis of propagation much longer than the wavelength.

Several commercial BPM solvers are available. In addition, a few free ones are available, of which I will recommend "LightPipes" [59], which can be an alternative to programming ones own BPM algorithm. Another small BPM program is called "FreeBPM" [60], which may be of some use.

In order to model the behavior of light in the optical structures concerned in this thesis, I have chosen a finite difference beam propagation method from [61]. The method was earlier described in [62]. See also [63] (but be aware of an error in equation 6b and 6c).

Although LightPipes is a good solver, with many possibilities, it does not allow for a continuously varying refractive index profile. Nor does it allow for gain to appear in the strucutres, why I decided to program a BPM anew. This also makes it possible to adjust the models without program specific constraints.

The method used in the modelling will be described somewhat in detail, in order to make the interested reader able to apply it to appropriate structures without consulting other literature (although this is also to be recommended). The method is described in the following part of this section for TE modes, however it is easy to adjust for TM modes, see [61].

The Helmholtz wave equation can be expressed as

$$\frac{\partial^2 U}{\partial x^2} + \frac{\partial^2 U}{\partial y^2} + \frac{\partial^2 U}{\partial z^2} + k^2 U = 0 \tag{4.31}$$

In order to compensate for the quick phase evolution in the direction of propagation of the wave (z), the following expression for the field is chosen

$$U(x, z) = e^{-ik_0 n_0 z} \psi(x, z) \tag{4.32}$$

where $k_0 = 2\pi/\lambda_{\text{vac}}$ and n_0 is the chosen refractive index at which the phase does not evolve with distance (during calculation) and $\psi(x, z)$ is a slowly varying function of z. The refractive index, n_0, can be chosen arbitrarily, but a good choice is to use the average refractive index the modelled wave will encounter.

Let the wavenumber be described by $k(x, z) = 2\pi n(x, z)/\lambda_{\text{vac}}$, where $n(x, z)$ is

the chosen refractive index distribution and λ_{vac} is the vacuum wavelength. After inserting the expression for $U(x,z)$ and $k(x,z)$ into (4.31), and applying the slowly varying envelope approximation ($\frac{\partial^2\psi}{\partial z^2} \approx 0$), one gets

$$2ik_0n_0\frac{\partial U}{\partial z} = \frac{\partial^2 U}{\partial x^2} + k_0^2(n^2(x,z) - n_0^2)U \tag{4.33}$$

Taking the difference coefficient with respect to x, via

$$\frac{\Delta U}{\Delta x} = \frac{U(x_0+\Delta x) - U(x_0)}{\Delta x} \tag{4.34}$$

one gets as the second order difference coefficient

$$\frac{\Delta^2 U}{\Delta x^2} = \frac{1}{\Delta x}\left(\frac{U(x_0+2\Delta x) - U(x_0+\Delta x)}{\Delta x} - \frac{U(x_0+\Delta x) - U(x_0)}{\Delta x}\right) \tag{4.35}$$

which can be rewritten to

$$\frac{\Delta^2 U}{\Delta x^2} = \frac{U_{i-1} - 2U_i + U_{i+1}}{\Delta x^2} \tag{4.36}$$

where $U_{i+1} = U(x_0+2\Delta x)$, $U_i = U(x_0+\Delta x)$ and $U_{i-1} = U(x_0)$. Then (4.33) becomes

$$2ik_0n_0\frac{\partial U_i}{\partial z} = \frac{U_{i-1} - 2U_i + U_{i+1}}{\Delta x^2} + k_0^2(n^2 - n_0^2)U_i \tag{4.37}$$

This expression is integrated from z to $z+\Delta z$:

$$2ik_0n_0(U_i(z+\Delta z) - U_i(z)) = \int_z^{z+\Delta z}\left(\frac{U_{i-1} - 2U_i + U_{i+1}}{\Delta x^2} + k_0^2(n^2 - n_0^2)U_i\right)dz \tag{4.38}$$

By denoting $U_q(z)$ by U_q^k and $U_q(z+\Delta z)$ by U_q^{k+1}, where q is $i-1$, i or $i+1$, one obtains

$$U_i^{k+1}\left(2ik_0n_0 - \frac{\Delta z}{2}k_0^2(n^2 - n_0^2) + \frac{\Delta z}{\Delta x^2}\right) +$$

$$U_i^k\left(-2ik_0n_0 - \frac{\Delta z}{2}k_0^2(n^2 - n_0^2) + \frac{\Delta z}{\Delta x^2}\right)$$

$$= U_{i-1}^k\left(\frac{\Delta z}{2\Delta x^2}\right) + U_{i-1}^{k+1}\left(\frac{\Delta z}{2\Delta x^2}\right) + U_{i+1}^k\left(\frac{\Delta z}{2\Delta x^2}\right) + U_{i-1}^{k+1}\left(\frac{\Delta z}{2\Delta x^2}\right) \tag{4.39}$$

By using the substitutions

$$\begin{aligned} a &= \frac{\Delta z}{2\Delta x^2} \\ b &= \frac{\Delta z}{\Delta x^2} - \frac{\Delta z}{2} k_0^2 (n^2 - n_0^2) + 2ik_0 n_0 \\ c &= -\frac{\Delta z}{\Delta x^2} + \frac{\Delta z}{2} k_0^2 (n^2 - n_0^2) + 2ik_0 n_0 \end{aligned}$$

equation (4.39) can be written in short form as

$$-aU_{i-1}^{k+1} + bU_i^{k+1} - aU_{i+1}^{k+1} = aU_{i-1}^k + cU_i^k + aU_{i+1}^k \tag{4.40}$$

This equation system yields an array of multiply dependent values for each propagation step. It is necessary to apply an algorithm in order to solve the N equations. For the current system, the Thomas Algorithm is appropriate. The following explanation is adapted from [64], but see also [56] chapter A16 for information about solution of finite difference problems.

The Thomas Algorithm is a simplified form of Gaussian elimination for tridiagonal matrices and is a common solution method. The algorithm solves equation systems of the form

$$\alpha_i U_{i-1}^{k+1} + \beta_i U_i^{k+1} + \gamma_i U_{i+1}^{k+1} = f_i(U^k) \tag{4.41}$$

for $\forall i = 1, ..., N_x - 1$. Choosing the boundary conditions $U_{i=0}^k = U_0$ and $U_{i=N_x}^k = U_{N_x}$ the following matrix system appears

$$\begin{bmatrix} 1 & 0 & 0 & \cdot & \cdot & \cdot & \cdot \\ \alpha_1 & \beta_1 & \gamma_1 & 0 & \cdot & \cdot & \cdot \\ 0 & \alpha_2 & \beta_2 & \gamma_2 & 0 & \cdot & \cdot \\ \cdot & \cdot & \cdot & \cdot & \cdot & \cdot & \cdot \\ \cdot & \cdot & \cdot & \cdot & \cdot & \cdot & 0 \\ \cdot & \cdot & \cdot & 0 & \alpha_{N_x-1} & \beta_{N_x-1} & \gamma_{N_x-1} \\ \cdot & \cdot & \cdot & \cdot & 0 & 0 & 1 \end{bmatrix} \begin{bmatrix} U_0^{k+1} \\ U_1^{k+1} \\ \cdot \\ \cdot \\ \cdot \\ U_{N_x-1}^{k+1} \\ U_{N_x}^{k+1} \end{bmatrix} = \begin{bmatrix} U_0 \\ f_1 \\ \cdot \\ \cdot \\ \cdot \\ f_{N_x-1} \\ U_{N_x} \end{bmatrix} \tag{4.42}$$

Gathering the boundary conditions in the second member yields

$$\begin{bmatrix} \beta_1 & \gamma_1 & 0 & \cdot & \cdot & \cdot \\ \alpha_2 & \beta_2 & \gamma_2 & 0 & \cdot & \cdot \\ 0 & \cdot & \cdot & \cdot & \cdot & \cdot \\ \cdot & \cdot & \cdot & \cdot & \cdot & 0 \\ \cdot & \cdot & \cdot & \cdot & \cdot & \gamma_{N_x-2} \\ \cdot & \cdot & \cdot & 0 & \alpha_{N_x-1} & \beta_{N_x-1} \end{bmatrix} \begin{bmatrix} U_1^{k+1} \\ U_2^{k+1} \\ \cdot \\ \cdot \\ U_{N_x-2}^{k+1} \\ U_{N_x-1}^{k+1} \end{bmatrix}$$

$$= \begin{bmatrix} f_1 - \alpha_1 U_0 \\ f_2 \\ \cdot \\ \cdot \\ f_{N_x-2} \\ f_{N_x-1} - \gamma_{N_x-1} U_{N_x} \end{bmatrix} = \begin{bmatrix} F_1 \\ F_2 \\ \cdot \\ \cdot \\ F_{N_x-2} \\ F_{N_x-1} \end{bmatrix} \tag{4.43}$$

There are two sweep steps in the solution algorithm. The first step reduces the number of non-zero elements in the matrix by "removing" the α_i coefficients. The following new coefficients are introduced:

$$\beta'_1 = \beta_1 \ , \ \ F'_1 = F_1 \tag{4.44}$$

$$\gamma'_i = \gamma_i \qquad \forall i = 1, ..., N_x - 1 \tag{4.45}$$

$$\beta'_i = \beta_i - \gamma'_{i-1} \frac{\alpha_i}{\beta'_{i-1}} \qquad \forall i = 2, ..., N_x - 1 \tag{4.46}$$

$$F'_i = F_i - F'_{i-1} \frac{\alpha_i}{\beta'_{i-1}} \qquad \forall i = 2, ..., N_x - 1 \tag{4.47}$$

The new algebraic system is defined by

$$\beta'_i U_i^{k+1} + \gamma'_i U_{i+1}^{k+1} = F'_i(U^k) \qquad \forall i = 1, ..., N_x - 2 \tag{4.48}$$

and

$$\beta'_{N_x-1} U_{N_x-1}^{k+1} = F'^k_{N_x-1} \ \text{ for } \ i = N_x - 1 \tag{4.49}$$

So after this step, the system is in the matrix form

$$\begin{bmatrix} \beta'_1 & \gamma'_1 & 0 & \cdot & \cdot & \cdot \\ 0 & \beta'_2 & \gamma'_2 & 0 & \cdot & \cdot \\ 0 & \cdot & \cdot & \cdot & \cdot & \cdot \\ \cdot & \cdot & \cdot & \cdot & \cdot & 0 \\ \cdot & \cdot & \cdot & \cdot & \beta'_{N_x-2} & \gamma'_{N_x-2} \\ \cdot & \cdot & \cdot & 0 & 0 & \beta'_{N_x-1} \end{bmatrix} = \begin{bmatrix} F'_1 \\ F'_2 \\ \cdot \\ \cdot \\ F'_{N_x-2} \\ F'_{N_x-1} \end{bmatrix} \tag{4.50}$$

The second step is to backward sweep the new matrix in order to obtain the solution. Firstly,

$$U_{N_x-1}^{k+1} = \frac{F'^k_{N_x-1}}{\beta'_{N_x-1}} \tag{4.51}$$

and then the solutions for the step $k+1$ is

$$U_i^{k+1} = \frac{F_i' - \gamma_i' U_{i+1}^{k+1}}{\beta_i'} \quad \forall i = N_x - 2, ..., 1 \tag{4.52}$$

By applying the Thomas Algorithm to the equation system (4.40), the field can be propagated through arbitrary complex refractive index distributions $n(x, z)$.

I have applied the FDBPM equations and the Thomas Algorithm with the "Mathematica 4.0" program, however most programming languages are appropriate. Furthermore, since a main feature of the laser devices to be modelled is the slab waveguide modes, I have implemented a 2-dimensional FDBPM version as described. Expanding to 3D is more or less straight forward, but requires much more computing time.

An important concern during modelling is how to apply sensible boundary conditions. Without further adjustment, the above method have reflective boundaries. Some effort has been exerted be several people in order to find good ways of implementing different kinds of boundary conditions in BPM's [65, 66]. During the modelling of the laser structures in this thesis, I have taken a simple approach, and fashioned the boundaries as a part of the refractive index matrix, that also contains the structures to be modelled. The upper and lower boundaries of the refractive index matrix are matched to the index of the upper and lower material, with respect to the real part of the index. The imaginary part of the refractive index is fashioned such that the absorption rises toward the edge of the calculating field. This gives absorbing boundaries, and thus prevents boundary reflection problems.

4.1.6 Finding the resonator round trip loss

A fundamental characteristic of resonators is their ability to store energy for a period of time. In optical resonators, the energy is obviously stored as light or photons trapped in a suitable structure. One way of describing this ability of optical resonators, is to express it as the loss of energy the light experiences from taking one round trip in the resonator, i.e. after ending up again in the place where it began. Describing the resonator by its round trip loss is advantageous when considering the gain that must be exerted by the gain medium in order to obtain lasing (i.e. when the net round-trip loss is 1).

Each optical mode in a resonator must be treated independently, unless two or more modes are degenerate with respect to the propagation constant. This can, for example, be the case for different polarization modes, in some resonator types. For the kind of resonators considered for the polymer dye lasers in this thesis, the modes will not be degenerate, and the round trip loss must in principle be found for each mode that exists, in order to describe the functionality of the resonator.

Let the round trip loss, RTL(λ), be denoted by the energy loss fraction at a certain wavelength, for one trip around the resonator. Consider the complete feedback in a resonator described by two mirrors with reflectivities $|r_1(\lambda)|$ and $|r_2(\lambda)|$ and phaseshift $\phi_1(\lambda)$ and $\phi_2(\lambda)$ positioned at distances L_1 and L_2 from a plane of

reference p, see Figure 4.8.

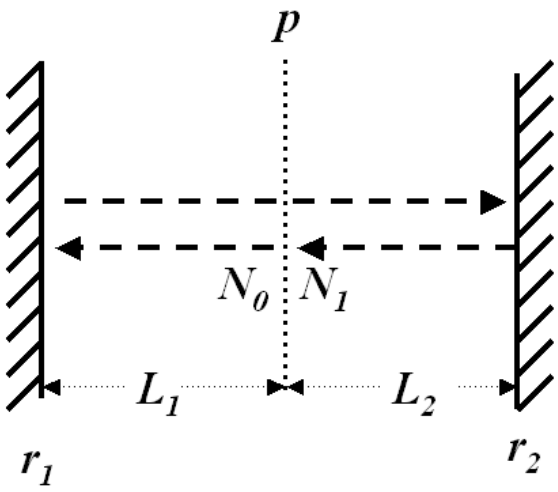

Figure 4.8: Sketch of optical resonator consisting of two mirrors with complex reflectivities r_1 and r_2. The distance between the mirrors is $L_1 + L_2$. N_0 photons begin a round trip in the resonator at the plane p, and N_1 photons are left after one round trip.

Consider a particle view of the photons. If N_0 photons start out at the reference plane p, then, on average, N_1 photons will reach the reference plane again, travelling the same direction as in the beginning (after being reflected twice). That is, the number of photons after one round trip:

$$\begin{aligned} N_1 &= N_0 \cdot (1 - \mathrm{RTL}(\lambda)) \\ N_1 &= N_0 |r_1|^2 |r_2|^2 |e^{-jkL_1 - j\phi_1} e^{-jkL_2 - j\phi_2}|^2 \end{aligned} \tag{4.53}$$

For ordinary mirrors, the feedback parameters are straight forward to apply to find the round trip loss. In the cases where Bragg gratings are used to create the feedback in the laser resonator, finding the round trip loss is not quite as straight forward, but still fairly easy. There are (at least) two ways of doing this. Either the Bragg gratings can be substituted with an effective mirror around the Bragg reflection wavelength, or the whole structure can be used to compute the round trip loss as function of wavelength using the transmission matrix formalism. The latter method yields the most information, but requires more computing.

The effective mirror model of a grating, asserts that the grating acts as a mirror located an effective distance L_{eff} from a reference plane located at the beginning of the grating. The model can be a good approximation at wavelengths near the reflection maximum of a grating since the phase in this region varies close to linearly near the reflection maximum. However, the applicability of the model is confined to this linear phase variation region.

Consider the effective mirror to reflect with the maximum value of the grating reflection $|r_{\mathrm{g}}|$, and the location of the mirror to be a distance L_{eff} away from the actual beginning of the grating.

The phase picked up by light travelling the distance L_{eff} is βL_{eff}, where β is the average propagation constant in the grating and $\beta_0 = \pi/\Lambda_{\text{grat}}$. Therefore, by assuming a linear relationship between the detuning $\delta = \beta - \beta_0$, from the Bragg condition and the phase, then for the case where $|\delta L_{\text{g}}| \ll \pi$ - with L_{g} being the length of the grating, one has

$$r_{\text{g}} \approx |r_{\text{g}}| e^{-2j(\beta-\beta_0)L_{\text{eff}}} \tag{4.54}$$

and it can be shown that [56] (still under the condition $|\delta L_{\text{g}}| \ll \pi$) a good approximation for the effective length is

$$L_{\text{eff}} = \frac{1}{2\kappa} \tanh(\kappa L_{\text{g}}) \tag{4.55}$$

where κ is the coupling constant of the grating.

Since L_{eff} is designed to give the correct mirror phase, it can be used to locate the longitudinal cavity modes, that are characterized by a total round trip phase accumulation in the resonator of $2\pi n$, where $n = 0, 1, 2, 3....$

Thus, the parameters that are needed to use the effective mirror model is the length of the grating, L_{g}, and the grating coupling constant, κ.

Finally, having found $|r_{\text{g}}|$, the phase, $2(\beta - \beta_0)L_{\text{eff}}$ and L_{eff}, these can be inserted as the mirror reflectivity, phase shift and position, in the expression for the round trip loss (4.53).

Another way to find the round trip loss for a resonator with a Bragg grating build from discrete elements with abrupt changes in refractive index, is to calculate the grating reflectivity as function of wavelength by using transmission matrix formalism. This formalism was presented in Section 4.1.3, and is straight forward to apply by using standard mathematical tools such as Mathematica, MathCad or MatLab.

In order to find the round trip loss for the resonator built with abrupt changes in the refractive index, the 2 by 2 transmission matrices, T^A and T^B, for each part of the bisected resonator should be found. The transmission matrices can be found via the method in Section 4.1.3. If the resonator contains a built in phase shift, the bisection plane can be inserted at the phase shift location. Consider a symmetric resonator, then $T^A = T^B = T(\lambda)$. In this symmetric case, where the middle of the structure is used as reference plane, a wave travelling to the right at the reference plane, will experience a reflection $r^A(\lambda) = T_{21}(\lambda)/T_{11}(\lambda)$ from the right part of the grating, and subsequently an identical reflection $r^B(\lambda)$ from the left part of the grating, as determined by the transmission matrix $T(\lambda)$, see Fig. 4.9. The round-trip loss at each longitudinal mode wavelength, λ_{lm}, is found as $\text{RTL}(\lambda_{lm}) = 1 - |r^A(\lambda_{lm}) r^B(\lambda_{lm})|^2$. Here, λ_{lm} are the longitudinal mode wavelengths where the imaginary part of $r^A(\lambda_{lm}) r^B(\lambda_{lm})$ equals zero, as required for the resonance to have no phase lag during one resonator round trip.

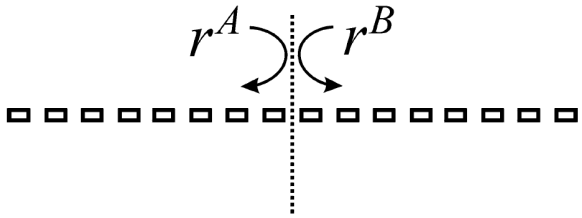

Figure 4.9: Symmetric Bragg grating with central reference plane and complex reflectivity, r^A, from the right part and r^B from the left part.

4.2 Dye molecule excitation

This section describes a model of the behavior of a dye gain medium forming a thin, optically dense film. The model can be used to predict the spectral gain profile as a function of time and pump power. This can in turn be used to predict lasing threshold and wavelength.

4.2.1 Spatio-temporal inversion evolution

When optically pumping the molecular electronic states of the dye embedded in a material, the pump photon density will decrease as the pump light travels through the material that is pumped due to absorption. Especially if the material is optically dense with respect to the pump light wavelength, the inversion obtained in the material along the propagation direction of the pump light, will depend on the penetration depth of the pump light. Considering that the transparency of the material to the pump light depends on the local inversion, since excited state molecules will not absorb pump light (assumption), it is clear that the gain distribution throughout the gain material, and thus the modal gain, is not trivial to find, especially in the case of pulsed pumping conditions where steady state solutions cannot be used.

In the case of molecular laser gain materials with a Stokes-shift, such as the Rhodamine 6G dye which is used in the light emitting devices in this thesis, the spatio-temporal dynamics of the inversion will influence the resulting lasing wavelength. It is therefore of double interest to be able to examine the evolution of inversion during an optical pump pulse.

In order to model the inversion dynamic, it is necessary to know the value and spectral variations of the absorption and the emission cross section for the dye species in question. These depend on the specific conditions, such as the temperature, concentration and solvent used. Therefore, it is difficult to know the precise cross sections without measuring them under the same conditions as the modelling aims to describe. However, in the following I approximate the cross-sections from data on dilute solutions of Rhodamine 6G in ethanol at room temperature (see also section 2.2).

It is advantageous to describe the absorption and emission cross sections, σ_{ab} and

σ_{em}, with functions fitted to experimental data. The advantage consists in the elimination of the noise and limited resolution of the original measurements, the cost is an injection of conjecture into the model. The functions below, (4.56) and (4.57), describe the cross sections in the wavelength range 550 nm to 700 nm.

$$\sigma_{\mathrm{ab}}(\lambda[\mathrm{nm}]) = 0.79288e^{-(\lambda[\mathrm{nm}]-550)/6.32731}10^{-16}\ [\mathrm{cm}]^2 \tag{4.56}$$

$$\sigma_{\mathrm{em}}(\lambda[\mathrm{nm}]) = (178.6581-0.56165\lambda[\mathrm{nm}]+4.4370110^{-4}\lambda^2[\mathrm{nm}^2])10^{-16}\ [\mathrm{cm}]^2 \tag{4.57}$$

Preliminary note: The model presented below is a suggestion for how to approach the problem of finding the spectral gain distribution in dye doped layers which are optically dense with respect to the pump light. It must be mentioned that the stability of the method has not been confirmed. The issue concerning the distribution of absorbed pump power has also been addressed by Blit and Ganiel [67].

The model for finding the temporal evolution of the modal gain spectrum due to a pump pulse is based on slicing time and space into finite chunks with sizes considerably smaller than the characteristic times and lengths involved in the physical process. The Rhodamine containing layer is divided into $l_{\max}$ thin layers, each with a thickness of Δx, see Figure 4.10.

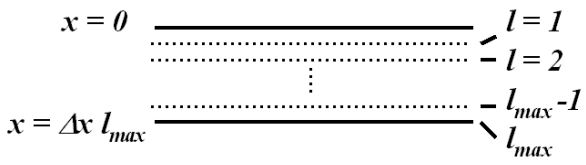

Figure 4.10: Sketch of the division into layers of the dye doped film. The film thickness is $\Delta x l_{\max}$ and the layer number is denoted by l.

For each time segment, the inversion of the Rhodamine molecular electronic states and the penetration of the optical pump light is calculated via rate equations. The time is divided into $\tau_{\max}$ segments, each with a duration of Δt, short enough to adequately resolve the pump pulse shape. In this manner, the spectral shape of the modal gain can be calculated throughout the duration of the pump pulse. The wavelength at which the modal gain just reaches the assumed resonator loss, can be interpreted as the resulting lasing wavelength, using the assumption that lasing action will clamp the gain. In this way, the lasing wavelength can be found. In reality, the gain will not be uniformly clamped spectrally and the Rhodamine 6G containing media will also have a spatially distributed gain, giving rise to spectral and spatial hole-burning respectively. The result from the model, however, gives a pointer to the dynamics of the system, and the model will give more accurate results if more precise cross-section functions are used.

Consider the frequency doubled Nd:YAG pump pulse (λ =532 nm) to be a gaussian pulse described by

$$Y(t) = Y_0 e^{-2(t-t_0)^2/w^2} \tag{4.58}$$

where $Y(t)$ is the power per cm^2, and w is the pulse length.

As mentioned, the layer of dye doped material is divided into $l_{\max}$ layers, each of thickness Δx. The layer numbers are denoted by $l = 1, 2, ..., l_{\max}$, and the position is given by $x = l\Delta x$. Also the time is sliced into $\tau_{\max}$ pieces of duration Δt such that the time is given by $t = \tau\Delta t$. The pump light intensity in the l'th layer and at the τ'th time slice is denoted $Y_{\tau,l}$.

Since the time steps are much shorter than the characteristic decay times for the dye molecules, and much shorter than the characteristic rise and fall time of the pump pulse, but longer than the time it takes for the pump light to propagate through the dye medium, it is reasonable to calculate the pump light intensity distribution throughout the layers, for each time step, based on the density of absorbing molecules present at each particular time step.

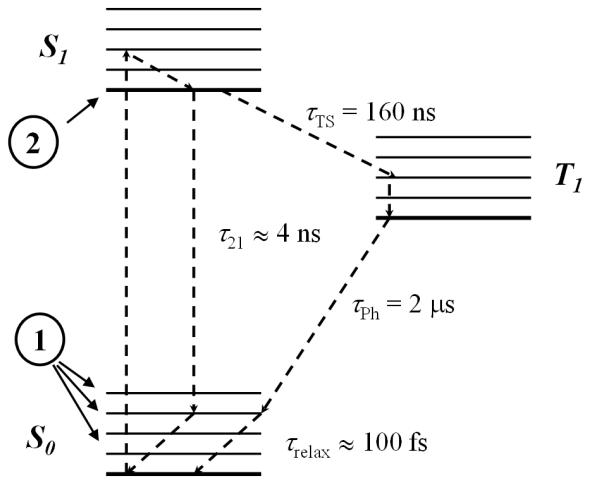

Figure 4.11: Sketch of energy level diagram for Rhodamine 6G with relevant life times. S_0 and S_1 denote ground singlet state band and excited state band, while T_1 denote the lowest triplet state band. The encircled numbers 1 and 2 denote the lower and the upper laser level respectively.

At the first time step, no molecules are excited, and $N_{2,0,l} = 0$, for $l = 1, 2, ..., l_{\max}$, where $N_{2,\tau,l}$ denotes the concentration of molecules in the upper laser level at the time $t = \tau\Delta t$ and the depth $x = l\Delta x$. It is assumed that the decay of the vibrational and rotational states in the S_1 and S_0 bands is so fast that the molecules immediately return to the lowest state in their respective band. Thereby the system can be described as a four level laser system. The upper laser level, 2, is the vibrationally relaxed state in the S_1 band, and the lower laser level, 1, is a vibrationally excited state in the S_0 band.

During the calculation, each time step is taken in succession. For each step, first the pump distribution throughout the layers is calculated. Then the change in the state population caused by the pump photons and natural decay of the molecular electronic states is calculated for each layer.

For the first layer, $l = 1$, the "residual" pump energy density is yet unperturbed by any dye molecules and

$$Y_{\tau,1} = Y(\tau\Delta t) \tag{4.59}$$

while the pump energy density for deeper layers is perturbed by the dye molecules. Thus, in the model, the pump energy density at the top of each layer forms the basis of the molecular response of the layer. Another approach, which will yield slightly more accurate results, is to use the pump energy density that is present in the middle of the layer. However, considering the error contributions from other sources, this should not be critical. Since molecules in the excited state do not contribute to the absorbtion of the pump light, the state populations have to be taken into account. Let N be the total concentration of optically active dye molecules (both excited and unexcited). The pump energy density as a function of layer is calculated by

$$Y_{\tau,l+1} = Y_{\tau,l} e^{-\Delta x \alpha (N - N_{2,\tau,l})/N} \tag{4.60}$$

for $l = 1, 2, ..., l_{\max} - 1$, where α is the absorption coefficient for the dye.

Thus, the pump energy distribution is found throughout the medium for the time step τ, and the state change response from the molecules can be calculated. Since the model only applies below lasing threshold, the number of photons in the resonator will be negligible, and the rate equations to calculate the state change response are

$$\frac{dN_2(t)}{dt} = (N - N_2(t))\eta\sigma_{\text{ab}} Y_{\tau,l} \frac{1}{\hbar\omega} - \gamma_{21} N_2(t) - \gamma_{TS} N_2(t) \tag{4.61}$$

$$\frac{dN(t)}{dt} = -\gamma_{TS} N_2(t) \tag{4.62}$$

Where $N_2(t)$ is the concentration of molecules in the upper laser level as function of continuous time, N is the total concentration of optically active dye molecules, η is the quantum efficiency of the dye molecules, γ_{21} is the decay rate of the upper laser level to the lower laser level and γ_{TS} is the decay rate from the upper laser level to the triplet state - in which the molecules are considered to be lost with respect to their optical activity due to the long lifetime of the triplet state.

The first differential equation describes the change of population of the upper laser level, which is influenced by the pump light intensity together with the number of molecules available for excitation $(N - N_2(t))$. It is also influenced by the decay rates from the state, γ_{21} and γ_{TS}. There are numerous other decay channels, caused by for example interaction between two closely space dye molecules. These other channels may, in part, be taken into account by adjusting the quantum efficiency, η, of the molecules.

The second differential equation describes the change of concentration of the complete number of photo-active molecules, due to transition into the triplet state,

from which the molecules are assumed to be decaying to the photoactive state (singlet) much slower than the characteristic time of the pump light pulse.

However, if the characteristic time of the pump pulse is much smaller than $1/\gamma_{\mathrm{TS}}$, then state-pumping into the triplet state can be ignored. So setting $\gamma_{\mathrm{TS}} = 0$ and solving to obtain an expression for $N_2(t)$, the following is obtained

$$N_2(t) = N\frac{\eta\sigma_{\mathrm{ab}}Y_{\tau,l}\frac{1}{\hbar\omega}}{\eta\sigma_{\mathrm{ab}}Y_{\tau,l}\frac{1}{\hbar\omega} + \gamma_{21}} + Ce^{(-\gamma_{21}-\eta\sigma_{\mathrm{ab}}Y_{\tau,l}\frac{1}{\hbar\omega})t} \tag{4.63}$$

where the constant C is determined by the condition

$$N_2(0) = N_{2,\tau,l} \tag{4.64}$$

and obviously when $t = 0$,

$$C = N_{2,\tau,l} - N\frac{\eta\sigma_{\mathrm{ab}}Y_{\tau,l}\frac{1}{\hbar\omega}}{\eta\sigma_{\mathrm{ab}}Y_{\tau,l}\frac{1}{\hbar\omega} + \gamma_{21}} \tag{4.65}$$

From this, the new inversion after each time step is easy to find as

$$N_{2,\tau+1,l} = N_2(\Delta t)\mid_{\tau,l} \tag{4.66}$$

where $\tau = 1, 2, ..., \tau_{\max} - 1$ and $N_2(\Delta t)$ is found anew for each time step, τ, and layer number, l.

After the calculation of a new inversion distribution throughout the layers, the new pump light distribution must be calculated and so forth.

The result is an array of inversion values for each time step and layer. In order to find the modal gain for a certain mode, m, the electro-magnetic field distribution and the local gain in the dye medium must be taken into account.

The local gain, for a certain concentration of molecules in the upper laser state, N_2, as a function of the wavelength can be expressed by

$$g(\lambda) = \sigma_{\mathrm{em}}(\lambda)N_2 - \sigma_{\mathrm{ab}}(\lambda)(N - N_2) \tag{4.67}$$

To obtain the transverse modal gain, which is the incremental rate of growth of the mode field as it propagates down the gain-structure, the following expression can be used (from [56] section A5.1):

$$\langle g\rangle_{\mathrm{xy}} = \frac{\int \mathcal{E}^*(x,y)g(x,y)\mathcal{E}(x,y)dA}{\int |\mathcal{E}(x,y)|^2 dA} = \frac{\int g(x,y)\mathcal{E}^*(x,y)\mathcal{E}(x,y)dA}{\int |\mathcal{E}(x,y)|^2 dA} \tag{4.68}$$

where $\mathcal{E}(x,y)$ is the distribution of the electric field. The field distribution for a planar waveguide can be obtained as described in section 4.1.1 (notice the difference in coordinate system).

In case the gain for a complete mode in a resonator is to be obtained, the weighted average along the z axis of $\langle g \rangle_{\mathrm{xy}}$ with the field should be taken.

In cases where the field and the gain is constant in the lateral direction (y) the modal gain is expressed simply by

$$\langle g \rangle_{\mathrm{x}} = \frac{\int g(x)\mathcal{E}^*(x)\mathcal{E}(x)dx}{\int |\mathcal{E}(x)|^2 dx} \tag{4.69}$$

This is approximately the case for structures based on planar waveguiding, where the structure is much wider than it is high.

In this way, the small signal gain for modes in a planar waveguide pumped by a pulsed source, can be found as function of time and wavelength. The model should work insofar as the cross section functions are accurate and as the pump pulse is much shorter than the inter-system crossing lifetime. The cross-sections are, however, dependent on solvent, temperature and concentration. The model can be extended to take intersystem crossing and other phenomena into account.

The model was used to find the threshold of the microfluidic laser in Section 6.5.

Chapter 5

Fabrication techniques

Several methods of fabrication of structures in thin films have been used throughout the work covered in this thesis. All methods are lithographic in nature, and the patterns are formed in a thin structurable layer on top of a hard substrate.

The four lithographic techniques that have been tried are

- UV lithography
- Electron beam lithography (EBL)
- X-ray lithography (XRL)
- Nanoimprint lithography (NIL)

This chapter describes the four different lithography types, and aims to provide the reader with a sense of the techniques, advantages and disadvantages. Quantitative comparative studies are not described.

The motive for examining the diverse techniques has been to determine which kind would be appropriate for particular structure types.

5.1 Lithography

Lithography is the process of writing on a surface, originally a stone surface. The primary lithographic method used for the laser devices described in this thesis, is radiation induced patterning of a thin polymer layer. Using radiation to pattern surfaces has the advantage that simple shadow masks can be used to replicate the pattern of the mask in the resist. In the case of single narrow ray like radiation, the ray can be scanned to define the patterns, as in electron beam lithography.

The resist used for all radiation patterned devices described in this thesis, is SU-8 from Microchem Corp. [27]. The resist has a negative tone, meaning that areas exposed to radiation will remain after development. Under the influence of radiation, an acid is formed in the resist, which promotes polymerization during

a subsequent heat treatment. The radiation exposed SU-8 is thus thermosetting, while the unexposed is not, and the non-polymerized SU-8 can be removed by a mild solvent (developer). For more on SU-8, see [4, 68], and for in-depth details on the different lithographic techniques, see the referenced literature.

5.1.1 UV lithography on SU-8

As the name implies the method uses ultraviolet radiation in order to induce the chemical change forming the photo-initiator acid in the SU-8 resist to be patterned.

The apparatus for performing the UV exposure of the resist (usually called an "aligner"), consists of a UV source, a mask holder, a substrate holder and microscope to align mask and substrate. The UV source delivers the radiation for the exposure. For SU-8, the source should be based on a Hg lamp with filters to allow only the Hg I-line (365 nm) to reach the SU-8 as described in Section 2.1.1. The mask holder and the substrate holder keeps the mask and substrate in close proximity or in contact, while also allowing alignment of the two. Opening a shutter exposes the mask and substrate assembly to the UV light.

A mask made of metal (for example Cr) on a transparent plate is used to cast a shadow on the photosensitive resist. Masks can be ordered from several companies.

For SU-8, the standard process sequence is illustrated in Figure 5.2. Apart from a spin step illustrated in Figure 5.1, where dissolved resist is deposited on the substrate, the process sequence consists of; 1) a pre-exposure bake, where the resist solvent is evaporated, 2) exposure with UV light through a mask, 3) a post-exposure bake, where exposed resist is cross linked and 4) a development and rinsing step, where unexposed resist is dissolved by a developer.

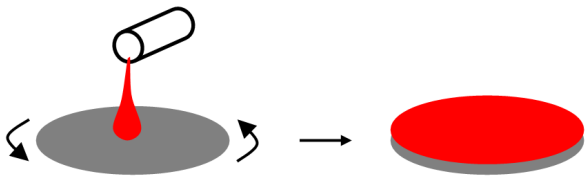

Figure 5.1: Thin films of resist are deposited on substrates via a spin process.

Figure 5.3 shows 26 µm wide strips of UV defined SU-8. The two pictures show the same structure from two different angles. There are several characteristics in the pictures that are connected with using UV light. Although the illustrated structures were not optimized with respect to corner sharpness and resolution, they do represent characteristics that are present, even for optimized structures. First of all, the corners of the strips of SU-8 are rounded (as viewed from above), whereas they should nominally have been sharp right angles. The rounding of the corners in the structures in Figure 5.3 is caused by using a small distance of 30 µm between the mask and substrate during UV illumination, and the rounding would be smaller (see Figure 5.4) if the mask and substrate was kept in contact. However,

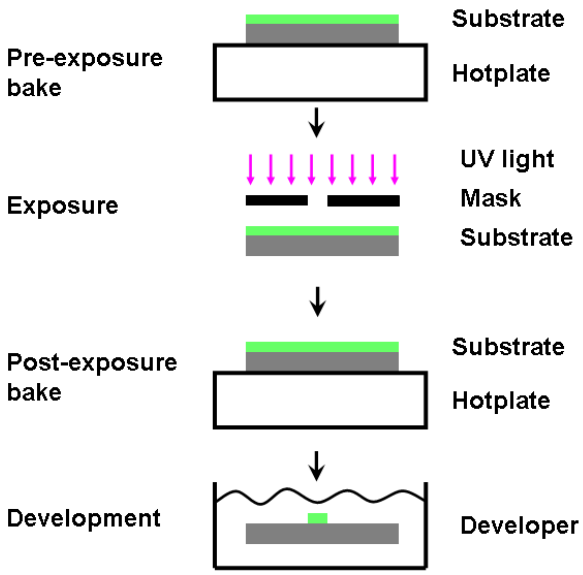

Figure 5.2: The lithographic steps for UV lithography on SU-8.

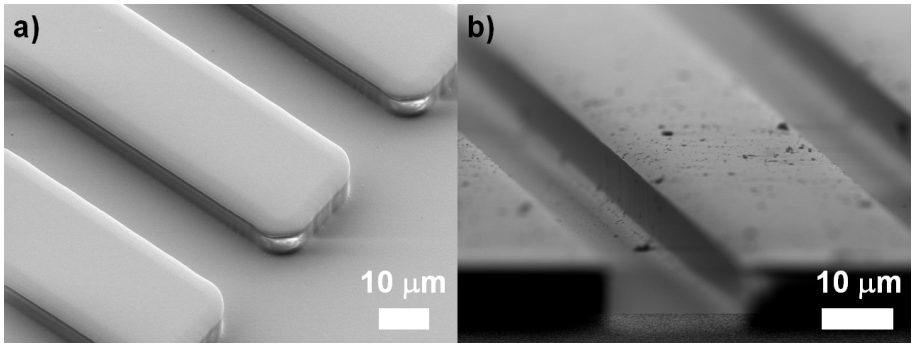

Figure 5.3: 26 μm SU-8 strips on a glass substrate fabricated via UV lithography. The structure is seen from two different angles.

contact between the mask and substrate tends to stick the two of them together, thereby contaminating the mask - especially due to the edge bead phenomena.

Secondarily, the step from cross linked resist to removed resist is not a perfect step function. The resist has a "skirt" at the foot of the structures and the top surface of the structures bends down before the step initiates.

For optical structures, the good verticality of the wall that is obtained in the lithography is beneficial, but the "skirt" and the bending of the top surface are likely to lead to scattering losses. In spite of this, UV lithography can be used to make lasers of sufficient quality to operate in a single mode.

The lithographic result varies with the process parameters. The main parameters are the exposure dose and the post-exposure bake temperature. In general the parameters must be optimized to the resist thickness. The parameters described in Chapter 6 and in the articles referenced in the appendix, can be recommended

as starting points for replication of the devices.

The minimum structure size with UV lithography is determined by the finite wavelength of the light, which leads to diffraction, and thus also by the thickness of the resist. With optimization, good resolution and aspect ratios can be achieved with UV lithography on SU-8. In Figure 5.4 a structure with an aspect ratio of 6 and a width of about 1 μm is illustrated (from [33]).

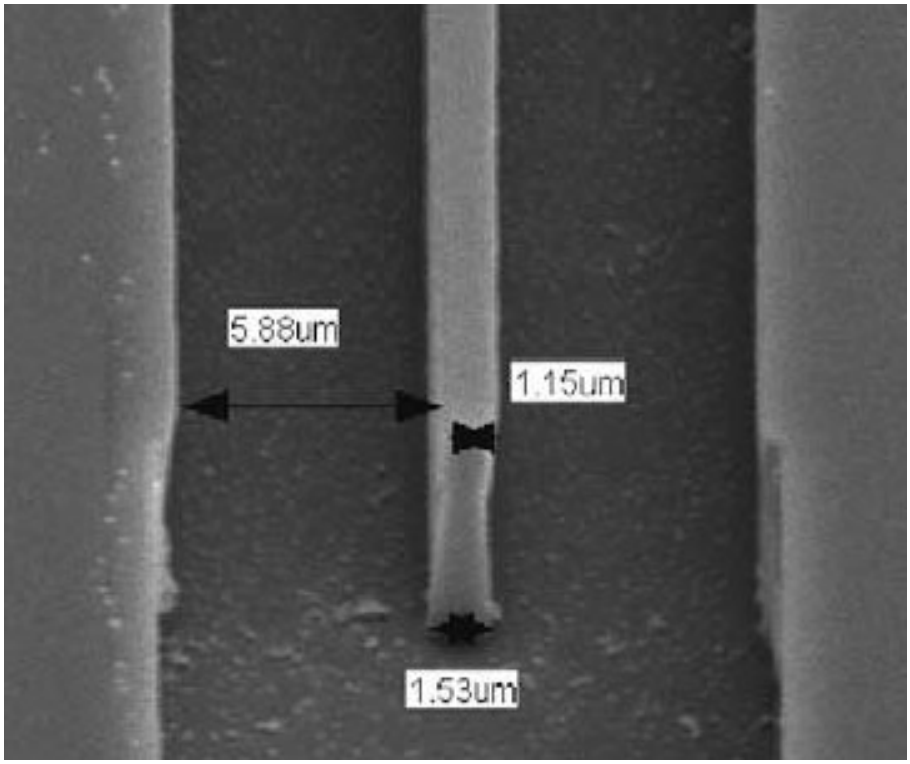

Figure 5.4: High quality SU-8 structures fabricated with UV lithography (reproduced from [33]).

There are some recurring phenomena associated with SU-8. First of all, SU-8 has the tendency to form cracks to release internal stress. These cracks either appear around (dust-) particles or they may appear at corners in the lithographically defined structure. To lower the risk of cracking, therefore particle contamination should be minimized and sharp corners in the design pattern can be rounded in order to distribute the stress along a longer edge. Cracking of the SU-8 film during development is a common problem, and it seems that the density of cracks increase with time the film is developed in PGMEA (propylene glycol monomethyl ether acetate). Therefore the development time should be no longer than necessary. A simple method to remove cracks that may have appeared, is to apply a quick heat treatment, such as 160 °C for 60 seconds. This will in many cases heal cracks. The treatment can be repeated.

SU-8 structures have a tendency to delaminate from the surface, especially if the surface is silica (as opposed to silicon). The delamination releases internal stress in the resist, and the released structures grow about 10% in length and width.

Delamination may be promoted by submerging the substrate containing the thin film in acetone.

Delamination worsens for small ($\sim$10 μm wide) line structures as compared to larger areas. When the aspect ratio of the structures becomes too high (above $\sim$2) the SU-8 seems to yield to the internal stress by elongating and becoming wavy, even though the resist has not delaminated.

As a final comment, even though cross-linked SU-8 can be removed with sulphuric acid, the reaction causes a brown substance which may contaminate other structures.

5.1.2 Electron beam lithography on SU-8

In electron beam lithography (EBL) on SU-8, the photo-initiator is activated by a beam of electrons impinging the resist. The exposure takes place in a vacuum chamber, and a narrow beam of electrons are swept across the resist surface according to the design pattern. The beam delivers a dose (charge per area) dependent on the beam current and sweep speed.

Due to the charge of the electrons, it is necessary that the substrate is conductive, to ensure that the electron beam will not charge the substrate. Charged areas will deflect the electron beam, and thus distort the pattern to be written. In case an insulating substrate is required, a thin metal layer deposited by thermal evaporation on the resist surface can take care of charge removal.

A unique issue that can arise in EBL, is caused by the proximity effect. The effect consists in unwanted exposure of resist in the proximity of the nominally exposed structures. Thus, around the written pattern, one can observe residuals of resist, especially if the written pattern is dense. This exposure of the resist in the proximity of the exposure zones can be reduced by reducing the exposure dose. But there is a lower limit to the dose that can be allowed, since the resist pattern must not be underexposed as this can cause bad structure quality and delamination from the substrate. Usually it is necessary to find a dose that suits a particular pattern, to optimize the result. The 100 keV JEOL electron beam writer at DANCHIP represents the state of the art. The proximity effect worsens with lower beam energies.

The apparatus itself for EBL, consists of a complex electron beam cannon that can be blanked and which has precise control over the direction of the beam of electrons. The resist covered substrate is placed at the target plane of the electron beam. The beam position at the target plane is computer controlled, according to a design file. The exposure necessarily takes place in a vacuum chamber, and loading and unloading of the sample from the chamber are fundamental procedural steps, that may be somewhat time consuming.

Apart from the exposure method (Figure 5.5), the process sequence is of the same type as for UV lithography (Figure 5.2). It may be advantageous to lower the post-exposure bake time and temperature though, since this may increase resolution by minimizing diffusion of the photo-initiator, and be relevant for minimizing the

proximity effect.

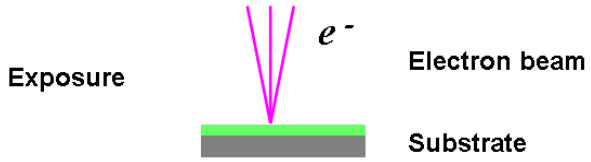

Figure 5.5: Exposure step of resist with electron beam.

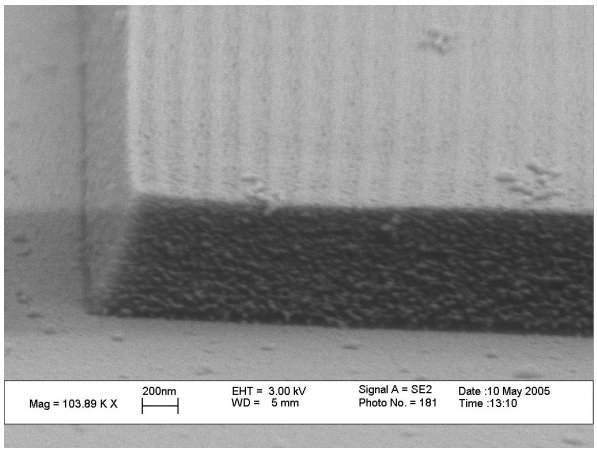

Figure 5.6: Electron microscope image of EBL defined SU-8. A periodic corrugation on the structure has been induced by varying the exposure dose.

Figure 5.6 shows an electron microscope picture of a SU-8 structure defined via EBL. Compared to UV lithography, the corners are very well defined. The radius of curvature appears from the image to lie below 50 nm. The walls of the resist are well defined, and do not exhibit a "skirt". Nor does the top surface curve down before the wall appears, as can be the case for UV lithography (Figure 5.3). Since a 20 nm layer of gold was deposited on the wafer, this may have increased the roughness of the resist surface due to aggregation of metal in islands, rather than a uniform layer. The top surface of the SU-8 has a corrugation with a period of 180 nm, which was made by varying the dose delivered to the resist in a line pattern.

Using a scanning electron beam to irradiate the resist, it is easy (apparatus allowing) to vary the dose delivered to individual areas. Since the height of the developed resist varies with the received dose, this makes it possible to create height variations in the resist, simply by varying, say, the scan speed of the electron beam during exposure. Thus grey scale lithography can be obtained.

The dose curve in Figure 5.7 shows the resist height after development for varying doses applied to the resist (original resist height: 700 nm). The resist height was measured with a surface profiler. The slope on the dose curve makes it possible to control the final resist height, by adjusting the dose delivered to the resist.

Even though the dose curve in Figure 5.7 appears to warrant the possibility of varying the resist height with 40 % or more, the quality of the resist deteriorates with too low doses. Figure 5.8 shows a series of electron microscope pictures of resist structures exposed with doses from 4 to 14 $\mu C/cm^2$. It is apparent that the resist quality is bad for doses below $\sim$6 $\mu C/cm^2$, where a spongy network forms. The sponginess is likely to cause scattering of light, leading to losses for light propagating in the resist. The resist was exposed with a beam energy of 100 keV and a beam current of 0.2 nA.

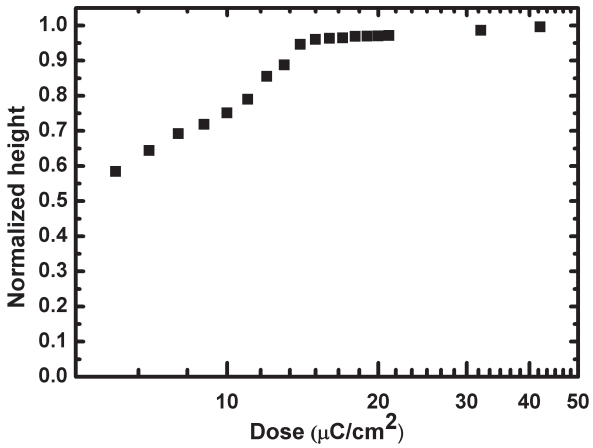

Figure 5.7: Residual height of a SU-8 resist film exposed with varying doses. The original film thickness was 700 nm.

Electron beam canons in electron beam writers can only be scanned reliably within a limited field (500 μm by 500 μm for the DANCHIP EBL apparatus). Larger EBL defined structures are written by "stitching" together write areas. Stitching can lead to errors in the written pattern as present in Figure 5.23 and Figure 8.7. During the work in this thesis, it appeared that stitch errors were worsened slightly when using silicon substrates with a thin (2.5 μm) layer of silica, as opposed to using pure silicon with a thin resist layer. Structures on silica thin films were routinely fabricated during the work in this thesis, however, in an experiment where pure glass wafers were used, the stitch errors were significant (as would have been expected) and the structures unusable.

In conclusion, the major advantage of electron beam lithography, as compared with UV lithography, is the high resolution that can be achieved. EBL also has the advantage that sidewalls become vertical. The edges on the top and the bottom of the resist become sharp, with resolution that seems mostly limited by the resolution of the resist itself.

Although EBL can be used to create structures of superior resolution, it is a rather slow exposure method due to its serial nature. Exposures normally lasts from 20 minutes to half a day, depending on the resolution, dose and structure size. In addition, loading and unloading procedures easily reach half an hour in total. Therefore EBL is a very good tool for prototyping, but obviously not suited for production of large quantities of devices. Large scale production facilities that

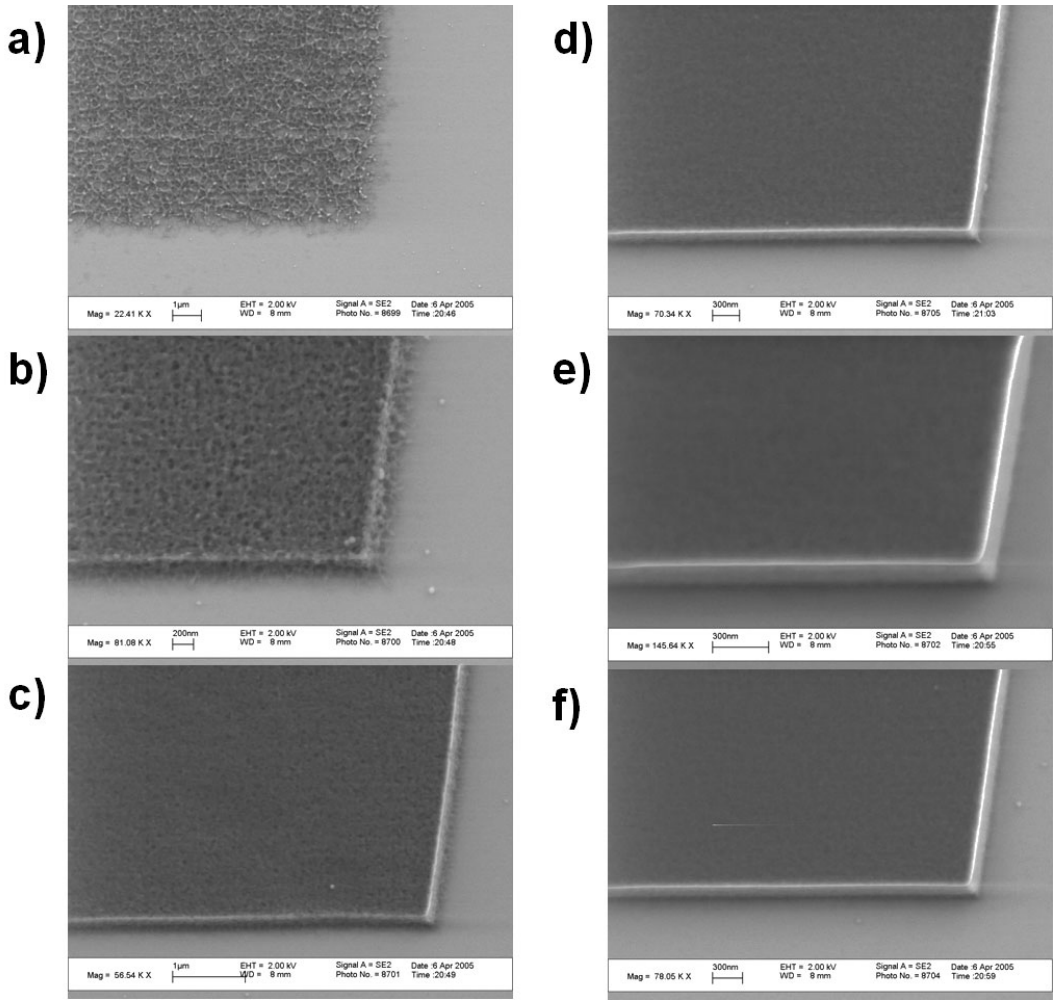

Figure 5.8: Electron microscope images of 500 nm thick SU-8 resist layer on silicon. The resist quality depends on the exposure dose. The doses are; a)4 μ C/cm^2 b) 6 μ C/cm^2 c) 8 μ C/cm^2 d) 10 μ C/cm^2 e) 12 μ C/cm^2 f) 14 μ C/cm^2. (Notice the difference in scale between the images).

need the same type of resolution as EBL can provide, using for example extreme ultraviolet (EUV at 13 nm) radiation. However there appears to also grow a market for medium scale production, where methods such as nanoimprint lithography may be economically advantageous, competing with the very expensive EUV equipment.

5.1.3 X-ray lithography on SU-8

Using X-rays to trigger the photo-initiator is another method to pattern SU-8 resist with very high resolution. The X-rays that have been used in the work described in this thesis, have a wavelength of 0.8 nm (1.5 keV), and thus diffraction has a very small impact on the resolution, as compared to UV lithography. Since the X-ray synchrotron source has a very small divergence, when delivered from a high quality source, this means that high resolution can be obtained even thick

resist layers.

From the experiments I have performed (in cooperation with Dr. Filippo Romanato), it appears that the final resolution is determined by the X-ray mask and the intrinsic resolution of the resist, rather than by diffraction of the X-rays or other factors.

The major feature of the apparatus is the beam source. At the moment, there exist no laboratory sized machine that is able to deliver the intensity needed to do effective X-ray lithography. The beam is delivered by a synchrotron, which is a large scale facility. Figure 5.9 shows the round building housing the synchrotron that was used as X-ray source for the work in this thesis. The synchrotron consists of en electron storage ring with a circumference of 260 m, where bunches of electrons are accelerated to high energies, usually 2 GeV for ELETTRA. The synchrotron radiation itself, is produced by bending the electron beam with magnets and the intensity of the radiation depends on the electron beam current in the synchrotron ring, while the spectrum depends on the energy. The broad spectrum high energy X-radiation is emitted into a so called beam line, which is a dedicated X-ray beam management setup. Figure 5.10 shows a photograph taken down the LILIT beamline that was used as X-ray source for the work in this thesis. For X-ray lithography, the beam line will contain wavelength selective mirrors, that picks out energy ranges of choice.

Below follows a description of the XRL setup at the LILIT beamline at the ELETTRA synchrotron in Trieste, Italy.

Figure 5.9: Aerial photograph of ELETTRA synchrotron facility (from [69]).

At the end of the beam line, the beam tube opens up to free air, the X-rays pass through a beryllium window that ensures a continuous vacuum behind the window (see Figure 5.11). The mask and substrate can be mounted on a so-called stepper in front of the beam exit. The stepper scans the mask and substrate assembly across the beam with a controlled speed. By scanning with different speeds, the X-ray dose reaching the resist can be varied, although the X-ray intensity is fixed by the beamline setup and the synchrotron electron beam current. The beam current drops slowly to half over a period of 36 hours due to loss or electrons in the storage ring. New electron bunches have to be injected to raise the current once more.

Figure 5.10: Photograph down the "LILIT" beamline (from [69]).

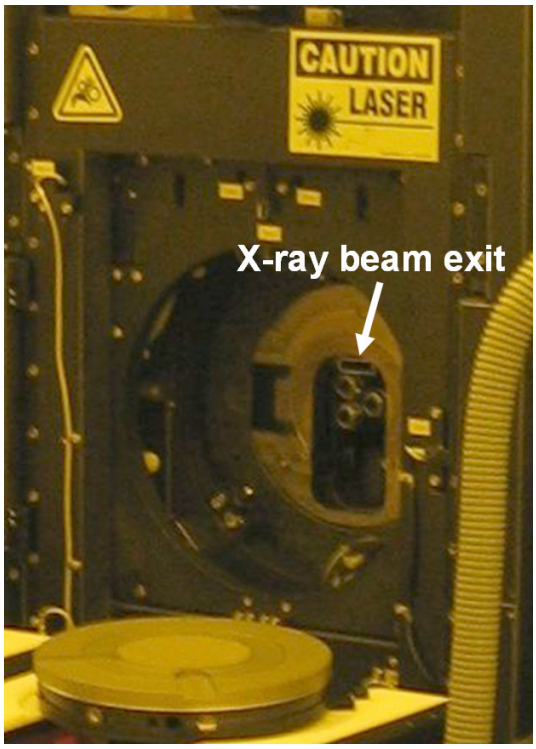

Figure 5.11: Beam exit and stepper at LILIT beamline at the ELETTRA synchrotron facility, Trieste, Italy. The substrate to be exposed is mounted on the stepper plate in front of the X-ray beam exit tube.

In order to avoid ionization of the ambient atmospheric air, the beam tube exit is flooded with helium, which also envelopes to the mask and substrate. The exposure takes place in a lead walled room which must be evacuated of all persons during exposure, and the stepper and beam line is controlled remotely.

Masks for XRL consist of a radiation absorbing layer made of a heavy material on a thin film of a sufficiently light-weight material. This principle is somewhat

different than the principle for masks for UV lithography, since they use reflection or optical opacity to cast a shadow. XRL masks can for example be made of gold on a silicon nitride film. The extinction ratio of the X-rays between the dark and the clear fields of the mask depends on the gold layer thickness. The extinction ratio that is needed, depends on the contrast of the resist. This minimum gold layer thickness, which was found to be 650 nm [70], increases the difficulty of fabricating the mask, since high (650 nm) vertical walls of metal have to be fashioned with a wall quality sufficient for the application (peak to peak roughness of ∼40 nm for optical purposes).

In order to fabricate thick heavy metal structures with vertical walls, they are made via an electroplating process. The mask fabrication sequence consists of the following steps; 1) preparation of thin silicon nitride film with thin gold layer and a resist layer, 2) definition of resist free areas via EBL, where gold is to be electroplated 3) electroplating of gold and 4) removal of EBL resist. The fabrication steps for making a mask are shown in Figure 5.12.

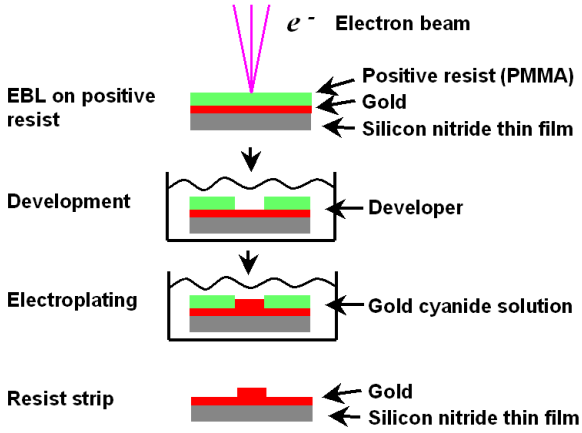

Figure 5.12: X-ray mask fabrication steps.

During the exposure step of the resist film, the mask is placed in contact with the resist and mounted in the X-ray beam path on the stepper. The lithographic process is much the same as for UV lithography, except for the radiation type and the mask type. It is necessary to adjust post-bake time and temperature to optimize the process.

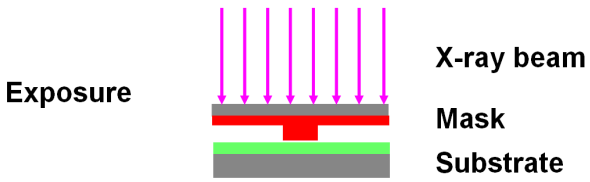

Figure 5.13: Principle of exposure step with X-rays. The resist underneath thick mask areas will receive less X-ray dose than resist under areas where the mask is thin.

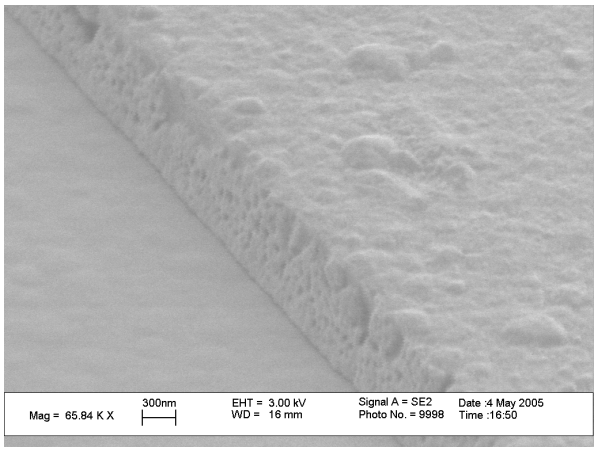

Figure 5.14: Electron microscope image of gold X-ray mask detail.

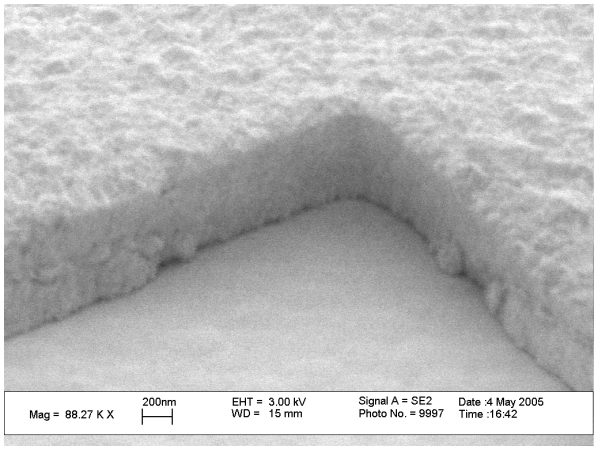

Figure 5.15: Electron microscope image of gold X-ray mask detail.

Figures 5.14 and 5.15 show electron microscope pictures of details of X-ray masks with gold on a silicon nitride membrane. The masks were fabricated in Trieste, Italy, in cooperation with Dr. F. Romanato. The top surface of the gold layer is somewhat rough due to the roughness induced in the electroplating process. However, it is the roughness on the sidewalls which is critical, since variations on the walls lead to edge roughness on the final resist in the form of vertical stripes. Although it was not possible to fabricate masks with lower side wall roughness than in Figures 5.14 and 5.15, the stripe formed roughness induced by the mask on the final resist, appeared to be of the same magnitude as the intrinsic roughness of the resist. The thickness of the gold on the mask in the figures is approximately 600 nm. It should be mentioned that the thickness varies as a function of the pattern density due to the electroplating process, which is sensitive to this factor. This can create problems if a mask contains both dense small structures and large wide structures.

Figure 5.16 shows an electron microscope image of a common phenomena in XRL

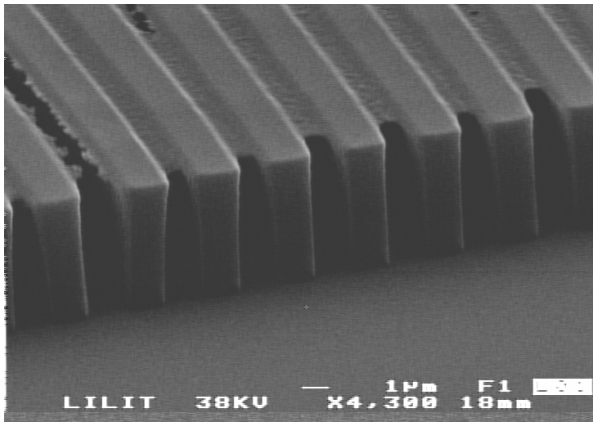

Figure 5.16: Electron microscope image of X-ray fabricated SU-8 structure. A top surface film is present due to overexposure.

on SU-8. The surface of the resist has polymerized after the post-exposure bake plus development and forms a film on top of the nominal resist pattern. The film can be eliminated by lowering the X-ray dose, which indicates that the film is caused by the residual X-rays penetrating the shadow areas of the mask. If the mask contrast is too low, it is not possible to lower the dose enough, without underexposing the SU-8. It may be conjectured that the surface of the SU-8 resist is, for some reason, more sensitive than the bulk, which is why a surface film appears, even though the absorption of the X-rays through the resist is low due to the low density of the hydro-carbon based material.

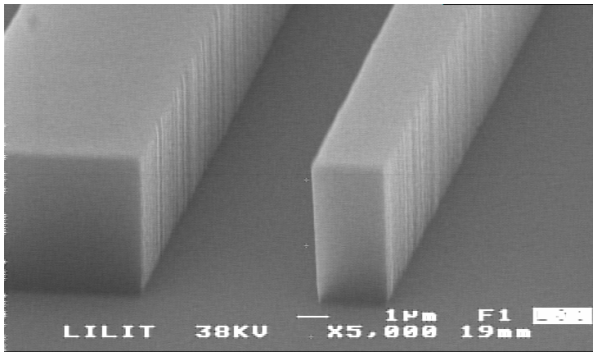

Figure 5.17: Electron microscope image of optimized X-ray fabricated SU-8 structure.

Figure 5.17 shows a typical result of an optimized XRL process on a 6 μm SU-8 layer. The structure is well defined, with minimal (but present) "skirting". Vertical stripes on the side walls are clearly present, and is caused by mask side wall roughness. Figure 5.18 shows an electron microscope image of another optimized structure.

Figure 5.19 shows SU-8 structures made by exposing the mask and substrate assembly to the X-ray beam in an angle of 45 degrees, instead of the normal 90 degrees, see also Section 8.3. Synchrotron X-radiation is uniquely effective for

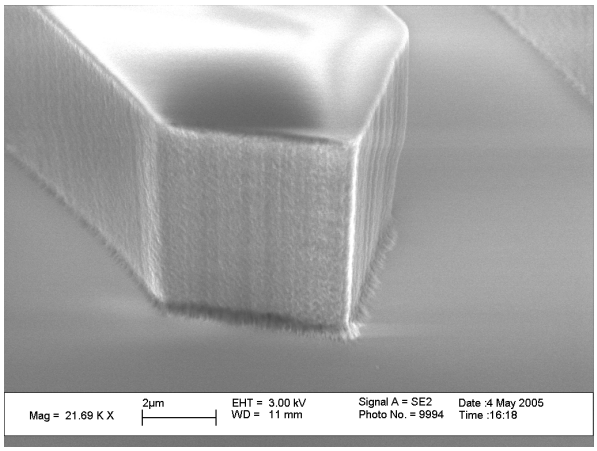

Figure 5.18: Electron microscope image of X-ray defined SU-8 structure.

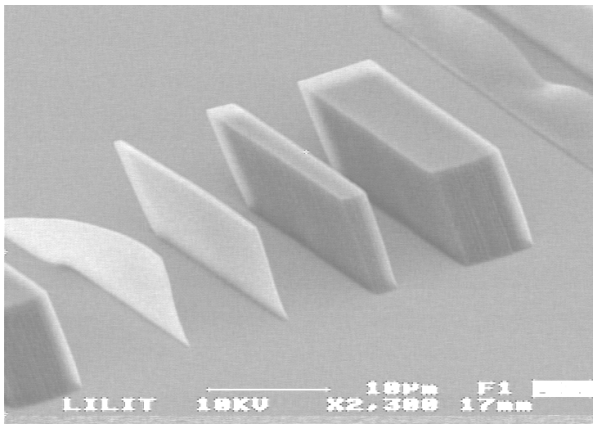

Figure 5.19: Electron microscope image of SU-8 structures made by angled X-ray exposure (45°).

making this kind of angled high resolution exposures due to the low dispersion of the X-ray beam. This is near to impossible in EBL due to the problem of keeping the beam focus stable. UV lithography is a candidate for making the sort of structure, although with lower resolution and it would require a collimated source, for example from a UV laser. Finally, nanoimprint lithography can create levelled imprints, however it is not possible to make negative slopes on the sidewalls of the resist.

In conclusion, as with UV lithography, the quality of the mask can limit the quality of the resist pattern. For UV lithography, fabricating masks that are of sufficient quality, such that other factors limit the final pattern quality is fairly easy. But making X-ray masks for lithography on SU-8 is somewhat more demanding, and the masks must be produced by oneself.

Even with sensitive chemically amplified resists as SU-8, the X-ray beam brightness needs to rather high as the required dose is $\sim$35 mJ cm^{-2}. Thus large synchrotron facilities are necessary to produce the appropriate radiation, until

bright table-top sources are available. So, even though X-ray lithography is a rather fast and easy process, the scarcity and expense of the beam source limits the commercial and research applications.

5.1.4 Nanoimprint lithography on thermoplasts

Unlike the three previous lithographic methods described above, nanoimprint lithography (NIL) is not based on radiation driven chemical changes in the resist, but rather on mechanically induced material relocation. Eliminating radiation sources in the lithographic process, removes all the problems related to waves (and energetic charged particles); diffraction, absorption, scattering and charging. NIL has other kinds of limitations, but the resolution that can be achieved depends entirely on the stamp, and not on the contingencies of the lithographic process. Even the type of intrinsic resolution limit that is observed for SU-8 (and other resists) becomes irrelevant, since the structure is determined by mechanical forces, rather than by changes in chemical nature of the resist and wet chemistry during development. Therefore NIL can in principle surpass all radiation based lithographic techniques, with respect to parameters such as resolution and roughness of the surfaces.

In the NIL process, a film of thermoplastic resist on a substrate is patterned with a stamp that is pressed down on the resist while the assembly is heated to above the glass temperature of the resist. The thermoplastic resist will then conform to the stamp. Subsequent cooling of the resist, brings the resist below the glass temperature again, and the stamp pattern remains in the resist after separation of the stamp and the resist coated substrate. The imprint process is illustrated in Figure 5.20. There will always remain a residual layer of resist under the stamp protrusion areas, which has to be taken into account in further processing.

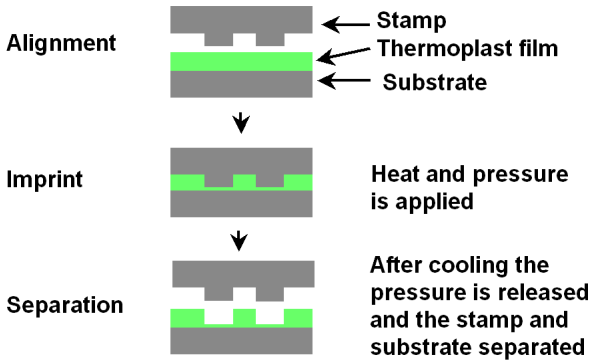

Figure 5.20: Fabrication steps during imprinting.

The apparatus used for NIL consists of flat plates that can be pressed together with an adjustable force. The plates can be heated and cooled, and substrate and stamp can be mounted on the plates. During operation, the temperature and pressure is controlled with a computer (in advanced setups). To enhance the

imprint uniformity, rubber like materials can be inserted in between the plates and the substrate.

The process steps for NIL depends on the type of imprint that is fabricated. In case the imprinted polymer itself forms a device (for example an optical structure as in Section 6.5), the process sequence is; 1) spin deposition of thermoplast, with subsequent bake-out of solvent, 2) imprint and 3) separation of substrate and stamp.

The separation of substrate and stamp can be somewhat difficult, however there exist high performance anti-stiction coatings that can be applied to the mask, in order to ease the separation step.

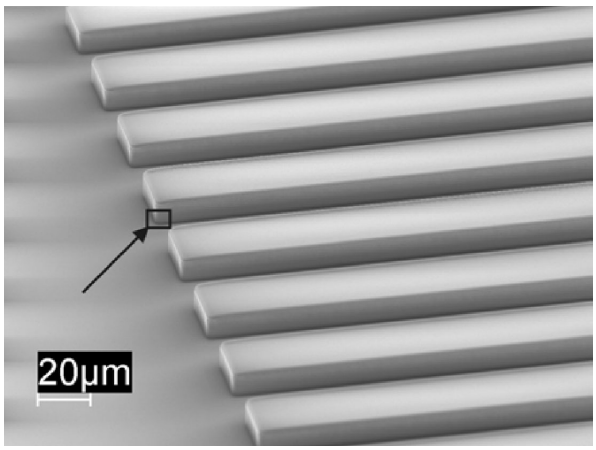

Figure 5.21: Electron microscope image of 26 µm wide structures made with thermal nanoimprint lithography. The box with the arrow indicates the zoom illustrated in the Figure 5.22 below.

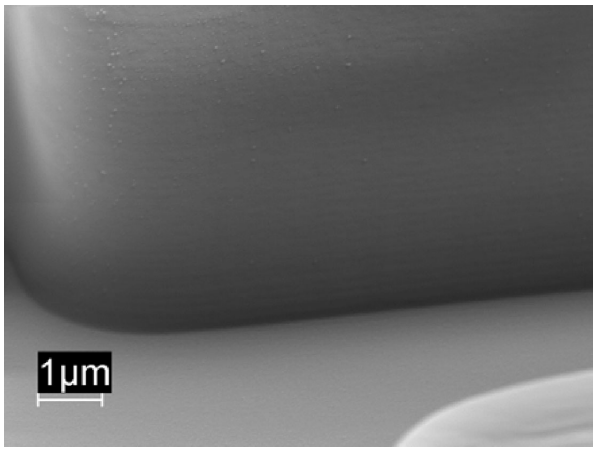

Figure 5.22: Electron microscope image of 26 µm wide structures made with thermal nanoimprint lithography. The structure is a detail of the figure above.

Figure 5.21 and Figure 5.22 show nanoimprinted structures in COC. The pattern is the same as the pattern in Figure 5.3. The imprinted structure has vertical

sidewalls, no "skirting" and a flat top surface. The smoothness of the surfaces, which reflect the smoothness of the stamp, is achieved by applying a "smoothing step" (described in [71]) to the stamp. This, however, has the effect that the corners become somewhat rounded as seen in the closeup in Figure 5.22. It should be immediately obvious from the images, that the quality that can be achieved with NIL is very good.

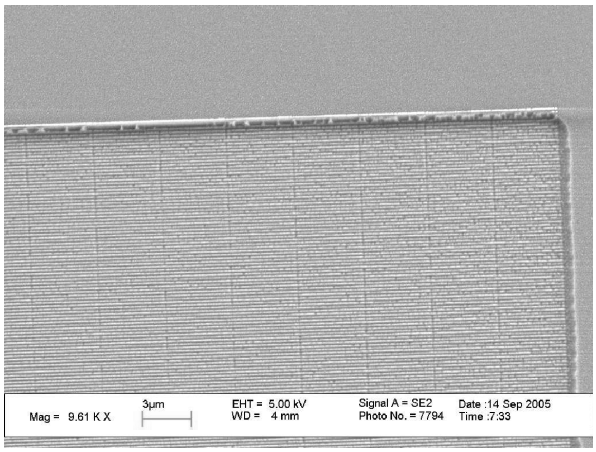

Figure 5.23: Electron microscope image of silicon stamp with corrugation with a pitch of about 200 nm.

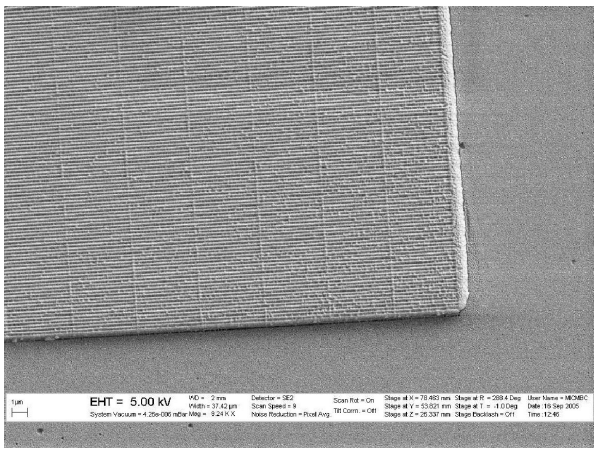

Figure 5.24: Electron microscope image of PMMA structure made via imprint in a thin film of PMMA of the stamp in the figure above.

Figure 5.23 shows a silicon stamp and Figure 5.24 shows the imprinted structure in a 680 nm thick PMMA layer [72]. The stamp contains 200 nm features that seems to be perfectly transferred to the PMMA resist (Figure 5.24).

The time necessary for a complete imprint step can be long, half an hour or more. The imprint time could be shortened significantly if the temperature could be varied quickly, especially cooling the large pressure plates in the imprint operation is time consuming. The temperature cycle time could be shortened by, for example, lowering the thermal mass of the system.

The residual layer (see Figure 5.20) is unavoidably present after imprint. If the imprinted polymer itself forms the device, then this residual layer must be thin enough not to disturb the functionality of the device. This is particularly relevant for optical components, where the imprinted structures have a waveguiding functionality. In this kind of components, it is obvious that the residual layer should be thin enough, not to be able to support confined propagating modes.

5.2 Summary

In summary, several factors may be relevant when deciding which lithographic technique to use for SU-8. Table 5.2 aims to sum up pros and cons of the different lithographic methods.

Method	Price	Resolution	Mask price	Availability	Roughness	Throughput
UV	+	−	+	+	+	+
EBL	−	+	+ †	−	+	-
XRL	−	+	−	−	− ‡	+
NIL	+	+	−	+	+	+

† No mask necessary. ‡ The roughness depends on the mask, see text.

A few comments in connection with Table 5.2: The price varies a lot and UV lithography is by far the cheapest process. The actual cost of NIL is difficult to determine yet, since this lithographic method is still under development. Only UV lithography has a significantly lower resolution than the other types of lithography due to the wavelength of the light. The mask price for XRL and NIL is high since the masks must be fabricated with expensive techniques (i.e. EBL). A UV lithography setup and a nanoimprint setup are fairly easy to install in a clean-room laboratory, while machines for EBL and especially XRL require more resources and are therefore more rare. The side wall smoothness of the XRL fabricated devices have not been of superior quality in the work presented in this thesis, however, in principle the roughness depends on the mask, which it may be possible to fabricate with a higher quality than what has been obtained in the present work. Finally, the throughput per device on a wafer must be considered. EBL is significantly slower than any of the other methods.

There is an abundance of resist types apart from SU-8, and new resist types are being developed. For example new types of SU-8 itself, are being developed with a lower dispersion of the size of the resin molecules, leading to a higher contrast of the resist. It is recommendable to research the appropriate new resist types in the design phase of new components.

Chapter 6

Fabricated lasers

This chapter describes a number of lasers that were developed and investigated during the work described in this thesis. The devices were all fabricated at MIC and DANCHIP except for devices fabricated with X-ray lithography, which were fabricated at the ELETTRA synchrotron facility in Trieste, Italy. All optical characterization was performed at MIC.

Some devices were investigated in collaboration with other Ph.D. students and master students at MIC. The contributions to each investigation is mentioned in a footnote at each description.

6.1 Laboratories

The DANCHIP clean-room facility (class 100) was used to fabricate all devices, apart from devices fabricated with X-ray lithography. All machines for fabrication was located inside the clean-room except for the dicing saw used to cut out chips from wafers and the diamond drill. More information about the current DANCHIP cleanroom facilities are available at http://www.danchip.dtu.dk/.

An optical laboratory was used to characterize the fabricated devices with respect to their light emission during optical pumping (Figure 6.1). The two most important pieces of equipment was a frequency doubled Nd:YAG laser and a CCD based spectrometer. The Nd:YAG laser was a Continuum Surelite I-10 which consisted of a flash lamp pumped Nd:YAG rod placed in a Q-switched optical cavity. The lasing action of the Nd ions takes place at 1064 nm and the intense pulses of infra-red light were frequency doubled in a non-linear crystal, yielding 532 nm (green light). Various optics delivered the green light to a sample platform, where the polymer light source devices under investigation could be placed. The specified pulse width of the pump laser was 5 ns and the repetition rate could be varied from a single shot to 11 Hz. The spot profile of the laser was flattened before the light met the non-linear frequency doubling crystal, in order to increase conversion efficiency. However, this flattening leads to some fringe structures in the mode, which must be taken into account when aligning the polymer devices under investigation to the pump beam from the Nd:YAG laser.

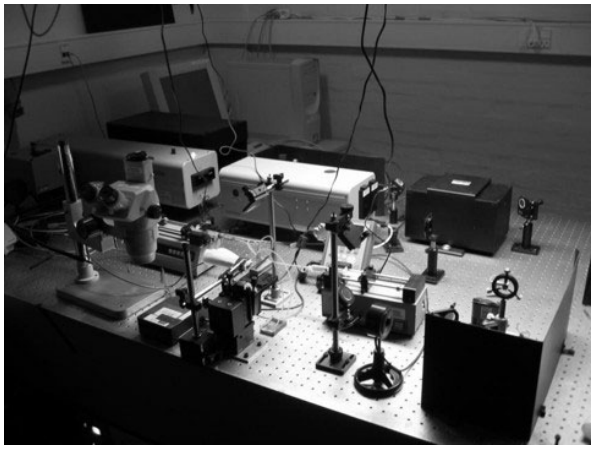

Figure 6.1: Photograph of the optical characterization laboratory showing the setup used to characterize the polymer laser devices.

The spectrometer that was used to measure the output spectra from the devices under test, was from Avantes and based on a fixed grating and a linear CCD array. The spectrometer was interfaced with a desktop computer. A multimode fibre with a core diameter of 200 μm delivered the light to be measured to the spectrometer. In all experiments the other end of the fibre directly picked up the light emitted from the dye light sources into free space. The fibre was placed 1 mm to 5 cm from the devices under investigation, depending on the intensity of the emitted light. The spectrometer had a wavelength resolution of 0.15 nm (FWHM of the response to a very narrow line laser) and distinguished light in 4000 levels. Due to this limited dynamic range, the side mode suppression ratio (SMSR) for the lasers could not be measured reliably. Even so, the lasers in this thesis that clearly operated in a single dominant mode are termed "single mode".

The available laboratory equipment only made it possible to measure the output energy of one type of laser device (the microfluidic high order Bragg grating DFB laser). Therefore this important parameter could not be determined for most lasers.

For the rest of this thesis, when "the spectrometer" or "the Nd:YAG laser" is mentioned, it refers to the equipment described above.

6.2 Laser overview

Several kinds of lasers are presented below. They are based on different feedback mechanisms and the gain medium either consists of the laser dye Rhodamine 6G embedded in a polymer matrix or of a liquid solution of Rhodamine 6G.

The following lasers are described:

- Metallic mirror laser [73]
- Three layer trapezoid laser [74]
- High order Bragg grating DFB lasers [75, 76, 77]
- First order Bragg grating DFB lasers [25]

The devices with grating based feedback could operate in a single mode, due to the wavelength dependence of the reflection from the gratings. On the other hand, the lasers using metallic mirrors or total internal reflection (the trapezoid laser) all operated in multiple modes and were not fully monochromatic.

6.2.1 Fluidic dye lasers

The two types of fluidic dye lasers presented below in Section 6.3 and 6.5 are based on liquid solutions of the laser dye Rhodamine 6G, flowing through microfluidic channels on the laser chips. This makes it possible to vary parameters in real time, such as the refractive index of the fluid and the concentration of the laser dye, during operation of the laser. Furthermore, the microfluidic channel makes it possible to replenish with new dye solution if the dye molecules in the laser should photo-bleach.

Due to the microfluidic channels, the laser chips must be sealed off by a lid. The lid will also form part of the optical structure, and the materials must be chosen under observation of both optical and bonding properties. Optically, the lid forms the cladding of a waveguide structure, and must therefore present a lower refractive index to the propagating light wave than the waveguide core (except for the laser based on metallic mirrors in Section 6.3, that does not utilize the waveguiding effect).

The microfluidic network on the chips were made by forming the channel pattern in a thin-film of polymer (for example SU-8) on a substrate. The lid was bonded to the chips by means of a thermoplastic polymer thin-film (for example PMMA) on a separate substrate, thereby sealing the channels. The final sandwich consisted of a bottom wafer, a patterned thin-film, a thermoplast thin-film and a top substrate. To access the channels, holes were drilled through the lid or the bottom substrate. Due to the hardness of the materials - glass or silicon - a diamond encrusted drill or sand blasting had to be used to make the holes. Both methods create a lot of dust, and care has to be taken if further clean room work is necessary for drilled devices. Also the dust may settle in the microfluidic network.

6.2.2 Solid state dye lasers

The solid state dye lasers and ASE devices presented in Sections 6.4, 6.5, 6.6, 8.1, 8.2 and 8.3 are all based on Rhodamine 6G embedded in polymerized SU-8 or in PMMA. The shape of the doped polymer defines the optical resonators.

Embedding dye in the solid polymer matrix that also forms the laser resonator, has the obvious disadvantage that bleached dye cannot be replenished, and the lasers have a lifetime that is limited by bleaching of the dye. However, judging whether the lifetime is short or long depends on the application, since the lasers can last several hundred thousand pulses. Considering the case where each pulse entails a measurement, the number of measurements is large.

It is an obvious advantage of using embedded dye that the laser is ready for use "as is", and does not require an external liquid dye source and fluidic connection to the chip.

6.3 Metallic mirror laser with vertical output

One of the first types of microchip lasers that was developed at MIC by Bjarne Helbo and Anders Kristensen [9], was based on a pair of opposing flat metallic mirrors, with the gain dye solution located in-between the mirrors. In the work described in this section[1], the metal mirror laser type was integrated with a microfluidic mixer and the response to varying parameters of the fluid was investigated.

The simple metal mirror resonator surrounding a microfluidic channel formed a test-bed for exploring the influence of the dye concentration and the refractive index of the dye solvent on the emitted light from the device during optical pumping. As mentioned in Section 4.2.1, the position and shape of the spectral gain peak depends on several parameters, among these are the dye concentration and the solvent (and thereby the refractive index), which could be easily changed in the chip device described below. Since the chip contained a microfluidic mixer, the fluid parameters could be varied in real time by changing the flows into the two inlets of the mixer.

The laser resonator (see Figure 6.2) consisted of two metallic mirrors located on the top and the bottom of a 1 mm broad and 7.5 μm high microfluidic channel as illustrated in Figure 6.3. The channel was filled with an ethanolic solution of Rhodamine 6G, which was optically pumped with a frequency doubled Nd:YAG laser through the semi-transparent top mirror (power reflectance: 0.72). The top mirror both coupled out light from the laser and permitted pumping light to reach the dye solution between the mirrors.

The bottom metallic mirror covered the entire chip, while the top mirror covered an area of 1 mm by 1 mm. The mirrors were only separated by the 7.5 μm

[1] My contribution to this work has consisted in optical characterization and analysis of the measurement results.

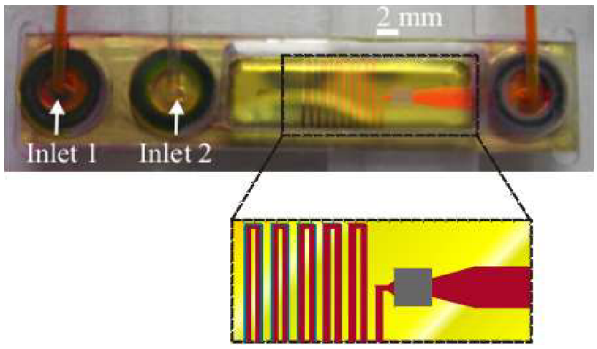

Figure 6.2: Photograph of the metal mirror laser mounted in a sample holder with fluidic connections. The chip contains a microfluidic mixer and the mixed dye fluid is carried to the resonator area (grey square) via a meander. For clarity, the lower part shows a drawing of a closeup of the meander and laser area.

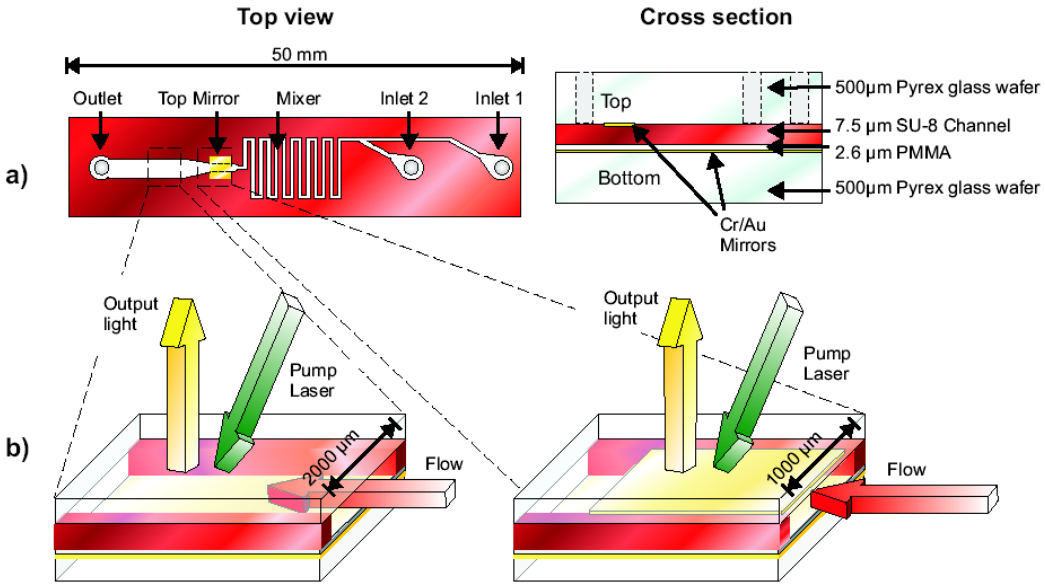

Figure 6.3: a) Top view and cross-sectional view of metal mirror laser device. Two inlets (1 and 2) allow fluids into the microfluidic channels, where the fluids are mixed and directed through a meander to the laser resonator which is located at the top mirror. The cross section shows the layered structure of the chip. b) Sketches of an area of the microfluidic channel with only a bottom mirror and an area with both a bottom and a top mirror.

high channel and by the 2.6 µm thick layer of PMMA used for bonding the glass lid to the SU-8. The extension of the mirrors were therefore much larger than the distance between the mirrors. Under usual free-space optics circumstances, two flat mirrors placed some distance apart would yield a quite lossy resonator due to the non-confinement of the light. However, the loss caused by diffraction at the edge of the mirrors in the integrated resonator is negligible compared to the loss posed by the semi-transparent top mirror. It can be expected that the integrated metal mirror resonator is modelled sufficiently well as a simple Fabry-Pérot resonator. The power reflectance on the dielectric interface between the

ethanol and PMMA is negligible (R=0.3%). The expected transmission response of the micro-resonator, calculated via the formula below (from [78]), is illustrated in Figure 6.4. The mode spacing is 10.9 nm from the Fabry-Pérot free spectral range expression $\Delta\lambda = \lambda^2/(2L)$,where λ is the wavelength of the light and L is the optical path length between the mirrors. In the case of the metallic mirror laser $L = (n_1 L_1 + n_2 L_2)$, where $n_1 = 1.33$ and $L_1 = 7.5$ μm are the refractive index and channel height for the fluid channel (containing ethanol), and $n_2 = 1.49$ and $L_2 = 2.6$ μm are the refractive index and the thickness of the PMMA bonding layer.

$$\frac{I_{\text{transm}}}{I_{\text{in}}} = \frac{(1-R_1)(1-R_2)}{(1-\sqrt{R_1 R_2})^2 + 4\sqrt{R_1 R_2}\sin^2(L2\pi/\lambda)} \tag{6.1}$$

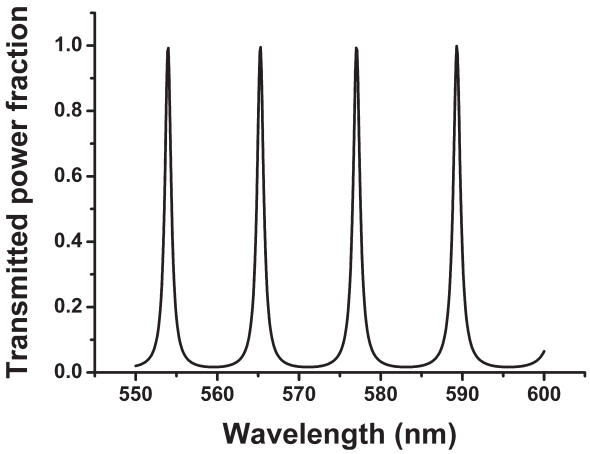

Figure 6.4: Transmitted power fraction through a resonator with mirrors having power reflectances 0.72 and 0.83 located 13.8 μm from each other. The mirror distance corresponds to the optical path length (geometric length times refractive index) in the metal mirror resonator. The reflectances correspond to the values for the metal mirrors. Losses are not taken into account.

According to the design, the top mirror has a power reflectance of 0.72, a power transmittance of 0.06 and a power absorbance of 0.22 at a wavelength of 570 nm. The bottom mirror has a power reflectance of 0.83, a power transmittance close to 0 and a power absorbance of 0.17 at a wavelength of 570 nm [79].

The fabrication of the laser takes several process steps (see Figure 6.5). Two Borofloat glass substrates were used. The bottom metallic mirror that covered the whole wafer was deposited via electron-beam assisted evaporation on the first of the glass substrates. The mirror consisted of 10 nm chromium and 150 nm gold, deposited in a two step process. The chromium acts as an adhesion promotor for the gold. A 7.5 μm thick layer of SU-8 photoresist were deposited in a spin coating step on the first wafer (on top of the gold) and pre-exposure baked on a hotplate with 65° for 2 min and 90° for 2 min with slow heating and cooling. The SU-8 was illuminated through a mask in a standard UV lithography step with a dose of 490 mJ cm^{-2} and post-exposure baked with 65° for 2 min and 90° for 15 min with slow heating and cooling. The SU-8 was developed in PGMEA for 4 min.

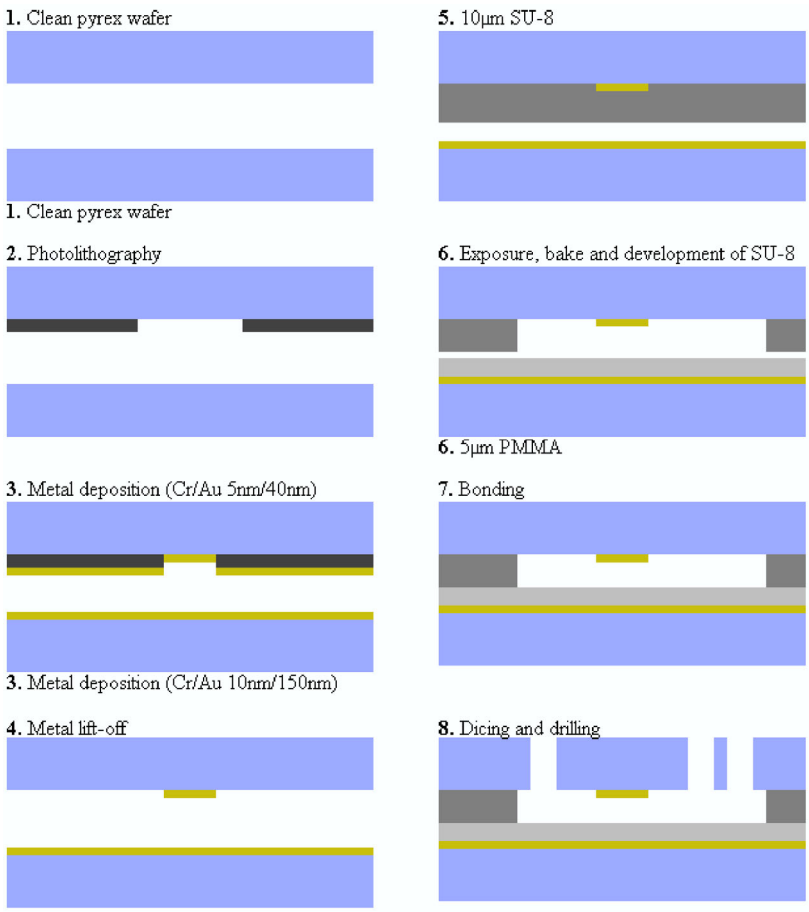

Figure 6.5: Process steps for fabrication of the metal mirror laser.

The 1 mm by 1 mm metallic mirrors on the top of the microfluidic channels were defined on the second glass substrate using UV lithography, metallization and lift-off of the metal on the remaining resist in a developer. Electron-beam assisted evaporation metallization was used to deposit 5 nm chromium and 40 nm gold. The lid containing the 1 by 1 mm metallic mirror was bonded to the substrate via PMMA mediated bonding [30]. This both formed the micro-resonators and sealed the microfluidic channels. The bonding layer consisted of a 2.6 µm thick 950k PMMA layer deposited via spin-coating. The holes for the inlets and outlet were diamond drilled.

The chip was used to examine the character of the emitted light as function of the Rhodamine 6G dye concentration in the microfluidic channel. For the examination it was mounted in a polycarbonate holder, see Figure 6.6. Figure 6.7 shows output spectra from the metal mirror resonator, when optically pumped with a pump energy density of 58 µJ mm^{-2}. The incidence angle of the pump beam on the chip was approximately 45°. The concentration of Rhodamine 6G dye in the microfluidic channel flowing through the two metal mirrors was changed by altering the relative flow rate into the two mixer inlets of pure ethanol and a 0.1 mol/L ethanolic solution of Rhodamine 6G controlled by syringe pumps. The

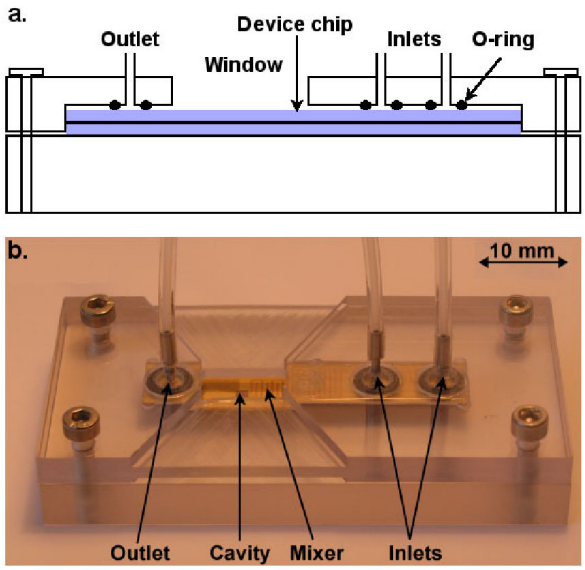

Figure 6.6: Metal mirror laser device holder. a. Schematic illustration of the device holder. b. Photograph of device holder with a device chip and inlet/outlet tubes mounted.

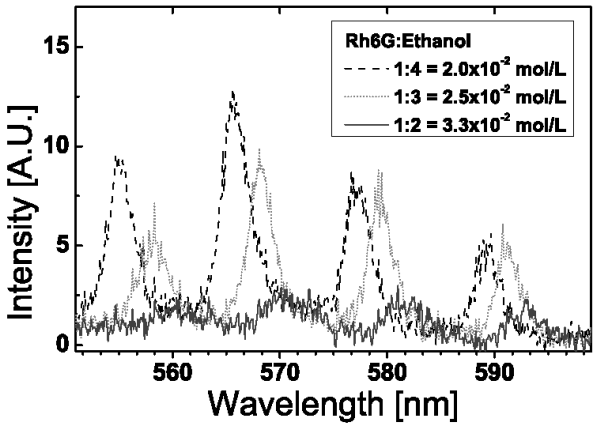

Figure 6.7: Output spectrum from the metal mirror laser for varying concentrations of Rhodamine 6G in ethanol. The pump energy density was 58 µJ mm^{-2}. The label indicates the relative flow rate of pure ethanol and a 0.1 mol/L ethanolic solution of Rhodamine 6G controlled by syringe pumps.

output spectra in Figure 6.7 resembles multi mode lasing, with a mode distance of 11.5 nm. However, it is not determined if it is lasing or fluorescence enhanced by the resonator. As the dye concentration changes, the spectrum shifts. This shift is most probably caused by a change in the refractive index posed by the fluid solution. The phase condition for a Fabry-Pérot resonator is $2\pi q = 2kdn$, where $q = 1, 2, 3, ...$, $k = 2\pi/\lambda$, d is the mirror distance and n is the refractive index between the mirrors. The change in wavelength with refractive index is $d\lambda/dn = 2d/q$. For the cavity defined by the metallic mirrors, $q\lambda = 2(n_1L_1 + n_2L_2)$, where n_1 and n_2 are the refractive indices of the dye solution and the PMMA layer, respectively, L_1 and L_2 are the thicknesses of the microfluidic channel (7.5 µm)

and the PMMA layer (2.6 μm) and q is the mode number (found to be 49). The tuning range determined from the spectra in Figure 6.7 is $\Delta\lambda = 4$ nm, which corresponds to a change of refractive index of: $\Delta n_1 = 0.013$. Expressed as $\Delta n_1/\Delta c$ this gives 1 L/mol (or $2.2 \cdot 10^{-3}$ L/g), where Δc is the concentration change. The value is comparable to the value in [80] for Rhodamine B in ethanol at 570 nm, which can be found from the graph in Figure 6.8 to ∼0.8 L/mol. This large value is connected to the anomalous dispersion curve around the molecular resonance.

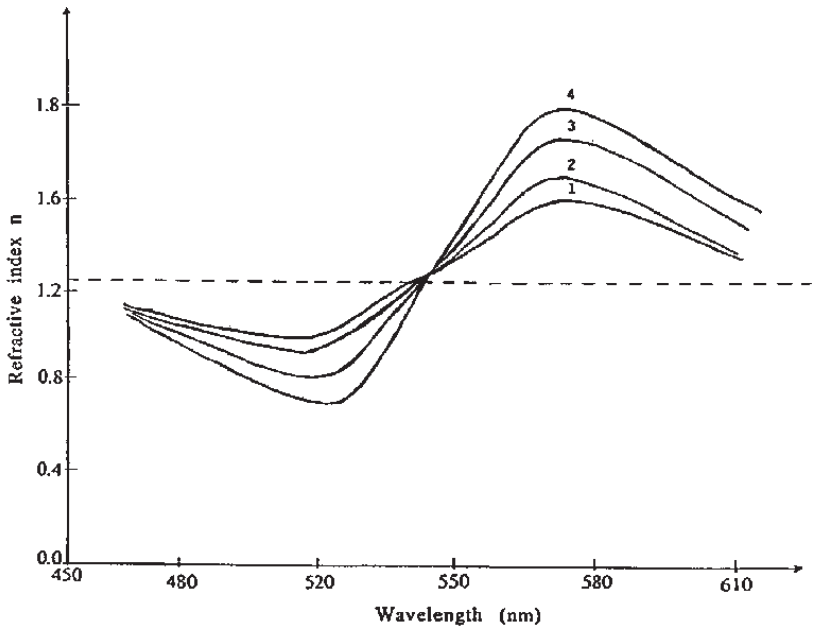

Figure 6.8: Absolute refractive indices versus wavelength for different temperatures: dashed line, ethanol; solid curves, 0.45 mol/L Rhodamine B in ethanol. 1, 23°C; 2, -5°C; 3, -20°C; 4, -70°C (reproduced from [80]).

The spectrum shift measurement is a reminder of the fact that the exact refractive index is not simply found by considering the material in which the dye is dissolved. In addition, the dispersion curve may be altered when the dye is optically pumped. When modelling laser structures, this state of affairs must be kept in mind during interpretation of the results.

Figure 6.9 shows the response from pumping the microfluidic channel outside the area of the metal mirror resonator with a pump energy density of 111 μJ mm^{-2} and an incidence angle of approximately 45°. The optical response from the dye in the microfluidic channel appears to be laser like (see the pump curve in Figure 6.10), however the response may well be a mixture of amplified spontaneous emission (ASE) and lasing. The lasing may arise from feedback from the bottom mirror in combination with reflection at the air-glass interface (∼5%) at the chip surface, or it may arise due to the volume grating induced by the angled 532 nm pump beam that is also reflected on the bottom mirror. In either case, the measurements illustrated in Figure 6.9 show the stimulated emission response at four dye concentrations. The response peak shifts in wavelength as function of the concentration due to the Stokes shift effect described in Section 4.2.1.

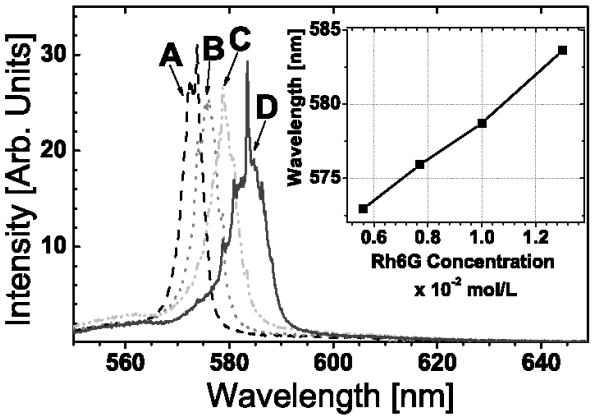

Figure 6.9: Output spectra from optical pumping with 111 µJ mm^{-2} of the microfluidic channel (away from the metal mirror resonator). The four spectra corresponds to Rhodamine 6G concentrations of A: $5.6 \cdot 10^{-3}$ mol/L, B: $7.7 \cdot 10^{-3}$ mol/L, C: $1.0 \cdot 10^{-2}$ mol/L and D: $1.3 \cdot 10^{-2}$ mol/L. The peak position moves from 573 nm to 583 nm. Inset: The peak wavelength as function of dye concentration.

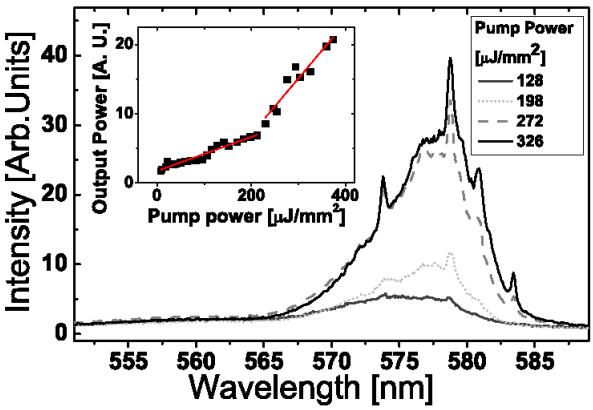

Figure 6.10: Output spectra from the microfluidic channel during pumping with increasing pump energy densities. The microfluidic channel contained a 0.01 mol/L Rhodamine 6G solution in ethanol. Inset: The pump curve shows the output power as function of pump power.

Figure 6.11 shows the optical response from the dye in the microfluidic channel when the inlet flow rates are changed at time $t = 0$. The flow rates were changed from 2.5 µL/hr Rhodamine 6G (at a concentration of $2{\cdot}10^{-2}$ mol/L) and 7.5 µL/hr pure ethanol to 5 µL/hr Rhodamine 6G solution and 0 µL/hr pure ethanol. This corresponds to a concentration shift from $5 \cdot 10^{-3}$ mol/L to $2 \cdot 10^{-2}$ mol/L. The response time of the mixer is about 60 seconds. After this time, the solution begins to change concentration at the mixer output. It takes another 50 seconds to reach a steady state. This demonstrates the functionality that can be expected from the type of diffusion mixer integrated on a chip.

In conclusion, the investigations performed with the chip have clarified aspects of the optical behavior of Rhodamine 6G, both with respect to the refractive index

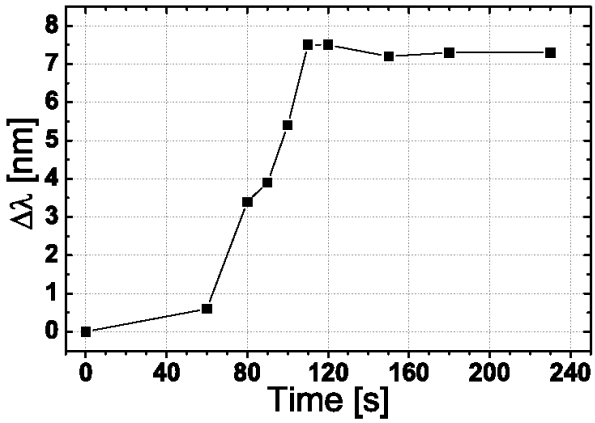

Figure 6.11: Graph of the center wavelength shift with time when the inlet flow rates are changed. The microcfluidic channel was optically pumped away from the metal mirror resonator. The relative flow rate is changed at $t = 0$.

exhibited by a Rhodamine 6G doped material and with respect to the variability of the stimulated emission spectra.

6.4 Three layer trapezoid laser

For lab-on-a-chip applications of the miniaturized dye lasers, it is advantageous to have lateral output. This makes it possible to couple the light directly into other components on the chip, such as waveguides. It is therefore preferable that the optical resonator operates in the lateral direction (in the chip plane). Because it is impractical to deposit metallic or dielectric mirrors on the low vertical surfaces of the patterned resist, resonators defined only in a single polymer layer have been designed. The laser described in this section is based on a ring resonator and has lateral emission[2]. This ring laser resonator is based on a trapezoid shaped slab waveguide and was first explored in a simpler version by S. Kragh and A. Kristensen [10]. The simple trapezoid laser was based on a 4.2 μm thick slab waveguide that operated in multiple transverse and longitudinal modes. The three layer version described in this section (see Figure 6.12), uses the trapezoid resonator shape to demonstrate the possibility of defining single mode slab waveguides in SU-8 with thick cores by doping with Rhodamine 6G. The single mode functionality is deduced from the laser spectra from the devices.

Embedding Rhodamine 6G dye in SU-8 raises the refractive index of the resist slightly. Measurements at a wavelength of 633 nm is graphed in Figure 6.13. This tuning of the refractive index can be used to make waveguides with a small refractive index difference between the core and the cladding. Constructing the planar waveguide with a small difference in refractive index between the core and the cladding, makes it possible to use a thick core and still have single TE-TM

[2]My contribution to this work has consisted in design of the laser resonator structure and analysis of the measurement results.

mode functionality. The mode field distribution in a waveguide with a 4 μm thick doped SU-8 core having a refractive index 0.001 higher than the buffer and cladding is illustrated in Figure 6.14. Since there is an upper limit to how high a concentration of Rhodamine 6G in SU-8 can be used without and loosing the optical efficiency (see Section 2.2), a thick core layer means that a higher gain per length can be achieved since more dye molecules can contribute to the modal gain.

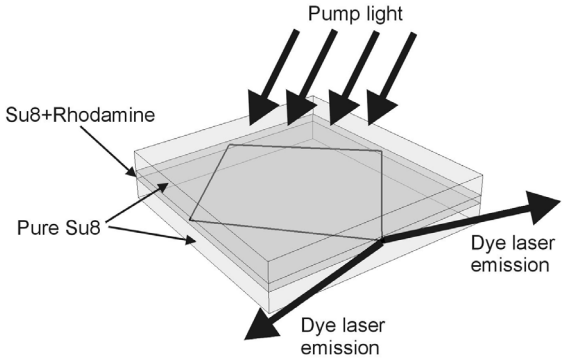

Figure 6.12: Principle of the trapezoidal 3-layer SU-8 laser structure.

Light travelling in the resonator experiences total internal reflection from three sides of the trapezoid and partial reflection from one side where the light is coupled out. Figure 6.15 illustrates some possible beam paths in a trapezoidal resonator. The angles of incidence are $\theta_2 = \theta_3 = 47.3°$, which is well above the critical angle for the SU-8 to air interface (38.9°). The angle of incidence on the output side was $\theta_1 = 38.1°$, giving an angle of the out-coupled light of $\theta_1 = 79°$ which has been verified experimentally [81]. The most immediate interpretation of the

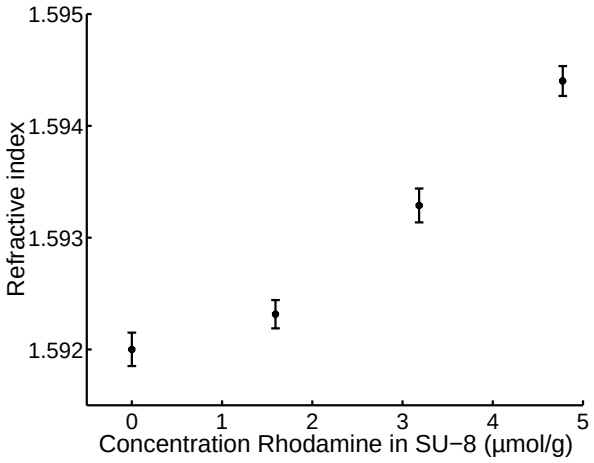

Figure 6.13: The refractive index of SU-8 doped with varying concentrations of Rhodamine 6G. The values were measured at a wavelength of 633 nm.

modes in the trapezoid resonator is the one of closed loops formed by a semi-plane

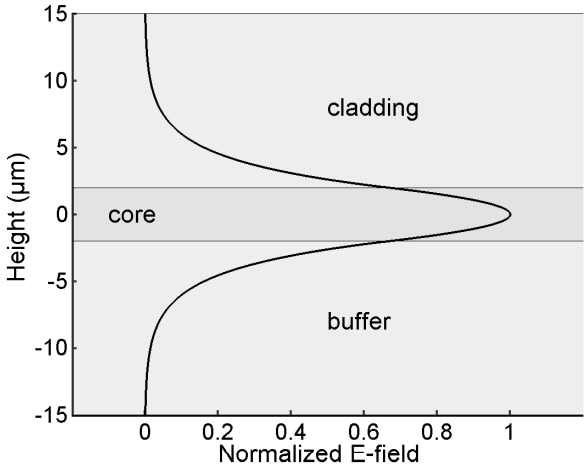

Figure 6.14: The distribution of the electric field for a waveguide with a core refractive index 0.001 higher than the cladding. The core thickness is 4 µm. The field extends into the buffer and cladding, which must be taken into account when manufacturing the device.

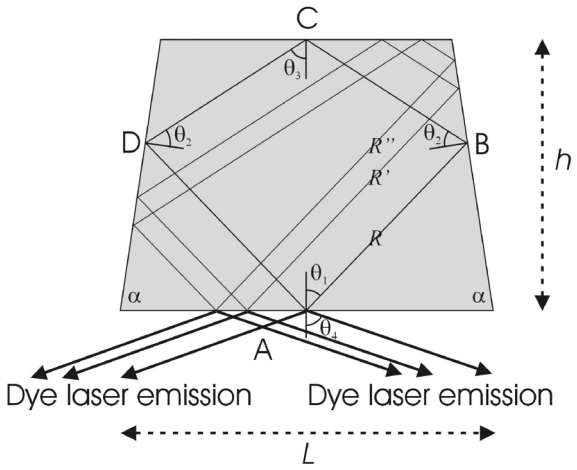

Figure 6.15: Three possible ray paths in the trapezoidal resonator, R, R' and R''. All incidence angles except for θ_1 lies above the critical angle for total internal reflection. Light is coupled out in a sharp angle to the side A.

slab wave travelling around the resonator. However, for square and rectangular resonators, Poon et al., [82], have shown that the mode spectra are more complex and modes with slightly changed incidence angles on the sides also exist. In the case of a laser, it is a fair assumption that the modes with the lowest round-trip loss begin lasing first, and thereby clamps the gain to a degree that eliminates lasing in modes with higher round-trip loss. Especially if the round-trip losses of the different modes differ significantly. The simple closed loop modes have the lowest loss according to Poon et al. and it may be assumed that the lasing modes in the trapezoid belong to the group of closed loops illustrated in Figure 6.15. The trapezoid structure has not been theoretically modelled with respect to the modes with slightly altered incidence angles, but the measurements support the

assumptions above.

It should be noted that while the total internal reflection occurs for both TE and TM polarization, the reflection at the out-coupling surface depends on the polarization. TE modes (with the electric field in the chip-plane direction) experience a power reflectance of 0.2, while TM modes have a power reflectance of 0.54. Therefore it should be expected that TM modes will lase, since they experience the largest reflectivity and therefore the lowest round-trip loss. The expected polarization of the emitted light was confirmed in experiment.

Before fabrication of the device Rhodamine 6G was mixed with diluted SU-8, to a final concentration of 3.2 μmol Rhodamine 6G per gram of solid SU-8.

The three layers were made in three individual spin processes, each followed by a bake step at 90° to evaporate the solvent (see Figure 6.16). In this way, contamination with Rhodamine 6G of the pure SU-8 buffer and cladding layer was minimized. The buffer and cladding layer thicknesses were ∼22 μm, while the core layer was deposited to yield a 4 μm thick layer. The core layer thickness proved difficult to measure since the core material properties resembles the buffer material properties. With a a refractive index difference of 0.001 between the core and the buffer and cladding, the maximum allowed thickness for the core layer is 4.96 μm in order to have single mode operation.

The three layer structure of resist was exposed in a standard UV lithography exposure step, with subsequent development in PGMEA. It is noteworthy, that by performing simultaneous UV lithography on the three SU-8 layers, the wall where the internal laser light impinges on the sides can be as flat as the intrinsic resolution of the resist allows, since the imperfections are localized at the top edge and the bottom edge of the resist (confer for example with the electron microscope images in Section 5.1.1).

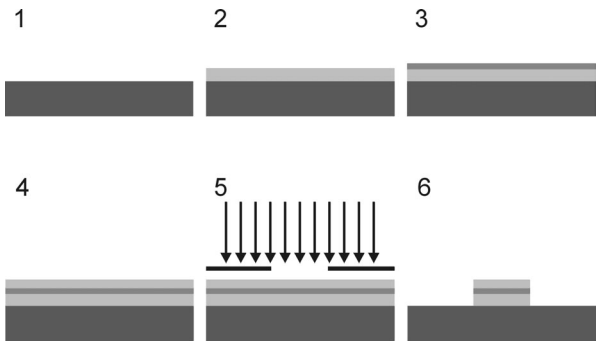

Figure 6.16: Fabrication steps for making the three layer UV defined trapezoid laser. In the steps from 1 to 6, the three layers of SU-8 are spun onto the substrate, and a UV lithographic step is performed.

The lasers were characterized in order to determine if the lasing output bore evidence of operation in a single transverse mode in the slab waveguide. The influence of the size of the laser on the spectrum was investigated, as well as the lifetime of the doped thinfilm under varying conditions.

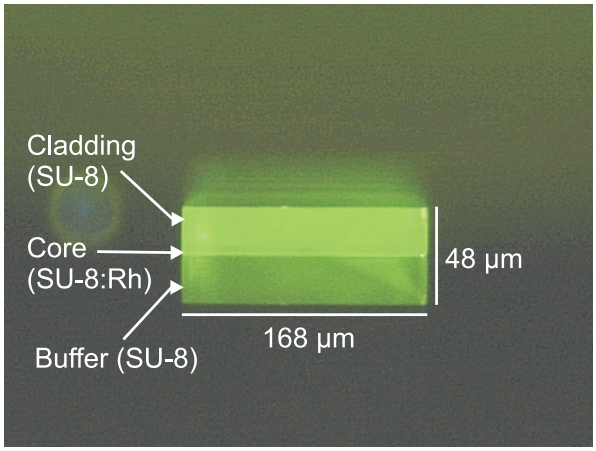

Figure 6.17: Microscope photograph of the side of a three layer trapezoid laser.

Figure 6.18 and Figure 6.19 show the output spectra from two lasers with geometric round-trip lengths of l =292 $\pm$ 5 µm and l =470 $\pm$ 5 µm. The spectra express multi mode lasing and show regular mode spacings of 0.67 $\pm$ 0.08 nm and 0.39 $\pm$ 0.08 nm respectively. According to a basic ring-resonator consideration the following is the case:

$$m\lambda_{\mathrm{m}} = ln_{\mathrm{eff}} \tag{6.2}$$

where $m = 1, 2, 3, ...$ is the mode number, λ_m is the vacuum wavelength of the corresponding mode and n_{eff} is the effective refractive index of the slab waveguide.

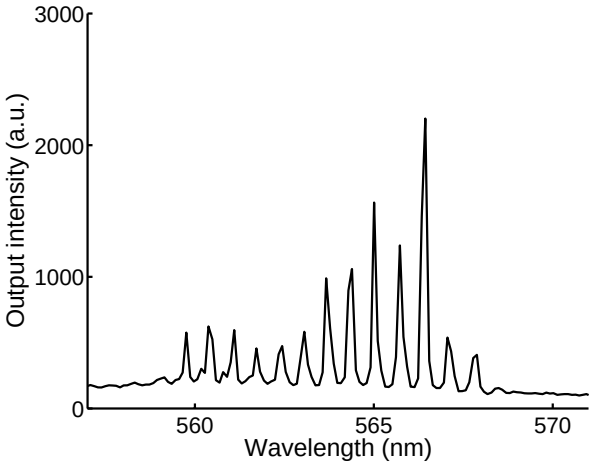

Figure 6.18: Output spectrum from a three layer trapezoid laser with a round-trip length $l = 292$ µm. The mode spacing is 0.67 nm.

The regularity of the spectra in Figures 6.18 and 6.19 is a strong indication that only a single transverse mode is active in the lasing operation of the devices.

Figure 6.20 shows emission spectra from lasers with different round-trip lengths (different sizes). Although the pump curve in the figure reveals a lasing threshold,

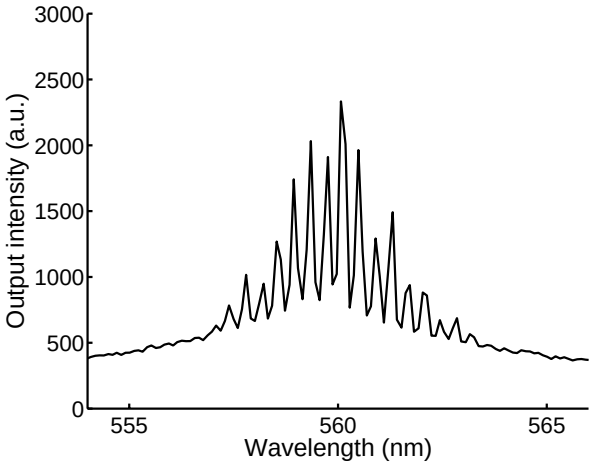

Figure 6.19: Output spectrum from a three layer trapezoid laser with a round-trip length $l = 470\mu$m. The mode spacing is 0.39 nm.

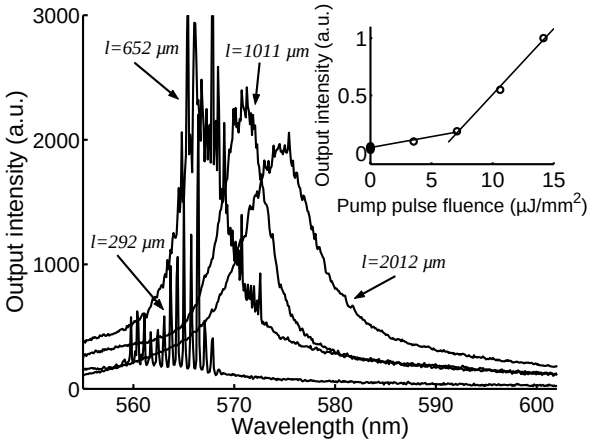

Figure 6.20: Spectra from three layer trapezoid lasers with varying side lengths l. Inset: Example of pump curve with threshold at 7 μJ mm^{-2}.

it is possible that the output is a combination of lasing and amplified spontaneous emission due to the low feedback in the ring resonator (nearly half the energy impinging the out coupling edge is coupled out of the resonator). Either way, the spectra reveals that the spectrum of the stimulated emission depends on the size of the laser structure. The reason for this spectral dependency is found the same place as the spectral dependency of the concentration in Section 6.3. An approach to model the behavior is described in Section 4.2.1 and a more intuitively based description can be found in Section 2.2.

Figures 6.21 and 6.22 show lifetime measurements on thin films of dye doped SU-8 (similar to the doped SU-8 used in the lasers). The fluorescent lifetime is measured for varying pump pulse energy and for varying pump pulse frequency respectively. As would be expected from the considerations in Section 2.2 on photo-bleaching, the lifetime decreases with increasing pump pulse energy. Somewhat more surprisingly, the lifetime also decreases with increasing pump pulse frequency – even

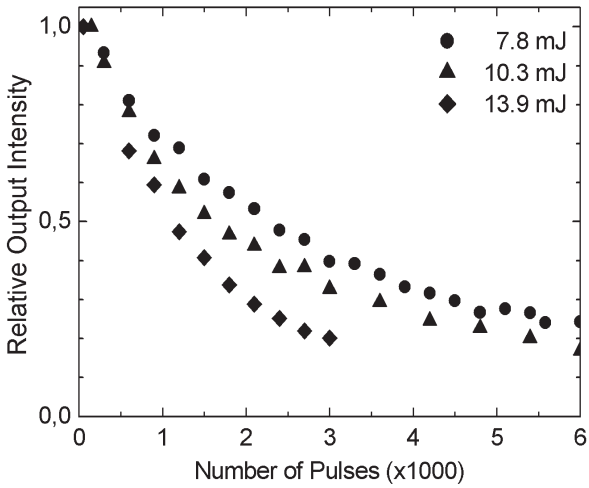

Figure 6.21: Lifetime of a dye doped thin film for three different pump energies. The pump pulse frequency is constant at 10 Hz and the pump spot diameter was 6 mm, with a flat intensity distribution.

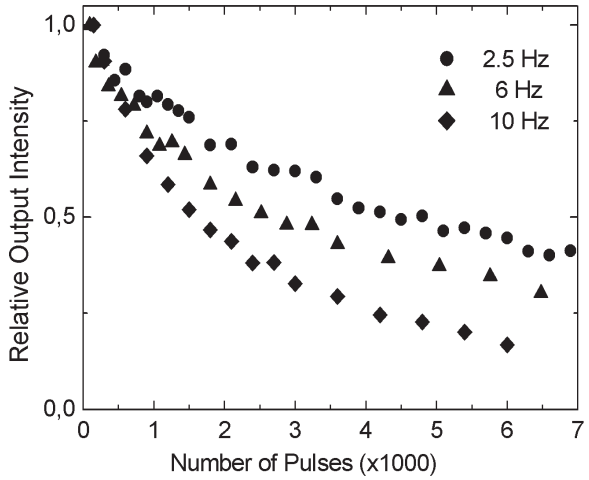

Figure 6.22: Lifetime of a dye doped thin film for three different pump pulse frequencies. The pump energy is constant at 10.1 mJ in the pump pulses impinging a spot with a diameter of 6 mm with a flat intensity distribution.

for the low frequencies used (10 Hz). It can be concluded that the bleaching of the Rhodamine 6G molecules not only depends on how much fluence, peak power or pulse energy the dye receives, but also how far the pulses are spaced in time. The reason is most probably local heating around the dye molecules, which increases with the frequency of the pump pulses.

In conclusion, a single mode waveguide has been fabricated by using three layers of SU-8 with the middle layer doped with Rhodamine 6G. The lasers exhibit multimode lasing with expected mode spacings. The wavelength of the output light depends on the laser size as expected from the considerations on the Stokes shift in Section 2.2. The lifetime depends both on the pump pulse energy and the

frequency of the pump pulses, even though the frequency is below 11 Hz.

6.5 High order Bragg grating DFB lasers

For many applications, such as interference based sensors, it is necessary to use a coherent single mode laser source with a narrow line width. The laser presented in this section has lateral output and can operate in a single mode[3]. The laser resonator pattern is entirely defined in cross-linked undoped SU-8 resist. It consists

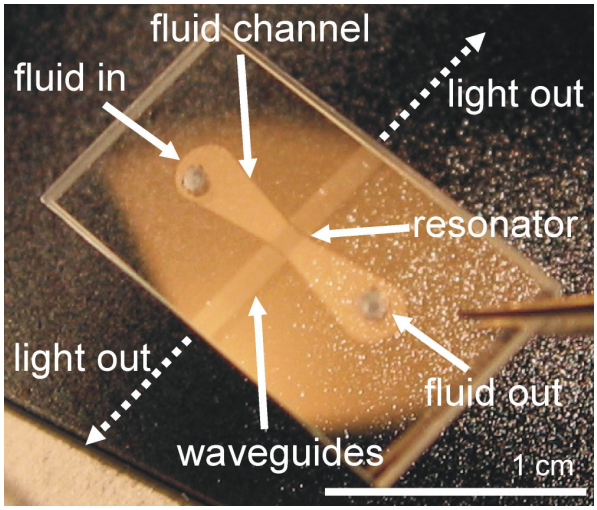

Figure 6.23: Photograph of the microfluidic high order DFB laser with lateral output. Two holes in the glass lid allows dye solution into the microfluidic channel and resontor, while waveguides carries the light to the edge of the chip.

of a high order Bragg grating embedded in a microfluidic channel as illustrated in Figure 6.23. The grating has 22 periods and a phase-shift of $\lambda/4$ in the middle to obtain a single resonance for each Bragg reflection order. During operation, a solution of Rhodamine 6G in ethanol or ethylene glycol is passed through the channel and the laser area is optically pumped with the frequency doubled Nd:YAG laser. A cross sectional view of the overall chip design shown in Figure 6.24.

Since the resonator uses a single Bragg grating with a central phase shift, it falls under the distinction of a DFB laser. However, the Bragg reflection order that is used from the grating is in the 130'ties, and the laser is therefore somewhat different from the traditional meaning of a DFB laser which is generally based on one of the first few reflection orders.

A peculiarity for this laser resonator is the use of a fluid as the core of the waveguide where the resonating light is guided. The core of the planar waveguide is

[3]I have contributed entirely to the work on the SU-8 defined device (i.e. design, fabrication, characterization and data analysis). For the imprinted laser in COC, I have contributed with design, optical characterization and analysis of the measurement results. For the solid state version, I have also been in charge throughout.

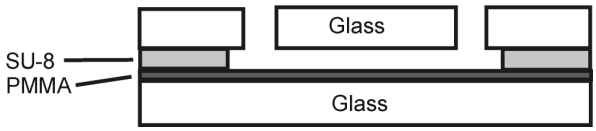

Figure 6.24: Sketch of the chip layer structure.

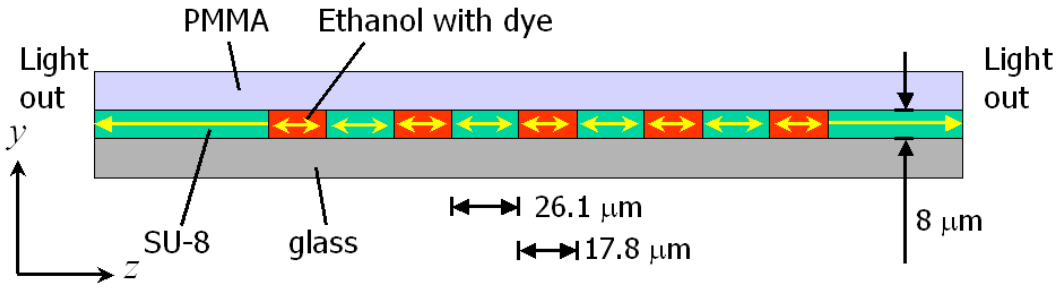

Figure 6.25: Sketch of the high order Bragg grating laser structure. The number of periods (actually 22) has been reduced in the drawing for clarity.

formed both by sections of fluid and by sections of cross-linked SU-8 (see Figure 6.25). However, the fluid parts of the waveguide are not only present in order to obtain gain in the resonator with the laser dye dissolved in the fluid, but also gives rise to a mode-dependent loss that can ensure single mode operation of the laser. The mode-dependent loss occurs since the fluid parts are anti-guiding, i.e. the refractive index of the fluid is lower than the refractive index of the bottom and the top layer of the waveguide. In by far the most cases, a fluid will have a lower refractive index than solids as for example glass or PMMA. High-index fluids are based on oil, and therefore dyes like Rhodamine cannot readily be dissolved in them - or the high index fluids are toxic or will react with Rhodamine 6G.

The beam propagation method that is described in Section 4.1.5 can be used to analyze how the grating structure consisting of the guiding and the anti-guiding segments will influence the loss imposed on the different TE (or TM) modes that propagate in the guiding sections.

Figure 6.26 shows a conceptual drawing of how the light propagates inside the resonator structure. Inside the guiding sections (with a waveguide core of SU-8), a finite number of TE modes are allowed to propagate. The figure considers one mode, n, with an electric field distribution $U_n(y)$. As the mode couples into the anti-guiding section, it deforms and looses energy. When the field again reaches a waveguiding section, the mode, $U_{n,p}(y)$, has to couple into the finite number of discrete modes. The resulting field is $U_m(y)$ inside the next guiding section, for each allowed mode, m. Figure 6.27 shows the result of a FDBPM propagation of the six first transverse modes that can exist in the SU-8 waveguiding regions. The modal loss for a channel transition can be found by taking the inner product between the propagated field and the allowed modes in the SU-8 waveguide [75]. The model uses a gain in the liquid region in order to illustrate the functionality

of the waveguide during pumping of the dye in the laser. It is apparent from the figures, that energy is lost in the antiguiding regions, especially as the mode number increases. Table 6.1 lists the calculated losses for traversing an anti-guiding section for the first six TE modes.

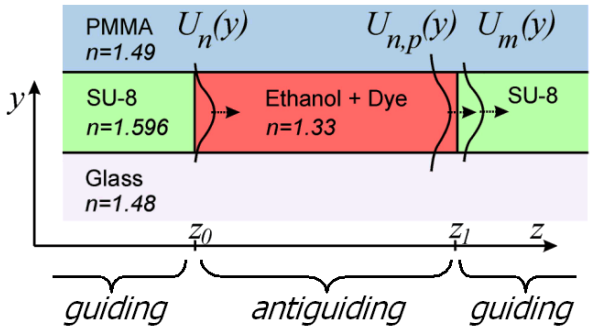

Figure 6.26: Illustration of a period in the high order Bragg grating. The structure is waveguiding where the core is SU-8 and anti-guiding where the core is ethanol.

Mode	0	1	2	3	4	5
Loss	0.006	0.025	0.055	0.093	0.138	0.186

Table 6.1: Calculated mode dependent power loss for the first 6 modes in the SU-8 polymer slab waveguide. The rise in loss is due to lack of confinement in the anti-guiding fluid segments of the resonator.

Figure 6.28 shows a calculation of the round-trip loss for the resonator, based on the transmission matrix approach in combination with the losses calculated via the FDBPM propagation shown above (see also [75]). The strength of the modes vary considerably from Bragg reflectio order to Bragg reflection order, due to the difference in phase evolution in the guiding and the antiguiding sections. This causes an effective three- or four-fold increase in mode distance, compared to the nominal mode distance of 2.5 nm. The increased mode distance makes it possible for the laser to operate in a single mode. The inset in the figure shows a zoom of the round-trip loss calculation for the fundamental TE mode, $m = 0$, and the first order TE mode, $m = 1$. The difference in round-trip loss for the different TE modes make it possible for the laser to operate in a single TE mode.

In fabrication, the laser structure, microfluidic channel and waveguides were defined in an 8 µm thick SU-8 layer on top of a Borofloat glass substrate via UV lithography (see Figure 6.29). Another Borofloat glass substrate was bonded to the SU-8 film using a 4 µm layer of PMMA [30]. The chips were cut from the wafer sandwich with a diamond saw and inlet and outlet holes to the microfluidic channel were diamond drilled. Electron microscope images of the lithographic result can be seen in Figure 5.3.

The laser structure has also been realized via imprint lithography in COC. This demonstrates the possibility of fabricating the laser structure by imprinting, even though it contains both large structures (the microfluidic channel) with an extension of ∼1 cm and small structures with extensions of ∼20 µm (the laser grating).

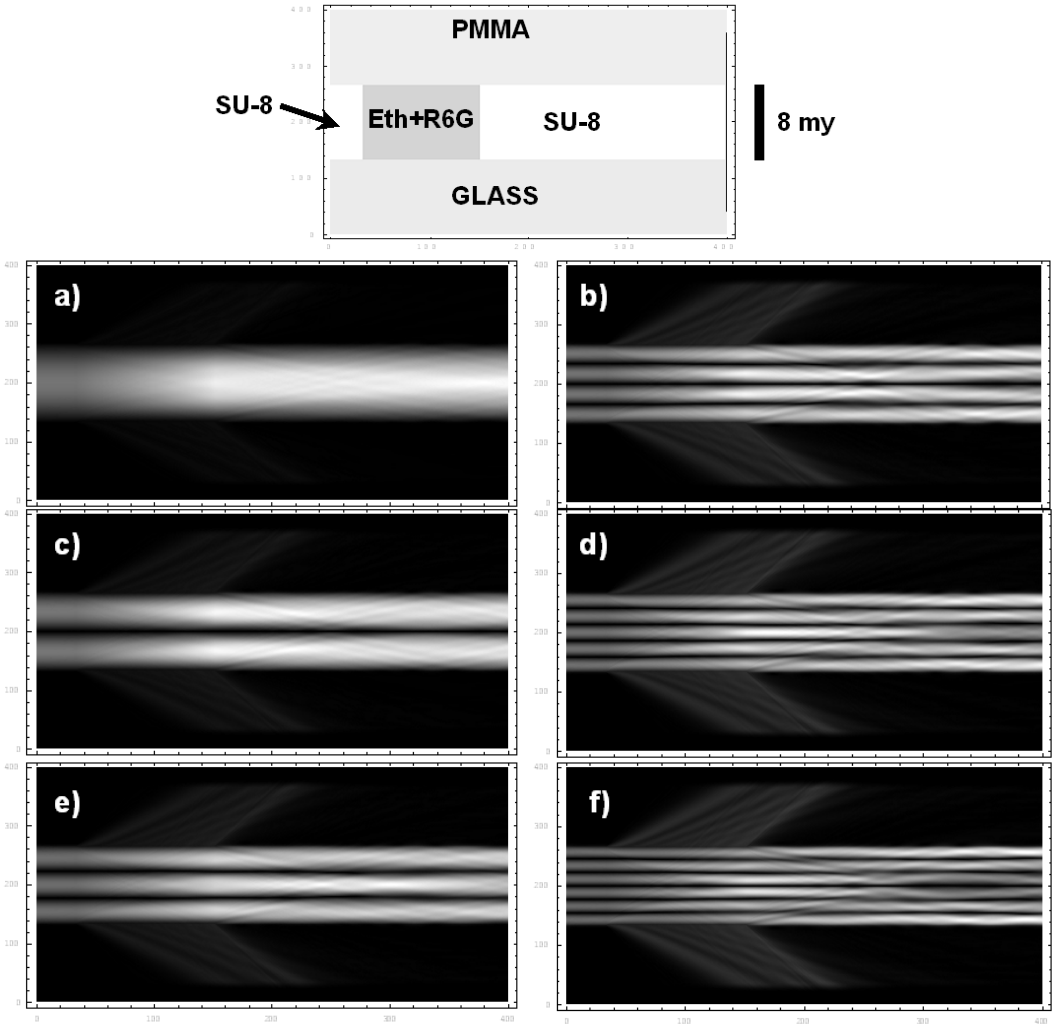

Figure 6.27: FDBPM used to model the propagation through an anti-guiding section of the six first allowed modes in the guiding section. The uppermost picture shows the refractive index structure used in the propagation. The TE mode is 0 to 5 for the sub-figures a) to f). The intensity on the pictures corresponds to the squared norm of the electric field.

It also demonstrates a laser device fabricated entirely in COC (except for the substrates).

The stamp for the imprint was made in a silicon wafer via dry plasma etch (Deep Reactive Ion Etch, Bosch process [83]). The rough surface (50 nm peak to peak) from the dry etch process was smoothed by a thermal oxidation step followed by a wet etch in hydrofluoric acid that removed the oxide film. This left a surface with a peak to peak roughness of less than 15 nm. Details of this process can be found in [76]. The silicon stamp was coated with a teflon like film in order to reduce stiction between the stamp and the polymer during imprint.

For the imprint a silicon substrate with a 3 μm thermal oxide was coated with a 10 μm thick COC layer via a spin-coating process using COC dissolved in toluene. The surface roughness resulting from this spin process was rather high (up to 30%

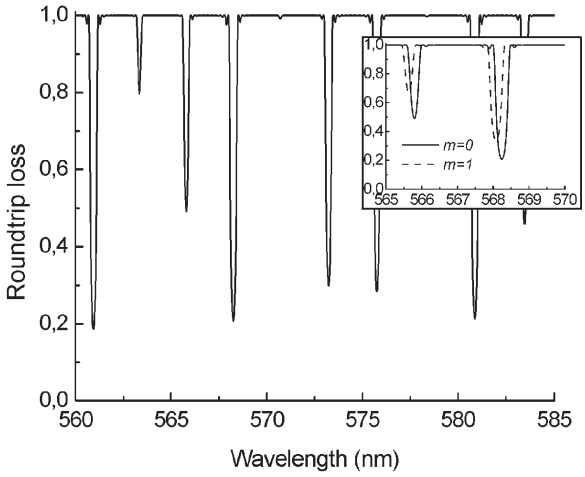

Figure 6.28: The theoretical round-trip loss as function of wavelength, for the fundamental transverse mode. Inset: The round-trip loss for the fundamental ($m = 0$) transverse mode and the next ($m = 1$) transverse mode.

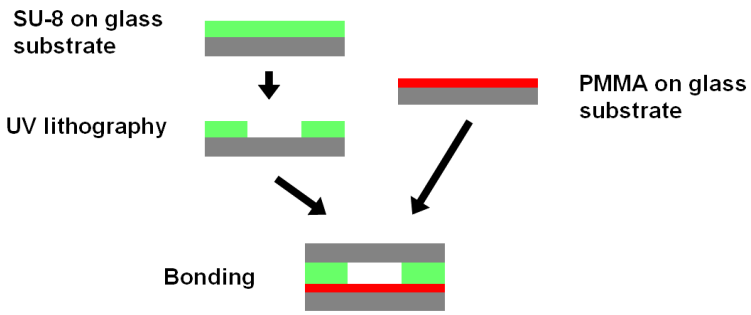

Figure 6.29: Fabrication steps for the UV defined microfluidic DFB laser.

of the film thickness) due to the rapid evaporation of toluene, but the surface was planarized in the imprint process (planarity of COC in toluene after spin-coating and after planarization has been investigated by D. M. Johansen [38]). The stamp was imprinted in the polymer at a temperature of 170°C with a force of 2 kN (on the 4 inch substrates) for 5 min. The force was released after cooling to 70°C. An example of the imprint result is shown in Figure 6.30. Electron microscope images of the imprint result can be seen in Figures 5.21 and 5.22.

To bond a lid to the imprinted structure a 300 nm COC film was spin-coated onto a Borofloat glass wafer. This thin film (compared to the PMMA layer of 4 µm in the SU-8 defined device) was chosen to avoid guiding of light in the bonding polymer since this has the same refractive index as the structure layer (unlike the SU-8 device). The bonding was performed at 90°C with the same force as the imprint step, but this time only 10°C above the glass transition temperature. As with the other microfluidic devices, holes were drilled to the microfluidic channel with a diamond drill. Microscope photographs of the bonding result can be seen in Figure 6.30.

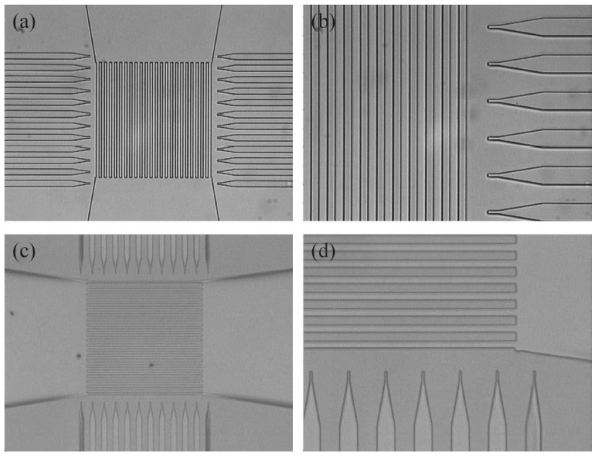

Figure 6.30: Microscope photographs of high order Bragg grating dye laser in COC (Topas). (a) and (b); imprinted structure without lid. (c) and (d) imprinted structure with bonded lid. The laser grating structure is 1 mm by 1 mm.

During characterization of the SU-8 defined chip, a solution of 20 mmol/L Rhodamine 6G in ethanol or ethylene glycol was pumped through the microfluidic channel with a flow rate of 10 µL/hr. This exchanged the dye solution in the resonator area about every 1 second, which was by far enough to eliminate problems with photo-bleaching. The quantum efficiency of the dye seemed to be slightly better in ethylene glycol than in ethanol, however there are no conclusive data to support this.

The pump beam impinged the SU-8 defined chip at normal incidence. It was necessary to avoid pumping the microfluidic channel outside the laser area, as this led to ASE light contaminating the laser spectrum. This was avoided by using an aluminum film to cover the microfluidic channel where the light was not supposed to reach. The measurement setup is shown in Figure 6.31 (without the aluminum shield).

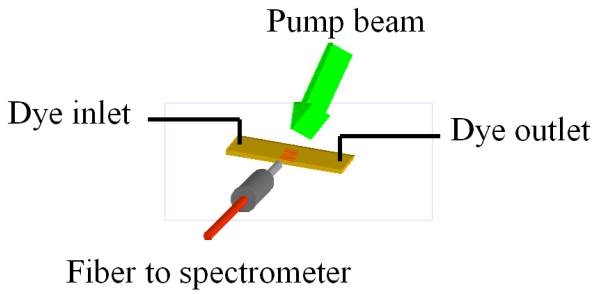

Figure 6.31: Principle of measurement on the fluidic laser chip. (Aluminum shielding not shown).

Figure 6.32 shows a spectrum and a pump curve for a SU-8 defined laser device. The laser was able to operate in a single mode due to the differential transverse mode loss and the effectively increased distance between the Bragg order modes caused by the mode strength variation (see Figure 6.28). The dye laser

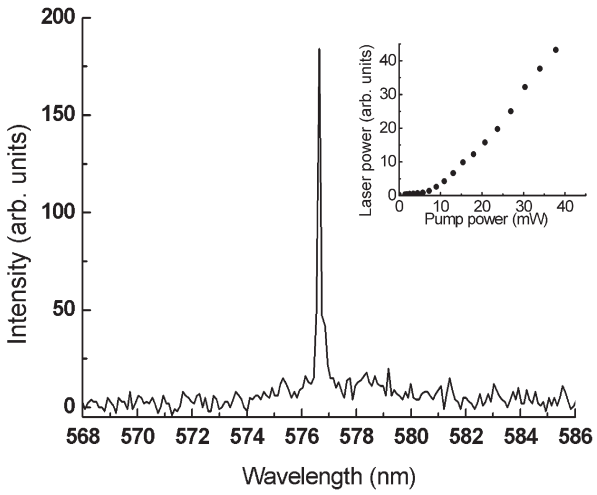

Figure 6.32: Output spectrum and pump curve from a fluid high order Bragg grating DFB laser fabricated with UV lithography in SU-8 .

pulse energy emerging from one side of the laser was measured to 1.2 μJ at a pump pulse energy of 105 μJ impinging the laser area. The lasing threshold was 20 μJ mm^{-2}. Using the method in Section 4.2.1, the lasing threshold was calculated to 1.3 μJ mm^{-2} by finding the 5 ns pump pulse energy necessary to reach a total gain of 1 in the resonator. This is about 15 times less than the observed threshold. Assuming that the method for finding the threshold is correct, the discrepancy may be ascribed to a smaller quantum efficiency than expected of the dye, different cross sections for emission and absorption in the dense dye solution or higher resonator losses than expected.

It must be mentioned that other Bragg reflection orders also began to lase if the pump beam was misaligned. Misalignment could also induce lasing output from higher order transverse modes. The origins of the additional modes were determined by inspection of the mode distances in the spectra. The alignment is not made less critical due to the inherent fringe structure in the pump beam. The light from the laser was picked up with a multi-mode fiber (core diameter: 200 μm) located a couple of centimeters from the waveguides on the chip (see Figure 6.31).

Figure 6.33 shows a spectrum and a pump curve from measurements on the high order Bragg grating laser imprinted in COC. The measurements were performed in the same manner as on the laser defined in SU-8. The spectrum contains much more structure than the spectrum from the SU-8 laser and cannot be termed "single mode". Three factors may contribute to this; 1) the structure quality is higher than for the UV defined laser, 2) the residual layer may allow for more transverse modes to exist and 3) the refractive index of the polymer used is 1.53 and not 1.6 as for SU-8. The high structure quality decreases the losses, thereby lessening the difference in losses between the transverse modes while the increased number of transverse modes makes the laser less prone to operate in only one of them. The lasing threshold was 60 μJ mm^{-2}.

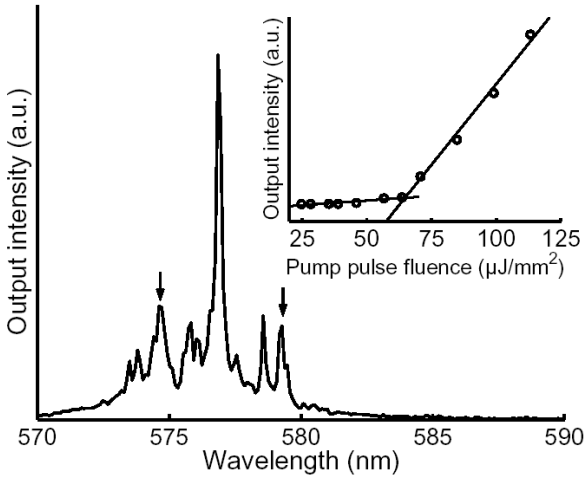

Figure 6.33: Output spectrum and pump curve from a fluid high order Bragg grating DFB laser fabricated with imprint lithography in COC (Topas). The two arrows indicate alternative Bragg reflection modes.

A solid state version using a high order Bragg grating has also been developed. This laser resonator is based on some of the same principles as the high order DFB microfluidic lasers described above. The resonator is made by a high order grating with a (geometric) grating period of 45.2 μm, and a central phase shift of $\lambda/4$. The structure can therefore easily be fabricated with simple UV lithography.

The structure is outlined in Figure 6.34. It consists of waveguiding and anti-guiding segments, with a doped SU-8 core and PMMA respectively. The light travels subsequently in the doped SU-8 and in the PMMA, that also forms the cladding for the doped SU-8. A buffer of pure SU-8 is used to reduce the number of allowed transverse mode in the doped SU-8 core. A few allowed modes can propagate, the exact number depending on the refractive index posed by the doped SU-8, which depends on wavelength due to the anomalous dispersion and is not exactly known.

The beam propagation method that is described in Section 4.1.5 were used to analyze how the grating structure consisting of the guiding and the anti-guiding segments influences the loss imposed on the different TE (or TM) modes that propagate in the guiding sections. Figure 6.35 shows the results of propagating the two lowest transverse modes in the SU-8 waveguiding section, through a period of the grating, assuming a refractive index difference between the doped and the undoped SU-8 of 0.002. The power loss fraction for the fundamental TE mode travelling through 1 period in the grating is estimated from the model to 0.47 and to 0.82 for the next TE mode. The loss is therefore quite high and can be expected to lead to a high lasing threshold. However it also makes it possible to obtain lasing in only one transverse mode due to the large difference in loss between the transverse modes.

The solid state high order Bragg grating laser devices were fabricated on 4 inch silicon wafers. The first 7 μm thick SU-8 buffer layer was deposited in a spin

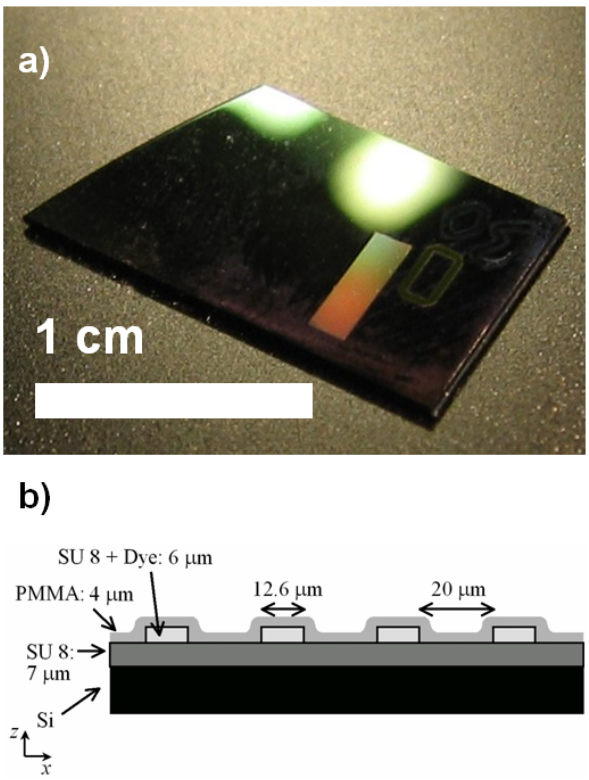

Figure 6.34: a) Photograph of a chip with a single mode high order Bragg grating DFB laser (rectangular area). b) Schematic of a part of the laser in profile.

process with subsequent flood UV illumination and bake in order to cross link the pure SU-8. On top of this pure layer, a 6 μm thick Rhodamine 6G doped SU-8 layer was deposited and subjected to a standard UV lithography step defining the grating structure. The SU-8 was doped with Rhodamine to a concentration of $2.9 \cdot 10^{-6}$ mol per gram solid SU-8. The grating structures were finally covered with a 4 μm thick PMMA layer. The resulting surface contour of the PMMA measured with a surface profilometer is illustrated in Figure 6.36, where also a curve showing the surface contour deconvoluted with respect to the influence of the profilometer needle is graphed.

The solid state devices were characterized with respect to output spectrum and output energy versus pump energy. The devices were not characterized with respect to their lifetime, but it is to be expected that the lifetime is similar to the one measured in Section 6.4, where also doped SU-8 and high pump energy densities are used.

Figure 6.37 shows the spectrum from a laser device together with a pump curve. The lasing threshold is 220 μJ mm^{-2}. The laser is entirely single mode and was purely horizontally polarized. Some lasers containing unwanted defects or with alternative design parameters showed lasing in a few simultaneous modes. Figure 6.38 shows spectra from two lasers with the same design from the same wafer. The spectra are highly similar, which indicates spectral stability with respect to fabrication variations for the design. The specific variations and the

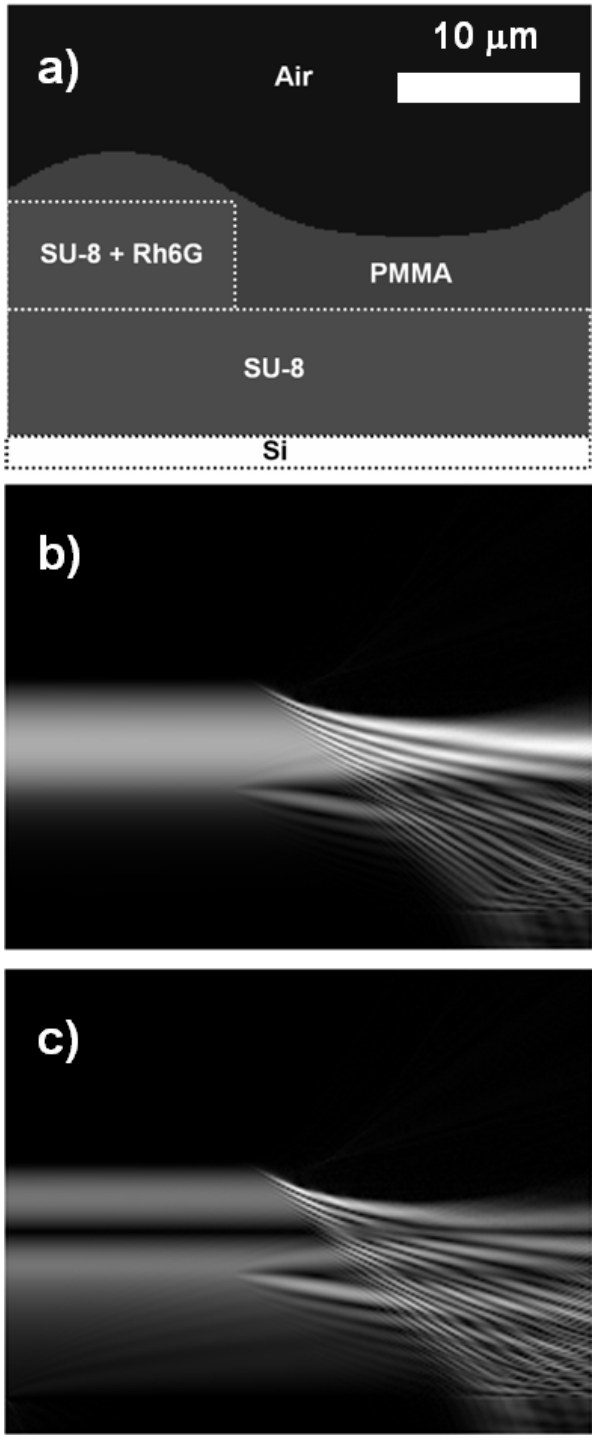

Figure 6.35: a) Grey scale representation of the refractive index matrix used in the beam propagation. The PMMA surface is shaped according to measurements on a real device. b) The squared norm of the electric field of the zeroth transverse TE mode. The field is propagated through one period of the Bragg grating. c) The squared norm of the electric field of the first transverse TE mode propagated through a period of the grating.

variation resistance have not been investigated.

In conclusion, it was possible to realize the high order Bragg grating based DFB

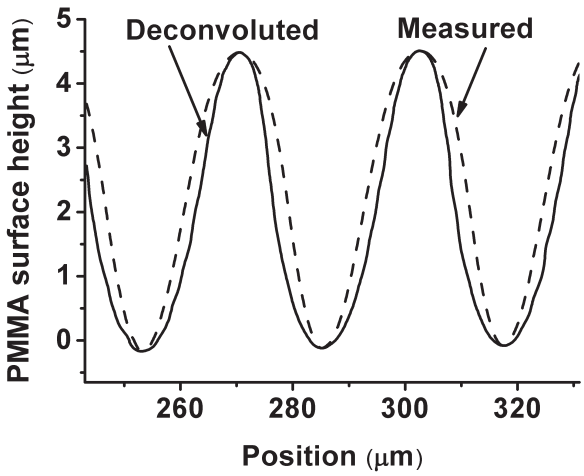

Figure 6.36: PMMA layer surface contour. The dashed curve shows the measurement data, the solid curve shows the measurement data deconvoluted with respect to the profilometer needle radius of curvature (5 μm).

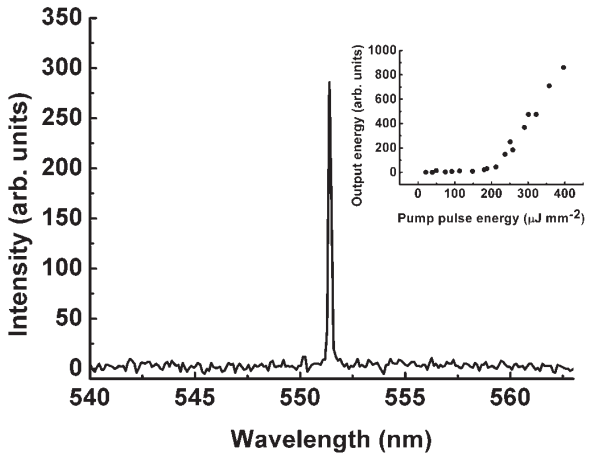

Figure 6.37: Output spectrum from a laser device at a pump energy density of 250 μJ mm^{-2}. The line width reflects the resolution of the spectrometer. Inset: The dye laser energy output as function of pump energy. The laser threshold lies at 220 μJ mm^{-2}.

lasers in several different ways. Single mode operation with the design demands some care in the choice of layer thicknesses, but is otherwise fairly easy to produce. Especially the fluid version of the laser is a good candidate for integration with fluidic channels, since it only requires an additional pattern in the resist already used for the channels.

6.6 First order Bragg grating DFB lasers

While the high order Bragg grating DFB lasers described above emitted light laterally in the chip plane and could operate in a single mode, the operation

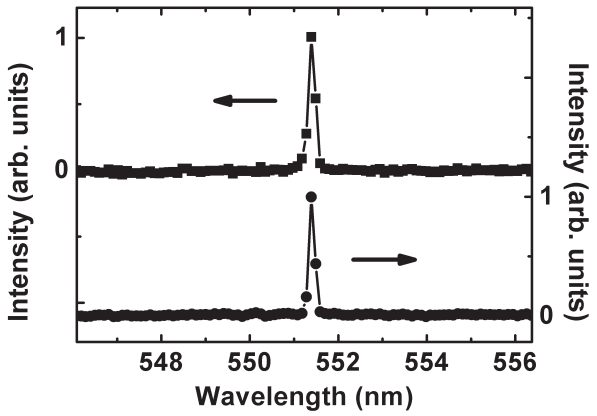

Figure 6.38: Output spectra from two laser devices cut from a common wafer. The emission from the lasers is highly similar, indicating that the design is tolerant with respect to process variations.

wavelength depended somewhat on chance. Therefore lasers with first order Bragg gratings were investigated when the fabrication of these was made possible with the acquisition of a machine for electron beam lithography at the DANCHIP clean-room facility[4]. With first order Bragg gratings the lasing wavelength can be chosen almost entirely at will within the operational region of the gain medium.

As described in Section 5.1.2, the height of SU-8 resist can be varied by using electron beam grey scale lithography. This can be used to fabricate small surface variations in any desired pattern. In the present case, it was used to make a first order Bragg grating with a well defined phase shift of the grating in the middle of the structure.

The laser devices were defined in a 500 nm thick film of dye doped SU-8. The SU-8 film was deposited on a SiO_2 surface, and the film functions as a planar waveguide with a buffer of SiO_2 and a cladding of air. A 0.5 mm by 1 mm area was defined with a periodic surface corrugation having a period of $\sim$200 nm and a 10 nm peak-to-peak amplitude, using grey scale EBL.

Using the expression (4.18) to find the coupling constant of the grating, first the average refractive index and the modulation height of the refractive index n_{mod} in equation (4.17) must be found. By applying the method in Section 4.1.1, n_{eff} and n_{mod} are found to 1.547 and $0.705 \cdot 10^{-3}$ respectively. This gives a coupling constant of $3.6 \cdot 10^3$ m^{-1}. By using the transfer matrix method the theoretical reflection spectrum from half the grating in the structure can be calculated, and this is illustrated in Figure 6.39. It should be kept in mind that determining the exact value of the coupling constant is difficult since the surface corrugation may not be entirely sinusoidal and since the grey scale fabrication method may also induce a refractive index variation in the SU-8 itself, due to the non-uniform

[4]My contribution to the work on the grey scale fabricated device has consisted in design, fabrication, optical characterization and analysis of the measurement results. My contribution to the imprinted PMMA device has consisted in contributions in the design phase and analysis of the measurement data.

exposure dose, and the real reflection may be stronger.

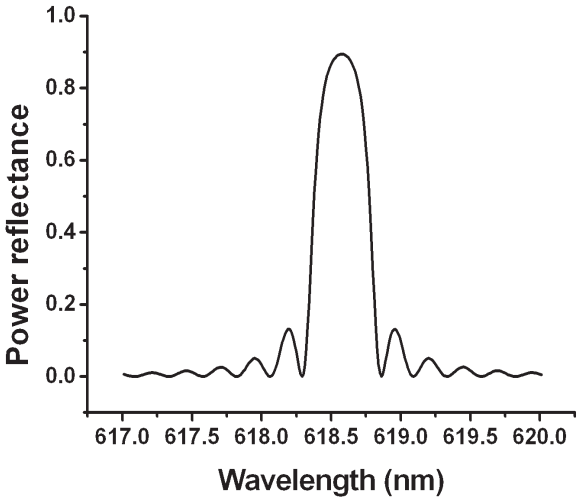

Figure 6.39: Calculated power reflected from half the grating in the grey scale EBL defined laser (length: 500 μm) using the coupling constant $\kappa = 3.6 \cdot 10^3$ m^{-1}.

For a thickness of 500 nm of the core in the planar waveguide, only the fundamental TE mode can propagate. Therefore there are no multimode problems stemming from multiple non-degenerate transverse modes.

The concentration of dye in the polymer was not optimized, although lower lasing thresholds may be possible by lowering the dye concentration, since gain may be reached for lower pump pulse energies under optimized conditions.

The most basic mode of operation of the laser resonator, consists in a semi-plane slab wave travelling in the slab waveguide and being reflected uniformly by the uniform Bragg grating. This interpretation is consistent with the observed laser wavelength and the effective refractive index of the slab waveguide. However, other operation modes may also exist, which will be discussed later in this section on the basis of measurement results.

In fabrication, an area of 0.5 mm by 1 mm were defined via EBL and a surface corrugation was induced by varying the dose in the exposure of the area between 8 and 16 μC/cm^2 for the low and the high part of the grating period. According to the dose curve in Section 5.1.2, this would give rise to a height modulation of 25 %, but due to the dense line pattern, the proximity effect evens out the dose, and the final modulation was only 2 %. The resist was exposed with a beam energy of 100 keV and a beam current of 0.2 nA.

In preparation for fabrication, the SU-8 resist was mixed with thinner (cyclopentanone) to obtain a solution with a solid mass content of 20 %. Rhodamine 6G perchlorate was mixed into the solution with a dye mass percentage of 0.14 % of the solid SU-8 mass content (corresponding to $2.9 \cdot 10^{-6}$ mol per gram solid SU-8). The final solution was spin-coated at 7000 rpm on a silicon wafer already containing a thermally grown silicon dioxide layer of 2.5 μm. After a pre-exposure bake at 90°C for 2 minutes a 500 nm dye doped resist layer remains.

After exposure, the wafer was post-exposure baked on a hot plate at 90°C for 2 minutes with rapid heating and cooling and developed in PGMEA for 30 seconds with a spray bottle. After rinsing in IPA, the wafer was left to dry.

Four lasers with different grating pitch, were each characterized with respect to their output spectrum and their output as function of pump pulse energy. Also the lifetime of the lasers was investigated.

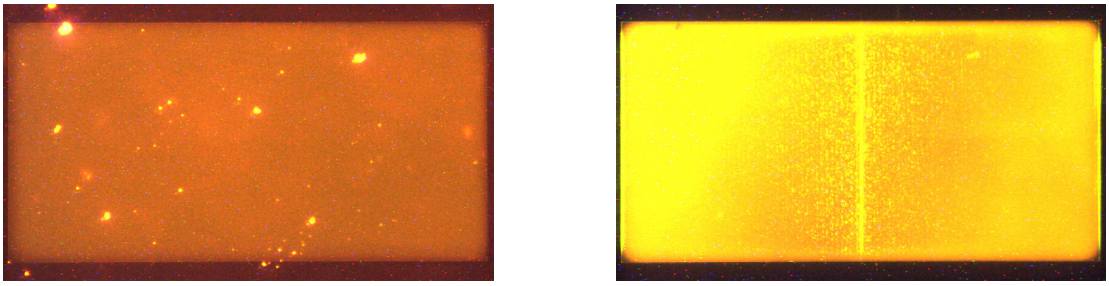

Figure 6.40: Microscope photographs of first order Bragg grating DFB laser. Left: White light photograph (the bright dots are caused by dust). Right: Photograph of the device during operation. The green pump light is filtered away in the microscope. Increased scattering is observed at the grating phase shift in the middle of the structure. The device in the photograph is 0.5 mm by 1 mm in size.

Figure 6.40 shows a microscope photograph of a laser device under white light and during optical pumping with the Nd:YAG laser. There is an obvious increased scattering visible from the grating phase shift in the middle during laser operation, which is not visible under normal lighting.

Figure 6.41 show measurement data for four lasers with Bragg grating pitches of 187 nm, 190 nm, 200 nm and 205 nm. The lasers operate in single mode. Table 6.2 lists the resulting lasing wavelengths and the lasing thresholds. In addition, the table lists the effective refractive index calculated from the grating pitches and the lasing wavelengths via $n_{\text{eff}} = \lambda/2\Lambda$, where λ is the lasing wavelength and Λ is the grating pitch. The calculation assumes that the lasing wavelength corresponds to the Bragg reflection wavelength. The thresholds differ due to the difference in pump energy required to obtain gain at different wavelengths.

Laser	a	b	c	d
Pitch (nm)	187	190	200	205
λ (nm)	579.2	587.6	615.9	630.0
n_{eff}	1.5486	1.5462	1.5398	1.5365
P_{thr} (μJ/mm^2)	1.6	0.75	0.53	0.59

Table 6.2: Parameters for the four laser devices, named a-d: The pitch of the Bragg grating, the observed lasing wavelength, λ, the measured effective refractive index, n_{eff} of the slab waveguide, and the measured threshold for lasing, P_{thr}.

Figure 6.42 shows the calculated refractive index as function of wavelength on a graph. The effective index seems to vary monotonously with wavelength, corresponding to an effective dispersion of $-2.4 \cdot 10^{-4}$ nm^{-1}. The dispersion is caused

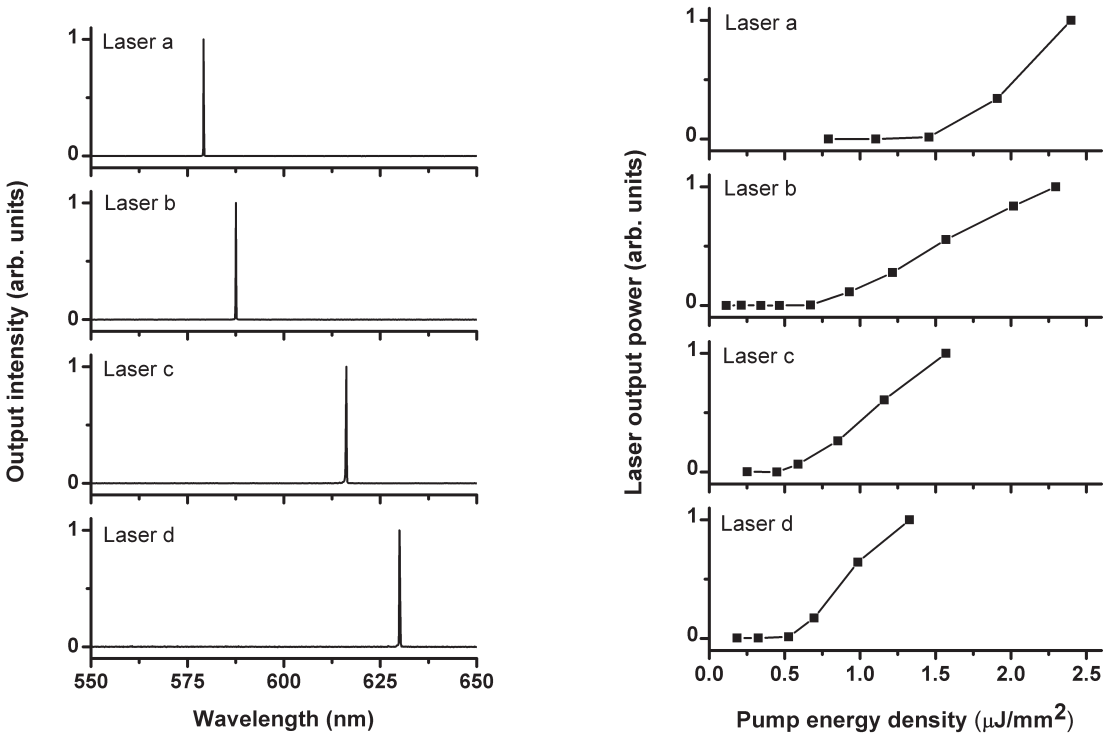

Figure 6.41: Measurement data for four different grey scale defined EBL lasers. Left: Output spectra for pump energy densities of approximately 4 μJ mm^{-2}. The linewidths reflect the resolution of the spectrometer. Right: Pump curves for the lasers.

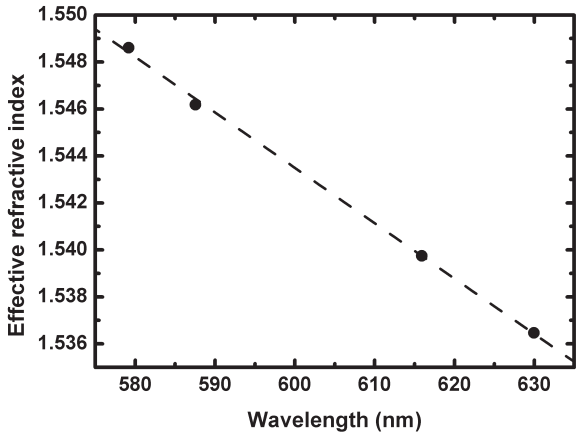

Figure 6.42: The effective index for the four lasers calculated from their lasing wavelength and the grating pitch. The effective index decreases with increasing wavelength with a slope of $-2.4 \cdot 10^{-4}$ nm^{-1}.

by a combination of the dispersions of the materials (including the dye) and the dispersion caused by the waveguide geometry. From the theory of waveguides (see Section 4.1.1) the values expected are a refractive index of 1.54 and a dispersion of $-1.2 \cdot 10^{-4}$nm^{-1} caused by the waveguide geometry. The larger dispersion observed from the slope on the graph is mainly caused by the internal dispersion in the SU-8 ($-1 \cdot 10^{-4}$nm^{-1} at 600 nm (data supplied by [27]) but also the silicon

dioxide ($-3 \cdot 10^{-5}\text{nm}^{-1}$ at 600 nm [84]).

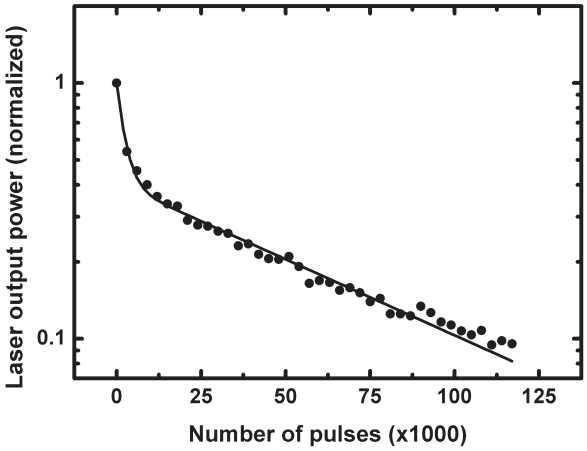

Figure 6.43: The output power from laser device c as function of the number of pump pulses. The pump energy density was 2.2 μJ mm^{-2} at 10 Hz. There is a fast initial decay, which steadies after a while. This pattern was seen for all devices.

Figure 6.43 shows a graph of the output power as function of the number of pump pulses for a laser device. A double exponential function fits the measurement points reasonably well. With P being the dye laser power output, N the received number of pulses, A_1 and A_2 the individual amplitudes of the exponential contributions and γ_1 and γ_2 the inverse decay constants, then

$$P = A_1 e^{-N/\gamma_1} + A_2 e^{-N/\gamma_2} \tag{6.3}$$

with $A_1 = 0.6$, $A_2 = 0.4$, $\gamma_1 = 2500$, $\gamma_2 = 73000$. The behavior of an initial fast decay followed by a slow decay was observed in several devices, with similar decay constants, and did not arise from pump laser fluctuations or from changes in the output pattern of the dye lasers. It can be speculated that the fast initial decay is caused by a factor relating to the doped SU-8 that is "used up" initially, while the slow decay is due to standard photo-bleaching. The factor may be oxygen dissolved in the polymer matrix or other chemical circumstances such as caused by incomplete polymerization due to the low post-exposure bake temperature and time (90°C for 2 minutes).

Figure 6.44 shows an enhanced photograph of the pattern of the laser light on a screen. The screen was placed 10 mm from the laser output, normal to the laser direction. The pattern on the screen suggests the presence of an additional mode in the resonator apart from the expected mode. The expected mode would only give a single vertical stripe on the screen - the output forms a stripe due to the confinement of the light to the waveguide in the vertical direction. However, two more stripes appear on the screen with equal distances to the central stripe. A possible explanation for this could be the presence of a mode supported by four-fold or six-fold total internal reflection inside the rectangular slab waveguide (illustrated in Figure 6.45). The following speculation considers the six-fold reflection mode. The grating couples out the light according the the coupling formula (6.4)(from [58] page 350)

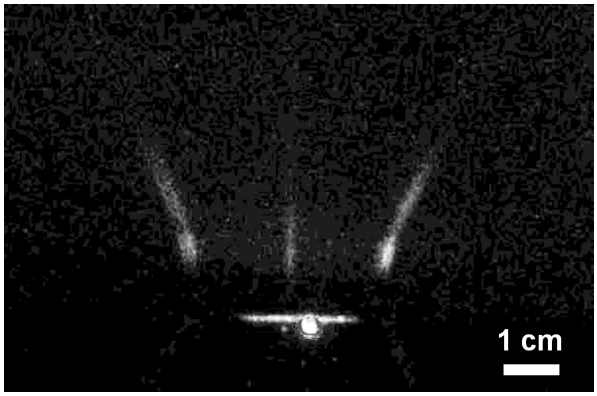

Figure 6.44: A photograph of the laser light impinging a white screen 10 mm away from the laser output. The lower bright spot is the laser itself, the horizontal line just above the laser is light scattered from the edge of the laser chip. The middle vertical stripe is the normally expected output from the laser, while the two angled stripes may be from a parasitic mode.

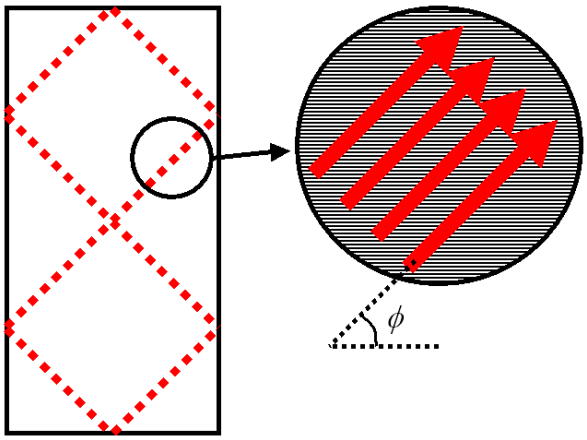

Figure 6.45: Six-fold reflection mode in slab waveguide with grating. The propagation direction of the light in the mode will form an angle of 45° to the grating groves.

$$\Lambda(\sin\Theta_{\mathrm{i}} + \sin\Theta_{\mathrm{m}}) = m\lambda_{\mathrm{vac}}/n_{\mathrm{eff}} \tag{6.4}$$

where Λ is the grating pitch, Θ_{i} is the incidence angle and Θ_m is the angle of the diffracted light (see Figure 6.46). The diffraction mode order is $m = 0, \pm1, \pm2, ...$ and $\lambda_{\mathrm{vac}}/n_{\mathrm{eff}}$ is the wavelength in the medium. In the waveguide, the light in the six-fold reflection mode, travels with an incidence angle (relative to the direction normal to the waveguide) of $\Theta_{\mathrm{i}} = 90°$. The light travels in an angle of $\phi = 45°$ to the grating direction (see Figure 6.45), lowering the effective grating period to $\Lambda_{\mathrm{eff}} = \Lambda_{\mathrm{grat}}/\sin(\phi)$. Assuming that the wavelength of the six-fold reflection mode is 600 nm, then $\Theta_m = 70°$. This angle is not unreasonable but has not been experimentally investigated, except for the screen photograph in Figure 6.44. Obviously, this kind of parasitic mode could be eliminated, for example by making the width of the waveguide smaller. In case the above interpretation of the screen pattern

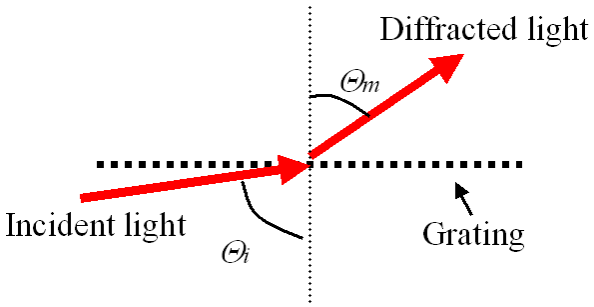

Figure 6.46: Angles for diffraction of light incident on a grating with a grating period of Λ. Only the m'th diffracted mode is pictured.

is correct, the performance of the laser type would increase if the parasitic mode is eliminated. Interestingly, similar DFB lasers fabricated using CNP (Combined Nano- and Photolithography) do not show parasitic modes. The dissimilarity may be due to a lower sidewall quality of the CNP defined devices.

The type of laser resonator that was shown above with EBL in a fast prototype demonstration described above, was also fabricated with imprint lithography. By imprinting the lasers instead of writing them with an electron beam, they can be reproduced cheaply and easily. To demonstrate this, a stamp was fabricated, and the laser structure was imprinted in dye doped PMMA.

The laser resonator is of the same type as the laser resonator for the grey scale EBL defined laser described above.

The stamp for the structure is fabricated with both EBL and UV lithography and reactive ion etching. First step: the first order Bragg grating is defined by EBL on the negative resist TEBN-1 and etched into the silicon surface with reactive ion etching. Second step: the 500 by 1000 µm slab waveguide area is defined by UV lithography and transferred 500 nm into the substrate again by reactive ion etching. The Bragg grating structure is thereby also transferred to the bottom of the 500 nm deep recess.

For the imprint, a substrate with a 680 nm layer of dye doped PMMA (50k) is prepared. The PMMA contained $2 \cdot 10^{-5}$ mol Rhodamine 6G per gram of solid PMMA. An imprint temperature of 220°C was used together with a force of 2 kN on the 4 inch wafers.

The imprint resulted in very good pattern transfer with respect to the Bragg grating (see Figure 5.23 and Figure 5.24 in Section 5.1.4). However, bending of the stamp (see Figure 6.47) caused an uneven thickness distribution of the 500 µm by 1000 µm slab waveguide as seen in Figure 6.48 where the thickness distribution is measured with a surface profilometer. The result of a situation where the bending of the stamp lead to incomplete stamp filling is seen in Figure 6.49.

The imprinted first order Bragg grating DFB lasers were characterized with respect to output spectra and output energy as function of pump energy. Several lifetime measurements were also performed in order to confirm the long lifetime

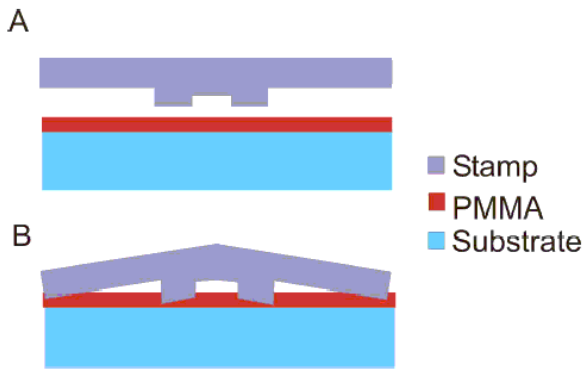

Figure 6.47: Sketch of problem during imprint of mm-sized structures. A: Before imprint the stamp is flat. B: The stamp bends during imprint which results in incomplete stamp filling or film thickness variation along the structure.

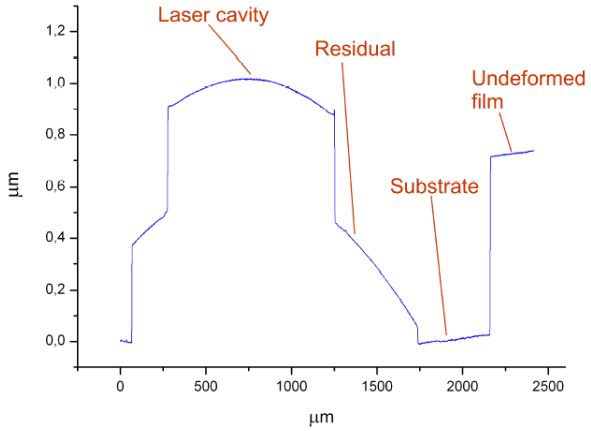

Figure 6.48: Height profile of imprinted structure. The residual film is removed from the part termed "Substrate".

observed for these lasers.

Figure 6.50 shows the measured spectra from four different lasers. The figure also shows the pump curves. The output spectra show a high quality of the output light, however, the line-width is broader than for the EBL defined SU-8 devices – approximately the double of the spectrometer response linewidth, why the FWHM linewidth should be ∼0.15 nm. In addition there seems to be more spurious modes and there are signs of fluorescence, probably from the residual layer. The increased line-widths are most probably a consequence of the grating-chirp induced by the slab waveguide. The thresholds were larger than for the EBL defined SU-8 devices, which may follow from the high concentration of Rhodamine 6G (20 µmol/gr) compared to the EBL defined SU-8 devices (2.9 µmol/gr). The reason why a high dye concentration can lead to higher laser thresholds, is found in the increased pump energy density necessary to obtain gain from the dye. In addition the high concentration may have led to formation of dimers, adding to the optical losses. Finally, the chirped grating and the scattering loss caused by the stitching errors in the EBL definition of the silicon stamp may contribute.

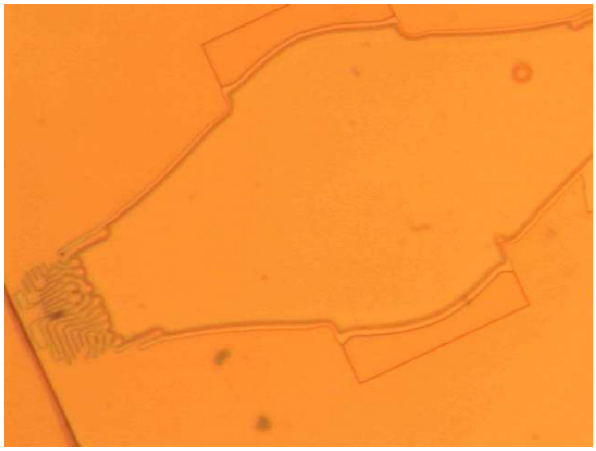

Figure 6.49: Microscope photograph showing the result of stamp bending during imprint, causing incomplete stamp filling. The 0.5 mm wide laser structure is seen above and below the unfilled area.

Figure 6.51 shows a measurement of the output energy as function of pump pulses. The output is halved after about $160 \cdot 10^3$ pulses, which at 10 Hz pump frequency corresponds to four and a half hour of operation. This long lifetime was observed for more than four devices. This was by far the longest lifetime observed for the kinds of solid state lasers that were investigated.

6.7 Conclusion

In this chapter the main laser devices investigated during the work described in this thesis have been described.

The metal mirror laser chip was used to investigate aspects of the stimulated emission dynamics of the Rhodamine 6G laser dye in a microfluidic channel at high concentrations. Thus the work on this device helped to increase understanding of using the laser dye at high concentrations in small structures. The laser type however, is not suitable for integration due to the output in the direction normal to the chip plane and the many process steps needed in its fabrication.

The trapezoid laser has lateral emission and this laser type is a step closer to being a candidate for integration in lab-on-a-chip systems. This laser was used to investigate how to form miniaturized optical resonators solely in polymer, without the use of metal or dielectric mirrors. One of the main objectives was to control the number of TE-TM modes contributing to the lasing activity and it was demonstrated that a single mode slab waveguide could be formed by doping the core laser with laser dye (Rhodamine 6G). The influence of laser size on the output wavelength was also looked into and the behavior completed the picture of the dye gain behavior together with the work for the metal mirror laser.

The group of high order Bragg grating based DFB lasers demonstrated that lateral single mode output could be obtained, even with devices fabricated with standard I-line UV lithography. Three lasers was fabricated; a SU-8 defined microfluidic laser, a nanoimprinted microfluidic laser in COC and a solid state version. The exact lasing wavelength was difficult to predict and the spectral mode pattern depended on the alignment of the pump laser.

After access to new equipment made it possible to fabricate first order Bragg grating DFB lasers, this type of laser was investigated. The laser type was made in two solid state versions; by grey scale electron beam lithography and by nanoimprint lithography. This kind of laser showed low thresholds, lateral emission, single mode operation and long lifetimes. Overall, this was by far the easiest lasers to work with.

The most easy laser to use for integration with other thin film polymer components such as microfluidic channels is the microfluidic high order Bragg grating DFB laser. Using this laser on a chip, the out-coupled light can easily be coupled into waveguides defined in the same polymer layer. The first order Bragg grating DFB lasers on the other hand needs to be fabricated in a separate step than the additional polymer structures on a chip since the DFB lasers are fabricated with dye doped polymer. It should still be possible though, to obtain a good coupling from the laser into the other polymer structures.

Another method to fabricate first order Bragg gratings is to use interference lithography [85]. This method is also cheap, but has the disadvantage that it is not easy to induce an exact phase shift in the grating. Therefore it is not possible to obtain full control of the wavelength and mode structure. However, interference lithography may be advantageous as compared to using high order Bragg grat-

ings, since the lasers based on high order Bragg gratings already have somewhat undetermined lasing wavelengths.

One of the advantages of the micro-fabricated laser devices, that has not been shown in the demonstrations above, is the possibility of making multi-color arrays for advanced sensors. Multiple colors can be obtained by either varying the size of the lasers (in the case where the lasers do not have frequency selective components), or by simply varying the grating period in the Bragg grating based laser devices. Since the laser devices do not take up much space, an array can be pumped by a single pump laser spot.

It proved difficult to measure the output energy of the lasers due to several factors. Coupling of light from the laser chip to a measurement device was difficult since the edge of the devices were rough due to sawing the polymer and thus scattered light to an unknown degree. Furthermore the output was quite divergent for many devices and difficult to collect. Finally, the equipment did not allow for pulse energy measurements on pulses with energies smaller than about 0.2 μJ.

All lasers were polarized in a single direction, although no specific effort has been made in the design to obtain this. In the authors experience it is a common phenomena that for resonator structures that are asymmetric around the axis of light propagation, the polarization will settle in one state only.

Finally, no wavelength shifts caused by pump induced temperature changes have been observed. The pump energy delivered to the lasers were less than 100 mW and the glass and silicon chips were lying on a sample holder acting simultaneously as heat sink.

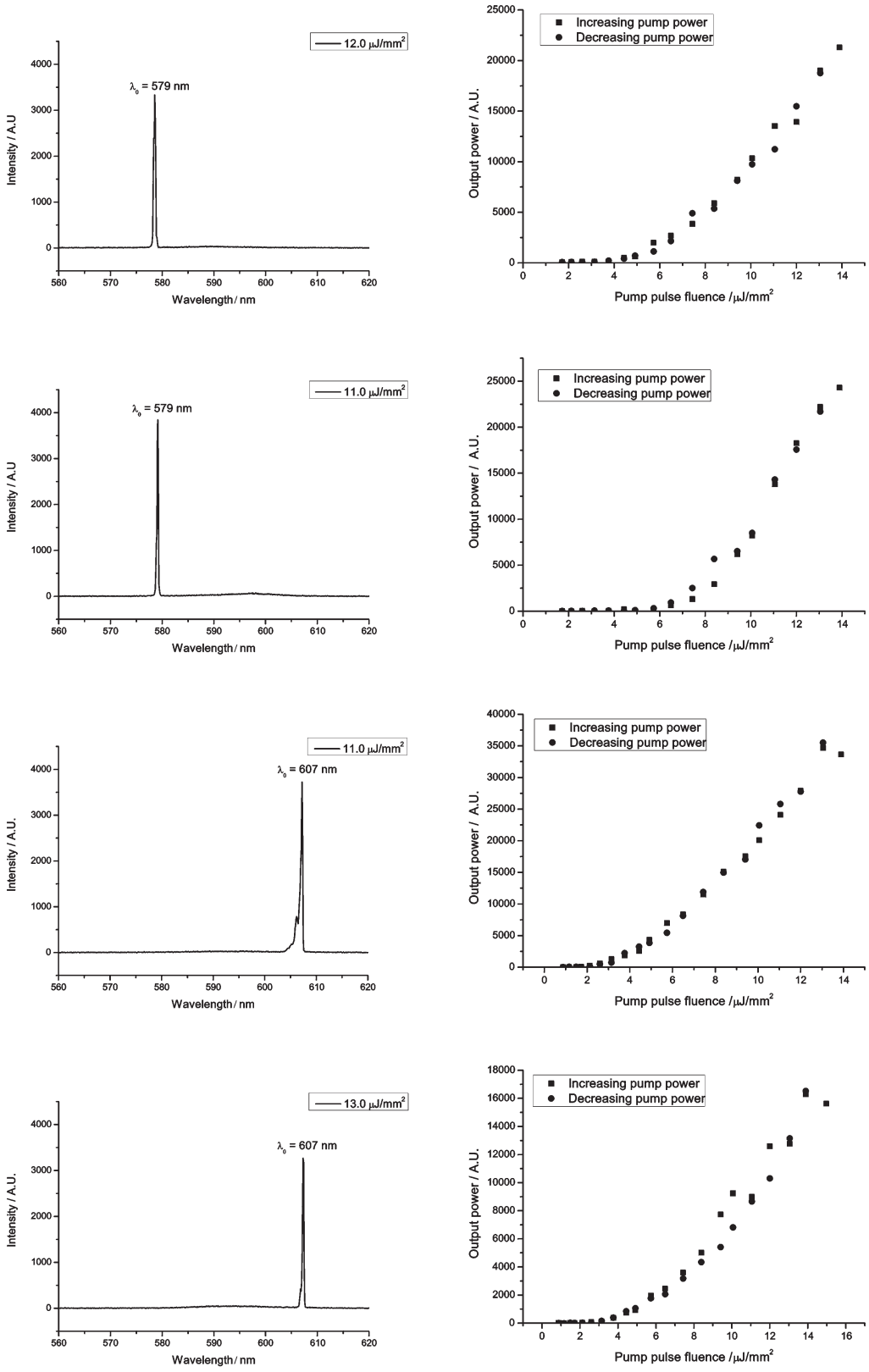

Figure 6.50: Measured data from four different imprinted first order Bragg grating lasers in PMMA. Left: Output spectra. Right: Pump curves.

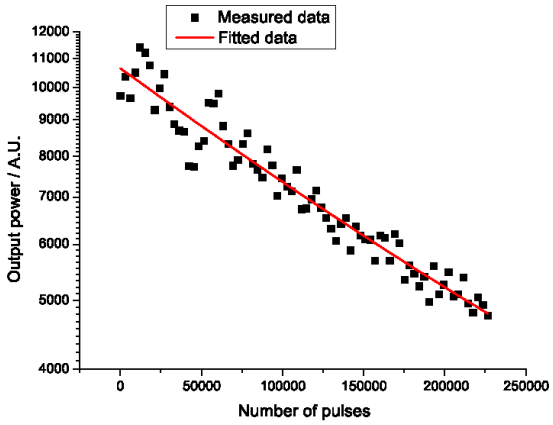

Figure 6.51: Output power as function of the number of pump pulses for the PMMA DFB lasers. The pump pulse energy was 8.4 µJ mm^{-2} and the output is halved after about 160.000 pulses.

Chapter 7

Implementation of polymer dye lasers

This chapter describes three examples of integration of the fluidic high order Bragg grating DFB laser described in Section 6.5. This laser type is particularly easy to integrate, since it only requires an additional pattern in the resist layer - i.e. no additional lithographic steps are necessary in structures that already contain a microfluidic channel system. The first example describes a device where the laser is integrated with other polymer components in addition to photodiodes embedded in the substrate. The second example illustrates how a complete system with several integrated components can be fabricated via a simple imprint step. The last example shows how a polymer dye laser can be hybridized with a miniaturized fluid dispenser that delivers the laser dye to the chip.

The examples explore possible ways to integrate polymer dye lasers with other components. The lasers find their use in the two first examples due to the high directionality of the laser light. In this way they function as converters of more or less randomly orientated light (optical pump) into light with a fixed direction and position (dye laser light). Coherence of the light is not exploited in the present cases. The descriptions of the devices will not be complete in detail, but will give an overview of the device functionality.

7.1 Demonstration of integration

7.1.1 Integration using UV lithography and functionalized substrate

A major advantage of the SU-8 UV lithographic process is that it uses low temperatures and can be used to create optical structures on top of any reasonably flat substrate. The low temperatures and non-aggressive chemicals involved in the SU-8 process allows it to be applied on top of substrates already containing embedded structures such as photodiodes.

In the present example, the fluid high order Bragg grating DFB laser is defined in a SU-8 layer together with waveguides, microfluidic mixer and microfluidic cuvette[1]. Five photodiodes are embedded in the substrate. Their function is to measure the intensity of the light from the laser after it has passed through the cuvette which is filled with a fluid to be tested. Thereby it is possible to measure the absorption of the fluid in the cuvette at the wavelength of the laser light (∼576 nm). The device consists of a microfluidic polymer dye laser delivering light to five polymer waveguides that direct the light to five measuring points along a cuvette (see Fig. 7.1). On the other side of the cuvette, five waveguides pick up the transmitted light and direct it to a photodiode array, enabling spatially or temporally resolved measurements. The electric signal from the photodiodes is used for detection and can be read out from metallic pads on the chip. There is a mixer in front of the microfluidic channel forming the cuvette, making it possible to mix two fluids and measure the absorption of the result. Fluids are supplied to the channels in the chip through holes in the glass lid. The complete micro-system with laser, waveguides, microfluidics and photodiodes has a footprint of 15 mm by 20 mm.

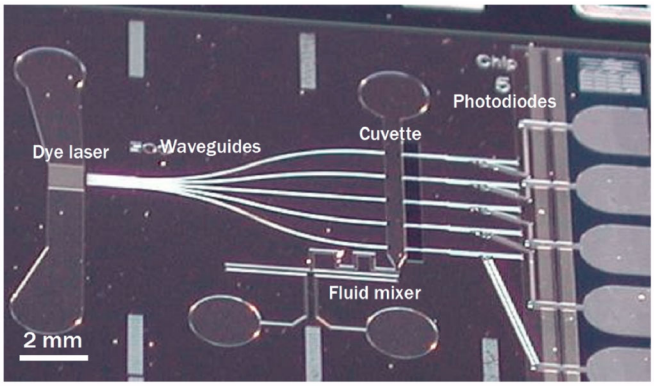

Figure 7.1: Photograph of the lab-on-chip device with integrated microfluidic dye laser, optical waveguides, microfluidic network and photodiodes. The metallic contact pads for the photodiodes are seen on the far right. The chip footprint is 15 mm by 20 mm. The photograph was taken before a lid was bonded to the structures.

Figure 7.1 shows a photograph of the device with the individual components pointed out. The size of the chip is 15 mm by 20 mm. The photograph was taken before a lid was bonded onto the structures. The metal pads on the left were used to read out the photodiode signals. Figure 7.2 shows a drawing of the cross sectional view of the system. The structure consists of a 500 µm silicon substrate, a 3 µm silicon dioxide layer, a 10 µm SU-8 layer, a 5 µm PMMA layer and a 500 µm borofloat glass lid. The SU-8 layer forms the core of a planar waveguide throughout the chip. There is a 70 nm silicon nitride layer between the photodiode silicon surface and the SU-8 (not shown in Figure 7.2). The purpose of this layer is to electrically passivate the front surface of the photodiodes as well as insulate the structures electrically.

[1]My contribution to this work has consisted in a design contribution, a fabrication contribution, optical characterization and analysis of the measurement results.

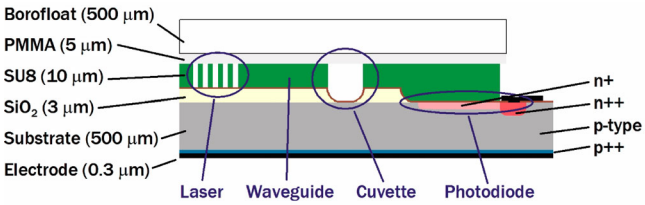

Figure 7.2: Outline of the cross section of the lab-on-chip device. Photodiodes are embedded in the silicon substrate (right), while optical waveguides and the microfluidic network are defined in the 10 μm thick SU-8 film. The channels are sealed off by a borofloat glass lid bonded to the SU-8 by means of a thin PMMA film.

In order to facilitate coupling of light from the SU-8 waveguides into the photodiodes, the silicon dioxide layer has been removed at the photoactive part of the photodiodes (Figure 7.2 right). The light in the waveguides will couple to the photodiode via leaky mode coupling. The underside of the silicon substrate contains a common Al electrode for the photodiodes.

Figure 7.3 shows electron microscope images of different parts of the chip. Rectangular multimode waveguides are formed in the SU-8 by defining 30 μm wide strips of SU-8, see Figure 7.3a). The structure imposes lateral confinement to the slab waveguide modes that travel in the SU-8. The laser light source is shown in Figure 7.3 b). The laser is equivalent to the laser described in Section 6.5, except for a small change of the waveguides that pick up the emitted light. The emission spectrum from the laser in the integrated device had the same characteristics as the corresponding lasers in Section 6.5. The waveguides terminate 25 μm before the cuvette channel and continue on the other side with a similar buffer distance to the cuvette (Figure 7.3 c) [86]. The waveguides direct the light they have picked up on the far side of the cuvette to the 2 mm long active area of the photodiodes, Figure 7.3 d).

Apart from the channel delivering laser dye solution to the laser, the microfluidic system on the chip consists of a mixer that functions by diffusion [87] and a cuvette for the absorption measurement (Figure 7.1 and Figure 7.4). The two mixer inlet channels are 50 μm wide and 8 mm long and yield a fluidic resistance of $22{\cdot}10^{15}$ Pa s/m^3 for water. The mixer meander where the two fluids meet and mix by diffusion is 100 μm wide and 5.7 mm long. The meander yields a fluidic resistance of $6{\cdot}10^{15}$ Pa s/m^3 and the 500 μm wide cuvette has a fluidic resistance of $1{\cdot}10^{15}$ Pa s/m^3. The mixer requires only small fluid amounts and is designed for flow rates of $\sim$1 μL/hr.

The response of a photodiode to laser pulses is illustrated in Figure 7.5. During measurement, the photodiodes were coupled in parallel with a 1 nF capacitor and a 1 kΩ resistor in order to measure the charge generated with each laser pulse [88]. The clear indication of the lasing threshold at 14 mW (corresponding to a pump energy density on the dye laser of 50 μJ/mm^2) in the graph in Figure 7.5 demonstrates a low influence of scattered 532 nm pump light on the photodiode signal. To obtain this discrimination the chip had to be shielded to the pumping light (except for the laser area). The inset of the figure shows the diode response

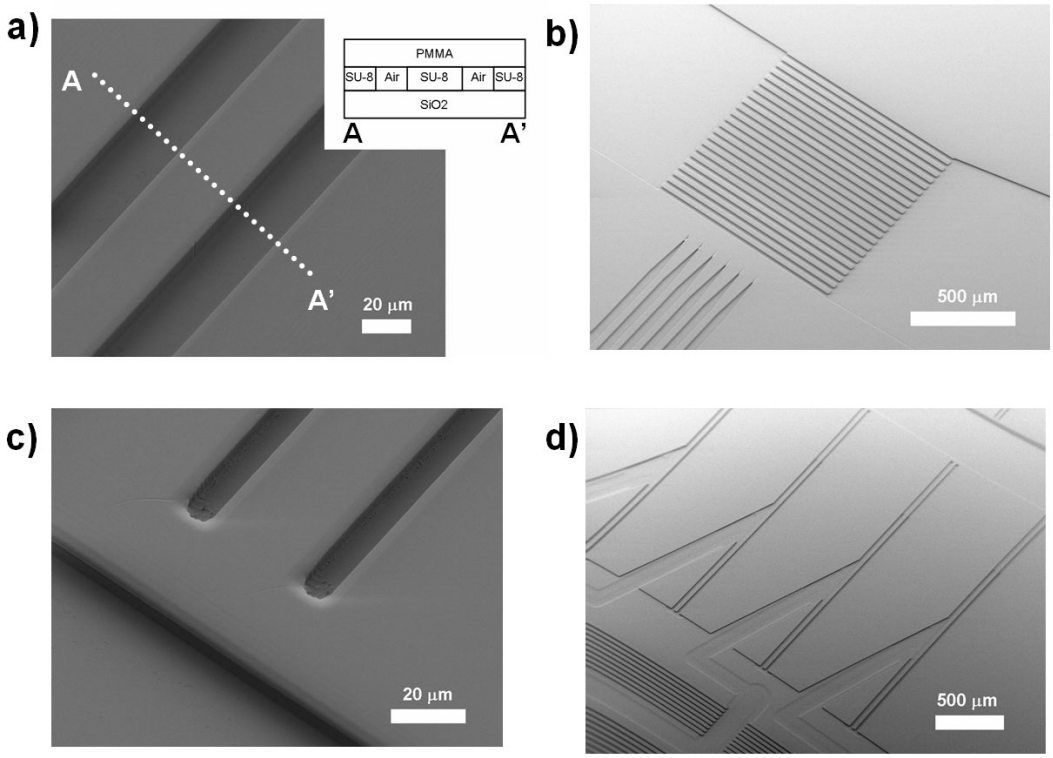

Figure 7.3: a) Electron microscope image closeup of a section of a waveguide. The light is guided in the central strip of SU-8. Inset: drawing of waveguide structure (not to scale). b) Electron microscope image of the microfluidic dye laser (center) and the beginning of the waveguides (lower left). The laser structure is situated in a 1 mm wide channel carrying the liquid gain media. c) Electron microscope image of the termination of a waveguide at the side of the cuvette, forming a dike towards the cuvette. d) Electron microscope image of the waveguide to photodiode coupling region. The waveguides picking up the light from the cuvette (upper right) directs the light to the photoactive region making up the last 2 mm under the waveguides which then terminates.

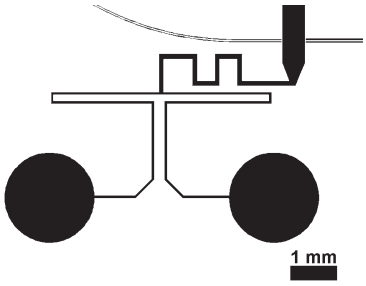

Figure 7.4: Design of the microfluidic mixer. There are two inlet holes connected to the inlet arms that meet at the beginning of the mixing meander. The meander opens up to form the cuvette (top right). The curved double line is the waveguide closest to the beginning of the cuvette.

to a single laser pulse.

In a demonstration of the operation of the integrated components, an absorbance

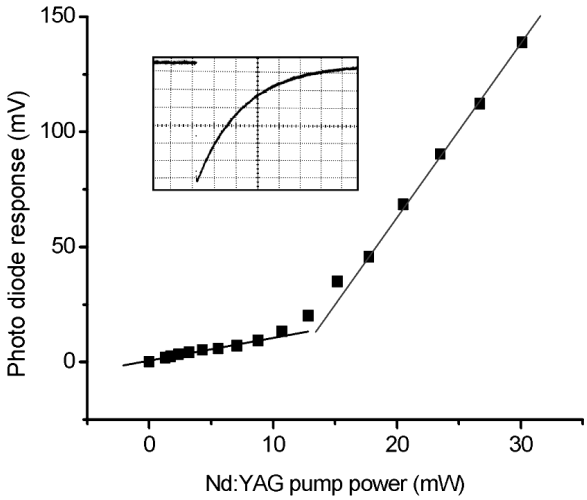

Figure 7.5: Photodiode response as function of optical pump power of the laser pumping the on-chip dye laser. The inset shows the open circuit response from a photodiode to a single pump pulse (vertical 10 mV/div, horizontal 10 ms/div).

measurement on two different concentrations of xylenol orange dye was performed [89]. Xylenol orange was used due to its absorption peak which is located at the dye laser wavelength. The dye can be used to detect ferrous ions in aqueous solution. Before each particular xylenol orange dye solution was injected into the cuvette, a reference measurement with pure water was performed. The xylenol orange solution was diluted in an ammonia buffer (pH=10) with Ca^{2+} ions. The photodiode signal, I, for different xylenol orange dye solutions, was referenced to the photodiode signal, I_0, for pure water in three tests. As expected, a test with pure water and pure ammonia buffer gave essentially the same signal readout on the photodiodes (so $I/I_0 \approx 1$). A xylenol orange dye concentration of 0.06 mM gave $I/I_0 = 0.7$ and a concentration of 0.12 mM gave $I/I_0 = 0.3$. This brief examination shows that the device could operate and measure absorption.

7.1.2 Integration using imprint lithography

The device in the above Section 7.1.1 described how a whole system containing laser, micro-optics and microfluidics, can be made by a single UV lithography step. As demonstrated in Section 5.1.4, imprint lithography can deliver higher resolution and better structure quality than UV lithography. The current example demonstrates that a system of polymer components, including a laser, can be fabricated via imprint lithography in COC[2]. The lid is bonded on to the structure with the same polymer, and the system is thus formed fully in COC, apart from the substrate and the lid, which are made of oxidized silicon and Borofloat glass respectively.

Figure 7.6 shows a photograph of the imprinted device with labels. The device

[2]My contribution to this work has consisted in contributions to the design and analysis of the measurement results.

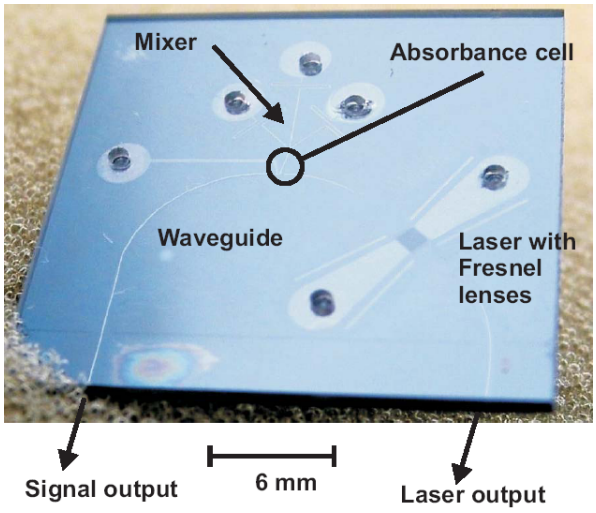

Figure 7.6: Photograph of COC chip with integrated components.

consists of a microfluidic laser that emits light into two waveguides. One of the waveguides direct the light to the edge of the chip for reference, while the other carries the light to an absorption cell. A fluid can be injected into the absorption cell and the transmitted light is picked up by another waveguide. The second waveguide directs the transmitted light to the edge of the chip for measurement. The microfluidic mixer functions by diffusion and has three inputs.

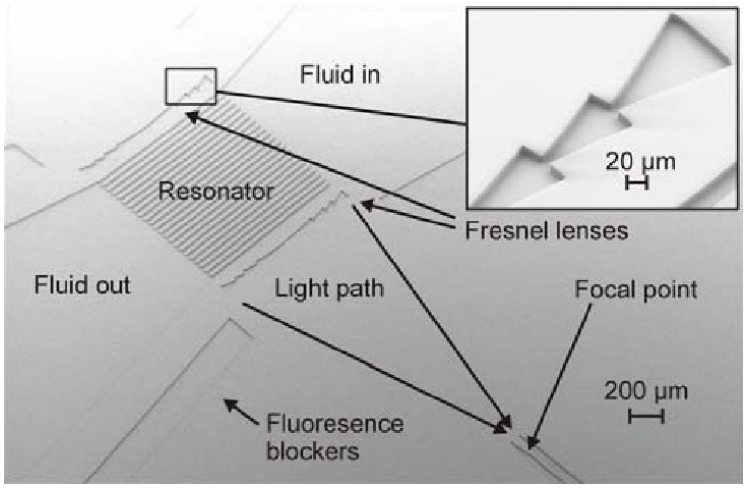

Figure 7.7: Electron microscope image of the microfluidic laser, Fresnel lenses and waveguides imprinted in COC.

Figure 7.7 shows electron microscope images of the laser along with the experimental Fresnel lens, whose job it is to focus the parallel output from the laser into a single waveguide. The lens was designed without any experimental knowledge about the performance of such a lens design in the current application. This important component of the chip may not have functioned as well as planned. The rationale behind using a Fresnel lens design instead of a standard continuous lens

was to minimize the path length the light had to travel through air, since the air section is anti-guiding.

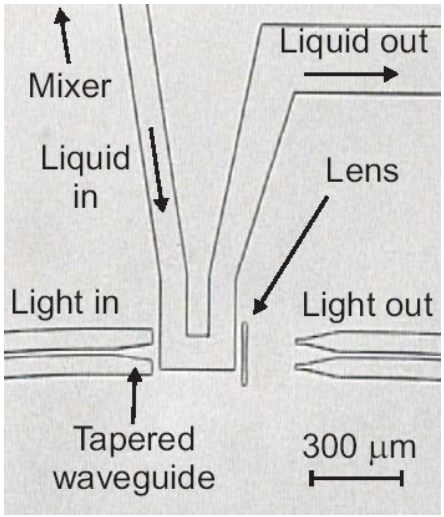

Figure 7.8: Microscope photograph of the two tapered waveguides sending light into the cuvette where an absorbing fluid can be injected. The waveguides are tapered and an air lens is used to maximize the transmission of light from the left waveguide to the right.

Figure 7.8 shows a microscope photograph of the absorbtion cell where mixed fluids interact with the laser light travelling in the optical waveguide. An air lens is used in the design to refocus the light leaving the cuvette on the signal output waveguide. As noted on the figure, the fluid delivered to the cuvette arrives from a diffusion mixer.

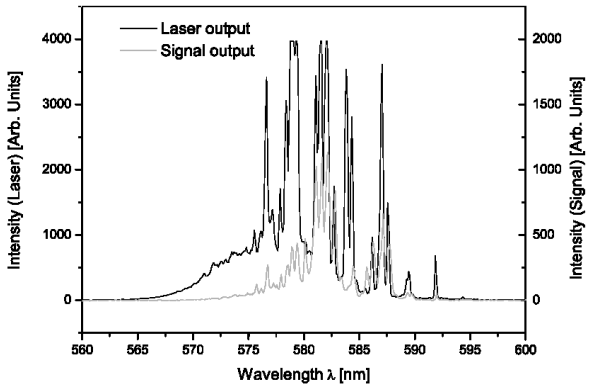

Figure 7.9: The spectra measured at the dye laser output and the signal output from the COC chip.

Figure 7.9 shows two spectra measured from a pumped device. One spectrum shows the light directly coming from the laser and the other spectrum shows the light after travelling through the waveguide and absorption cell and waveguide again. The dissimilarity of the spectra may be caused by a filtering effect experienced by the light travelling through the waveguide and the microfluidic cuvette system.

Although much work was invested into making this chip function according to the design, the functionality remained unproven. This was most likely caused by misfunction of the optical system of lenses and waveguides due to a wrong design. The laser and the microfluidic channels appeared to function as intended. Although the concerted functionality of all the components was not demonstrated, the chip demonstrates the possibility of forming microfluidic, passive optical and laser structures in COC on one chip via imprint lithography.

7.1.3 Hybridization of fluidic dye laser and mini-dispenser

An important part of the operation of a microfluidic laser is the supply of dye fluid. In normal laboratory sized (CW) dye lasers, liters of dye fluid are stored in a container and pumped at high pressure through the laser system. Miniaturization of dye lasers would be incomplete if the dye delivery system remains a large piece of equipment. Therefore a newly developed miniaturized fluid dispenser was adapted for use with the microfluidic lasers [90, 91], in order to demonstrate a possible solution to the delivery of dye fluid[3]. In all other instances presented in this thesis, tabletop syringe pumps have been used.

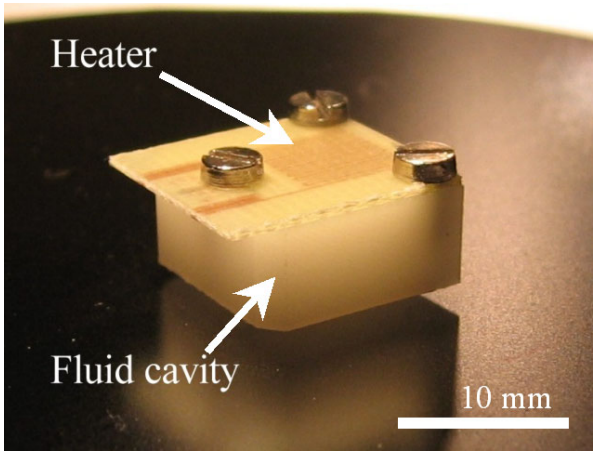

Figure 7.10: Dispenser chamber with a heater integrated in a printed circuit board on top. Electrical connections are on the left. The fluid is dispensed through a hole in the fluid cavity located underneath the cavity and not visible in the photograph. An O-ring is mounted around the hole to seal the connection to the laser chip.

Figure 7.10 shows a photograph of a dispenser. It consists of a chamber for the fluid to be dispensed and a heater. A material that expands upon thermal activation is located between the heater and the fluid. When the heater is heated with an electric current, the material expands and pushes out the fluid at a rate determined by the applied power.

Figure 7.11 shows a drawing of a dispenser mounted on a laser chip. The figure also shows the principle of the dispenser. A membrane (Nitrile) separates the dye

[3]My contribution to this work has consisted in hybridization, characterization and analysis of the measurement results.

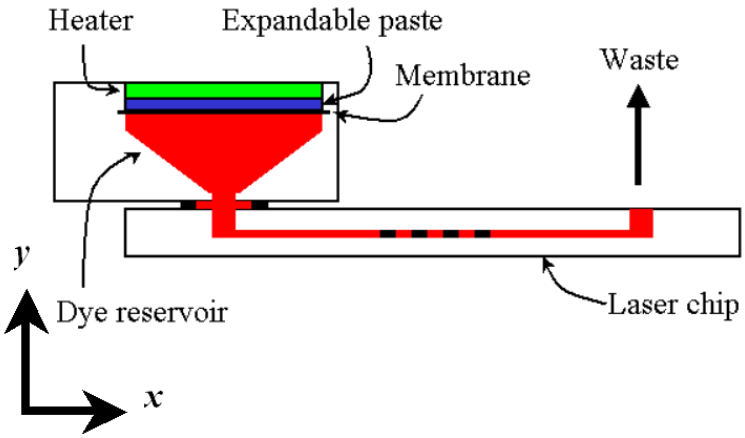

Figure 7.11: Outline of dispenser principle and dye solution flow through the system.

reservoir from the expandable paste. The expandable paste is in contact with the PCB heater.

The liquid dispenser is 14 mm by 15 mm by 8 mm in size (see Figure 7.10). The dispensing action is based on a compound of glycerine and microscopic polymer spheres containing a fluidized hydrocarbon gas (Expancel® 820DU) mixed with glycerine to a concentration of: 0.7 g/mL glycerine. When the compound is heated the polymer spheres expand and the whole compound paste expands into a cavity containing the liquid to be dispensed, this ejects the liquid from the cavity through the outlet hole. The polymer sphere compound and the liquid in the cavity are separated from each other by a thin elastic polymer membrane (Nitrile) in order to avoid contamination of the liquid by the compound (see Figure 7.11). The dispenser cavity holds 100 µL of dye liquid, enough for more than 10 hours of operation of the laser. The flow-rate of the dispenser can be adjusted between 1 µL/hr and 2400 µL/hr by controlling the electrical power delivered to the heater in the dispenser. The current application dictates an operational flow between 1 µL/hr and 10 µL/hr, although a higher flow-rate is used to prime the downstream components at the beginning of operation. The recyclable dispenser lasts for a limited operation time, however the used dispenser can be easily replaced with a newly prepared one.

Figure 7.12 shows the parts mounted together with all channels primed with dye fluid and ready for operation. O-rings seal the fluidic connection between the glass laser chip and the dispenser and the waste and Figure 7.13 shows the volume of fluid dispensed as function of time for a heater power of 301 mW. The fluid was dispensed through the laser chip and the volume was measured using a capillary tube connected to the waste outlet. The small amount of fluid in the dispenser allows for more than 10 hours of continuous operation including preliminary priming of the fluidic system with dye fluid from the reservoir.

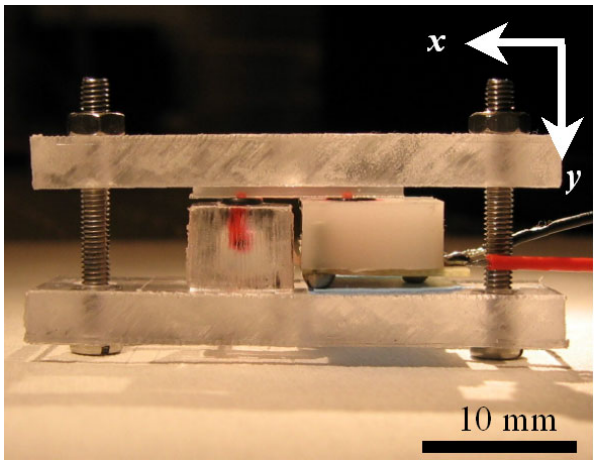

Figure 7.12: Realized assembly after priming of laser with dye and attaching electrical connection to the heater. The left cube underneath the laser is a waste disposal arrangement.

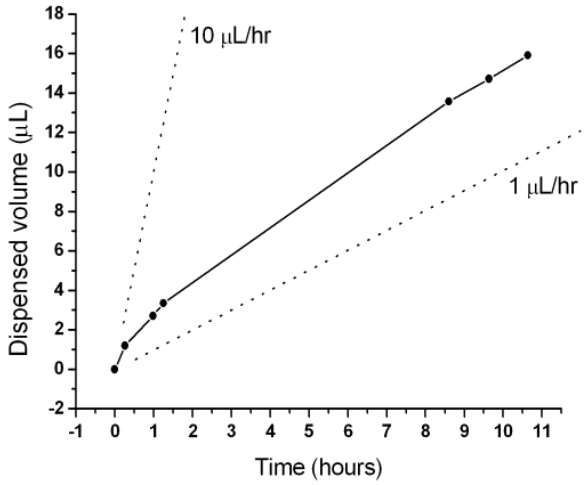

Figure 7.13: Dispensed volume of dye solution through laser at 301 mW heater power, as function of time. The maximum temperature of the liquid dye in the dispenser during actuation was measured to 39.5°C.

7.2 Conclusion

This chapter has shown some of the efforts directed toward demonstrating integration of miniaturized polymer dye lasers into microfluidic circuits. Integrating a microfluidic laser, has the significant advantage that it does not increase the production cost and there are no alignment necessary, that may influence the coupling between the laser and the rest of the polymer components.

It must be mentioned, that since the integrated devices were more complicated, some effort had to be put into characterizing them, which is the cause of the limited measurement data set.

Chapter 8

Alternative resonator types and devices

This chapter describes a couple of laser resonator types that have been investigated during the Ph.D. work in addition to the devices presented in Chapter 6. The lasers are termed "alternative", since they are somewhat secondary to the main goal of the thesis work in the sense that they are probes for development in new directions and not steps directly toward usable lab-on-a-chip lasers. Only the most important details and results are described.

8.1 Triangular mirror lasers

Total internal reflection appears on a SU-8 to air interface for an incidence angle of 45°. A triangle will therefore function as a mirror when light impinges normal to a side of the triangle. A structure with two opposing triangles therefore creates an optical resonator, see Figure 8.1[1].

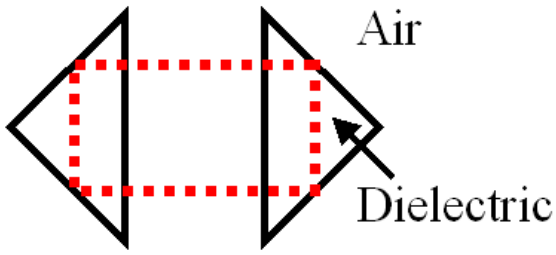

Figure 8.1: Two opposing triangles forming an optical resonator via total internal reflection on the dielectric-to-air interface.

With X-ray lithography, a waveguide terminating in a triangle at both ends were

[1]My contribution to this work on triangular mirror lasers has been complete with respect to the solid state device, and has consisted in design contributions and contributions to analysis of the measurement results for the microfluidic device.

defined in Rhodamine 6G doped SU-8. Figure 8.2 shows an electron microscope image of two waveguides with widths of 3 μm and 8 μm. Lasing was observed

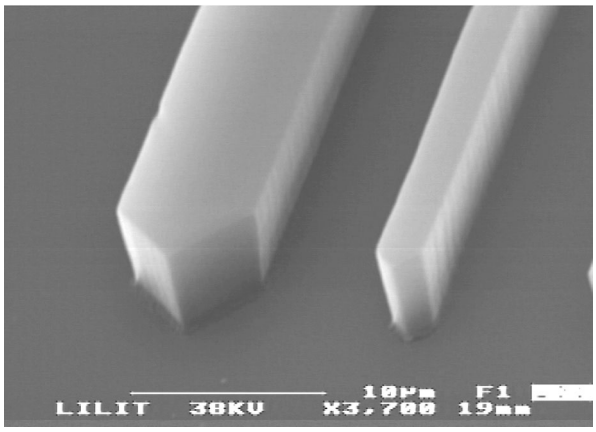

Figure 8.2: Waveguides fabricated with X-ray lithography on dye doped SU-8. The waveguides terminate in a triangle which reflects light back into the waveguide due to total internal reflection.

from 300 μm long and 8 μm wide waveguides. A spectrum and pump curve is illustrated in Figure 8.3. Since there is no specific out-coupling mechanism, the spectrum was measured on scattered light from the devices. The mode spacing

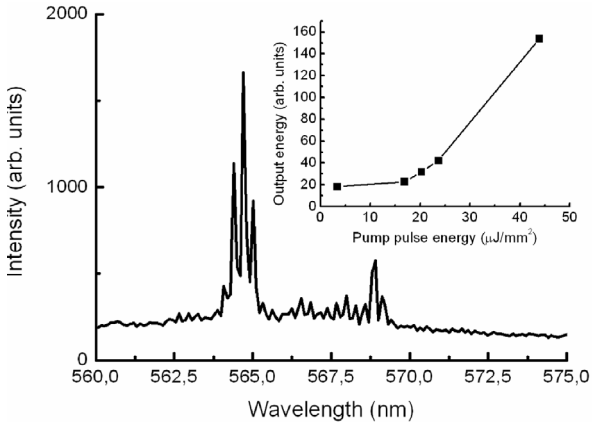

Figure 8.3: Output spectrum from a 300 μm long waveguide terminating in reflecting triangles at both ends. The mode spacing is 0.3 nm. The lasing threshold lies around 20 μJ mm^{-2}.

is 0.3 nm corresponding to a 300 μm long Fabry-Pérot resonator as would be expected. The power reflectance of the mirror was found to 93% by modelling in FEMLAB (see Section 4.1.4).

Another type of laser using triangle reflectors have been investigated. The laser is based on two SU-8 defined triangles separated by a microfluidic channel, the design is illustrated in Figure 8.4.

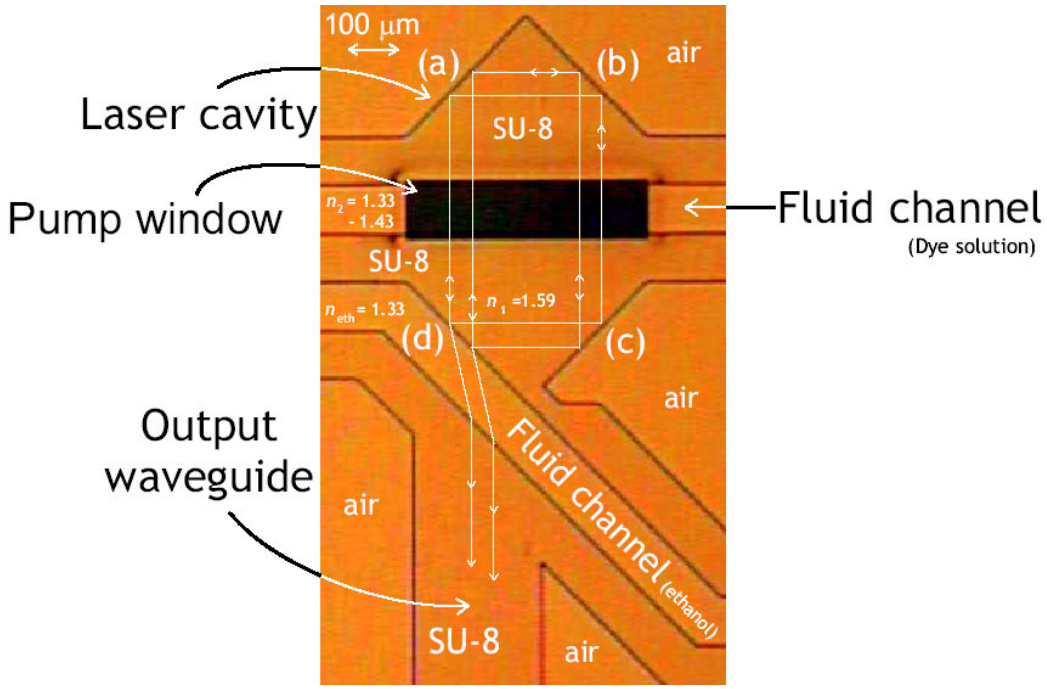

Figure 8.4: Example of integration of a trapezoid laser with a waveguide in undoped SU-8 resist. A microfluidic channel passes in between the two reflecting triangles. A Rhodamine 6G dye solution is injected into the fluid channel during laser operation of the chip.

One of the sides of the SU-8 triangles is wetted with pure ethanol, breaking the total internal reflection and allowing the light to be coupled out through the side into an output waveguide. A solution of Rhodamine 6G dissolved in ethanol was pumped through the microfluidic channel in between the two triangles. A window in a metal mask ensures that only the area between the two triangles is optically pumped.

As for the triangularly terminated waveguide described above, there is no good out-coupling mechanism. The solution of breaking the total internal reflection with ethanol, leads to a low reflectivity of only 5%. The feedback in the triangle resonator thus becomes correspondingly low. It can be speculated that fluids with lower index of refraction could be used to control the out-coupling, however it would be necessary to use a fluid with a refractive index of ∼1.12, which does not exist. High index fluids are another approach, that may be considered. Another solution is to use evanescent field coupling, which is currently being investigated (at the time of writing).

Figure 8.5 shows a series of spectra for increasing pump energy densities, measured on the microfluidic laser using SU-8 triangles for reflectors. Figure 8.6 shows the output as function of pump energy density, which has a slight bend that can be interpreted as the lasing threshold. The spectra are quite broad and contain a mode structure from the resonator. The bend of the pump curve at lasing threshold is not sharp, and the device may operate in a mixture of lasing and ASE. This would be reasonable considering the large round-trip loss, approximately 95%.

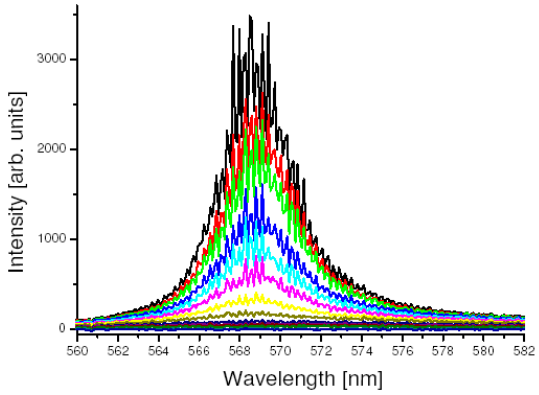

Figure 8.5: Output spectra from the microfluidic laser using triangles to form the resonator. The pump energy densities are in the range 0 μJ mm^{-2} to 120 μJ mm^{-2}.

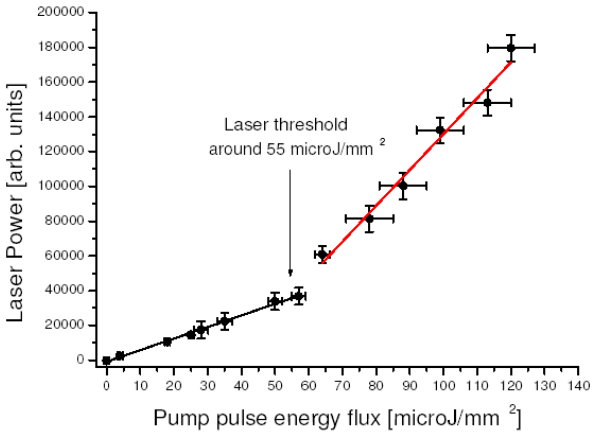

Figure 8.6: Pump curve for the microfluidic triangle laser.

For both the solid state device and the fluid state device, the out-coupling is a problem which must be solved if the laser type using triangular mirrors shall find use in lasers for microsystems.

8.2 Ratchet laser

Laser resonators with circular geometry have been pursued due to the high Q-factors of whispering gallery modes (WGM) and the correspondingly low pump thresholds that may be obtained. However, coupling light out from the resonators presents a challenge, especially for the short wavelengths of visible light. Out-coupling from a ring resonator would typically be obtained by evanescent field coupling or by using a grating. Both methods require exact fabrication of sub-wavelength features.

One method that has been used to control out-coupling of light from WGM type

resonators consists in a deformation of the circular structure [92, 93]. This typically results in multiple output beams, which is not desirable from an efficiency point of view.

Another solution to coupling out light that has been approached, is to apply an asymmetric deformation on the circular geometry. This breaks the symmetry of the clockwise and the anti-clockwise waves propagating in the structure and can lead to unidirectional output from a lasing device [94, 95, 96, 97, 98].

The deformation that has been investigated during this Ph.D. work consists of a spiral shape deformation with a notch (see Figure 8.7)[2]. The radius of the laser ring is determined by equation (8.1). The general conception of the ratchet resonator, is that it is a chaotic resonator due to its shape. If the resonator is chaotic or not, and for which conditions, has not been determined though.

$$r(\phi) = r_0(1 + \frac{\epsilon}{2\pi}\phi) \tag{8.1}$$

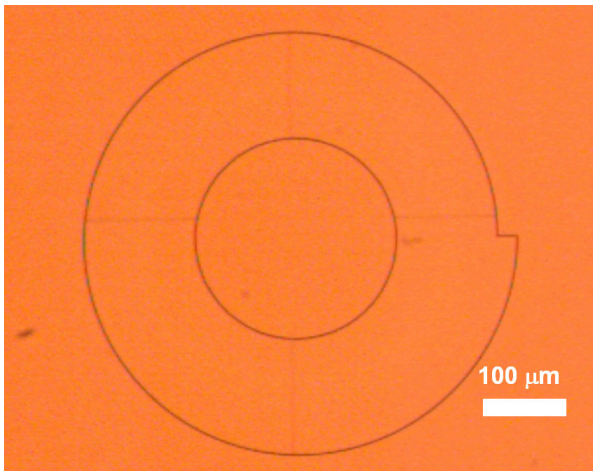

Figure 8.7: Microscope photograph of a ratchet laser structure in SU-8 defined by electron beam lithography.

It is speculated by Chern et al., in [94], that the ratchet geometry has a lower loss for clockwise propagating light than for counter-clockwise propagating light (see Figure 8.8). This makes it possible to achieve unidirectional lasing in the clockwise direction, and the light is coupled out by scattering backwards on the notch. The angular distribution of the emission from a ratchet resonator has been measured by Chern et al. in [99, 94] and they observed a single dominant lobe (see Figure 8.9).

In fabrication, the ratchet lasers are defined in a 770 nm thick film of doped SU-8 photoresist on top of a silicon substrate containing a 2.5 µm of thermally grown silicon dioxide. To define the structures we use 100 keV electron beam lithography, applying a dose of 14 $\mu C/cm^2$ on the negative resist. The resist has been doped with 0.14% mass Rhodamine 6G perchlorate.

[2]My contribution to the work on ratchet lasers has been complete.

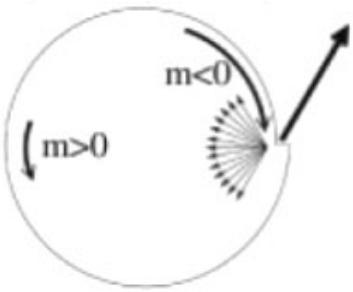

Figure 8.8: The two counter propagating set of modes in the ring experience different losses. Clockwise modes are denoted by a negative mode number, m, and counter-clockwise propagating modes by positive mode number m. The clockwise modes are scattered on the notch and some of the energy is coupled out (reproduced from [94]).

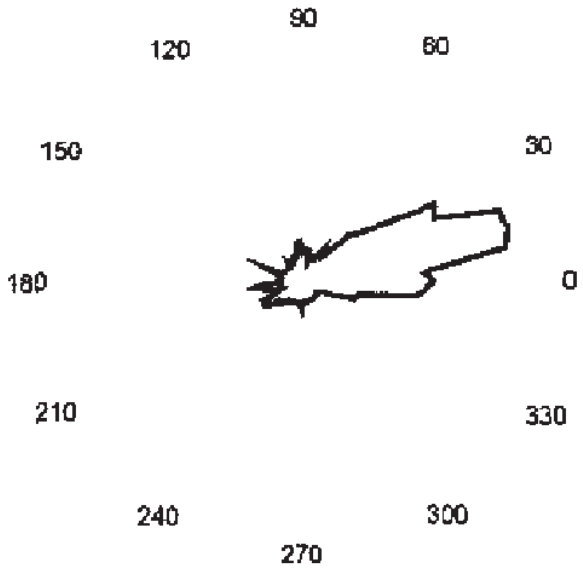

Figure 8.9: Emission pattern measured from a semiconductor ratchet laser device (r_0=145 μm and $\epsilon = 0.1$). The numbers denote the angle ϕ in equation (8.1) and the curve the angular distribution of the light intensity (reproduced from [99]).

During optical characterization, the polymer dye lasers were optically pumped by the frequency doubled Nd:YAG laser. Figure 8.10 shows a microscope photograph of a lasing ratchet resonator. The emitted light from the ratchet resonators was picked up by a multimode fiber with a core diameter of 200 μm and directed to the solid state spectrometer. The fiber collecting the light was positioned at an angle 45 degrees to normal and 45 degrees relative to the notch on the ratchet lasers.

The output spectra picked up from the notch of these devices showed an interesting feature (Figure 8.11). The spectra showed bunches of modes with an intra mode spacing of 0.3 nm, corresponding to the round-trip around the resonator, 786 μm. The lasing threshold was 4 μJ mm^{-2}. The appearance of bunches was present in several lasers with similar design parameters. These modes appearing in bunches

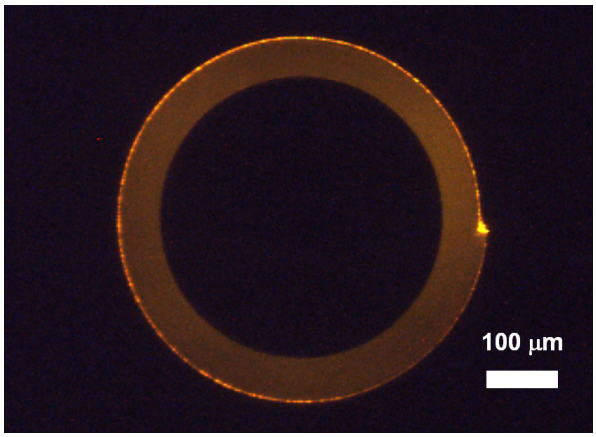

Figure 8.10: Microscope photograph of a lasing ratchet device. Light is emitted at the notch and partly scattered vertically into the microscope. The light from the notch has saturated the CCD camera.

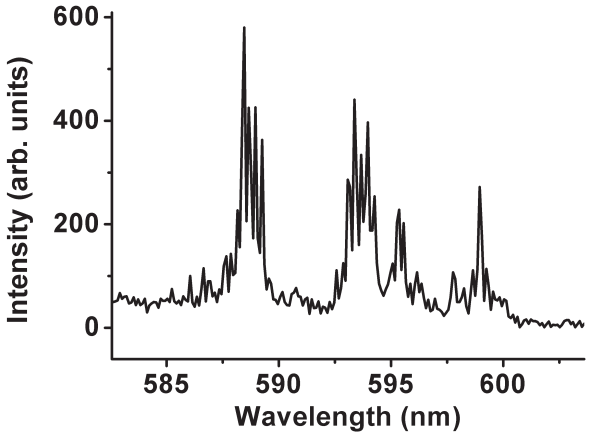

Figure 8.11: Output spectrum from ratchet laser with a radius of 125 μm and no center hole, the notch is defined by $\epsilon = 0.01$. The lasing threshold for the device is 4 μJ mm^{-2}.

does not seem to be immediately explainable. Modelling efforts have not yielded conclusive results yet.

In conclusion, it is possible by using EBL on dye doped SU-8 to quickly prototype new resonator structures. Although the ratchet resonator functionality is intriguing, ratchet resonator devices in SU-8 lase in multiple modes. The lasing threshold was low and further work on this kind of device could lead to single mode operation by defining frequency selective structures on the ring, such as a grating.

8.3 ASE device with vertical output

Machines for UV lithography and EBL are constructed for normal incidence of the radiation on the substrate. Normal incidence is advantageous with respect to

uniformity of the exposure, but it principally entails vertical sidewalls. Sloping sidewalls are possible via grey scale lithography, but this method relies on the properties of the resist which are in general not constant at varying exposure doses. In addition it is not possible to fabricate negative sidewall slopes with grey scale lithography.

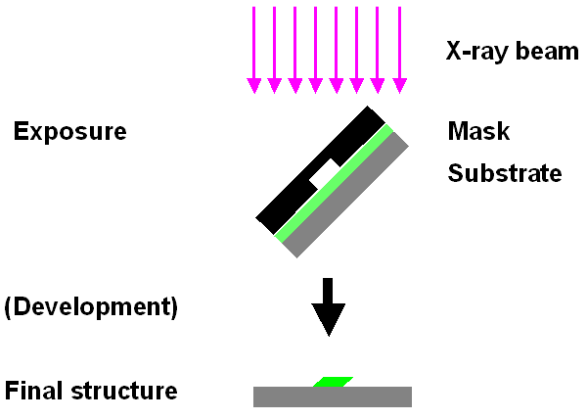

Figure 8.12: Principle of angled lithography with X-rays.

Sloping sidewalls can be obtained by tilting the substrate under exposure with respect to the exposure radiation source (see Section 5.1.3). X-rays from the ELETTRA synchrotron beam-line LILIT have good collimation with an angular distribution less than ± 1 mrad, and it is therefore easy to perform good quality exposures on tilted substrates [100]. This makes it possible to fabricate structures in the resist with well-defined tilted sidewalls. In particular, it is noteworthy that with this technique sidewalls with negative slope can be fabricated with very good corner definition due to the high resolution of the lithographic method. Defining a negative slope of 45° at the end of a waveguide, results in total internal reflection of light travelling in the waveguide (for SU-8) as illustrated in Figure 8.13. Thereby the light is coupled out vertically. This is the principle exploited in the ASE device in this section[3]. ASE is generated in a length of waveguide under optical pumping, and the light is coupled out at the end of the waveguide with negative slope. An ASE device is an alternative to a laser device if coherence and narrow spectral line-width are not necessary.

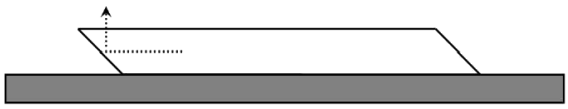

Figure 8.13: Light travelling down a waveguide terminated with a negative slope is coupled out vertically due to total internal reflection on the sloping sidewall.

The result of an exposure on a (45°) tilted substrate can be seen in Figure 5.19. The pattern is 5 µm thick and consists of waveguides of varying width (in µm: 0.5,

[3]My contribution to this work on ASE devices has been entire.

1, 3 and 8) and length (in μm: 18.75, 37.5, 75, 150 and 300). Figure 8.14 shows a microscope photograph of the array of waveguides pumped with the Nd:YAG laser. Only the waveguides with widths of 3 and 8 μm show significant output. The contrast of the photograph has been decreased to make it possible to see both the vertically out-coupled light and the fluorescence from the waveguides.

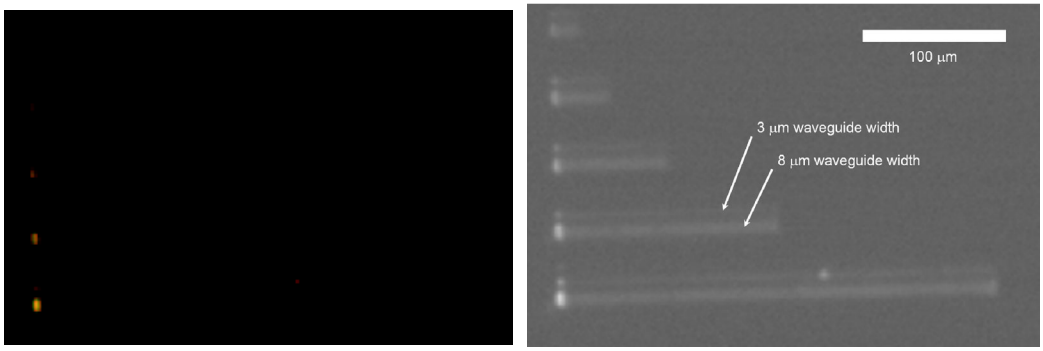

Figure 8.14: Microscope fluorescence photograph of waveguides with sloping end sidewalls, being pumped with 532 nm (filtered away in microscope). Left: Original photograph. Right: The contrast of the picture has been adjusted to allow seeing both fluorescence from the waveguides and the light coupled out of the ends at the same time.

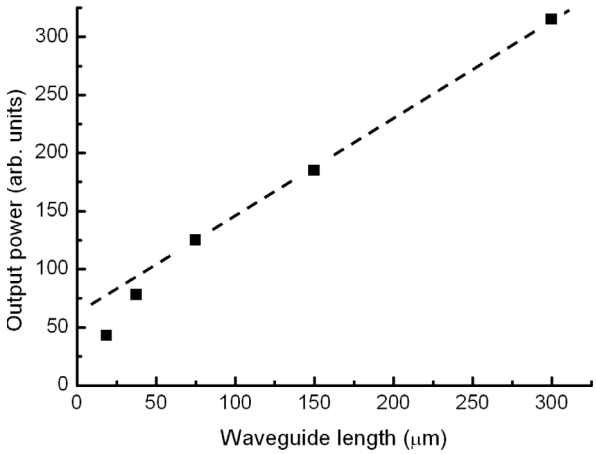

Figure 8.15: Amount of light coupled out from the ends of the ASE waveguide structures as function of waveguide length.

Figure 8.15 shows the power coupled out vertically from the end of the 8 μm wide waveguides as function of waveguide length – the data was extracted from the photograph in Figure 8.14. It is observed from the figure that the plot points for waveguides lengths longer than 75 μm lie on a straight line that does not intersect with the origin of the coordinate system. The fact that the output from the three longest waveguides lie on a line that does not go through the origin of the graph indicates that the light is generated by ASE. Pure fluorescence would lie on a line going through the origin of the graph, assuming that the optical loss along the short waveguide was negligible. In contrast, ASE needs to propagate a distance

to build up. So for waveguides longer than about 75 μm, ASE is dominant. The linear relationship arises due to saturation of the gain in the ASE process[101].

8.4 Conclusion

This chapter has been concerned with some alternative miniaturized polymer dye lasers and ASE sources that are not ready for integration into LOC systems "as is". Investigations are continuing (at the time of writing) on the microfluidic triangle based laser and the ratchet laser. It should be apparent from the chapter that there are many possibilities for defining lasers in polymer.

Chapter 9

Concluding remarks

Several laser architectures have been demonstrated through the work covered in this thesis. The main objective of the work was to develop lasers that could be used for LOC circuits, however there are some issues that need to be addressed: Most importantly, since the lasers need to be optically pumped, any real-life apparatus will need to contain a flash lamp (or a laser) and a flash lamp driver. Whether the benefits from using an on-chip laser outweighs the inconvenience of an optical pump, is entirely application specific. Parameters such as if the application requires disposable chips or if it requires widely tunable laser light, will influence the "cost/benefit" analysis. The research area of LOC has not yet settled into widespread commercialization, and which types of applications that will precipitate from research is as yet unknown.

Another concern is the dye supply to the lasers. The solid state lasers have a limited lifetime, therefore laser devices that need to operate for times exceeding the solid state lifetime has to be based on a fluid solution of laser dye. As anyone will concede, who has worked with lasers based on fluid laser dye solutions, liquid dye is a mess. Therefore the benefits need to be weighed with the inconveniences also with regard to using microfluidic miniaturized dye lasers – here it must be remembered though that the amount of dye consumed by the lasers is minuscule ($\lesssim$1 μL hr^{-1}).

Although the devices in this thesis has focused on integration with LOC systems, this does not limit the applicability of the laser devices to that area. One alternative application that may become interesting, is using a microchip to form a laser and pulse shaping elements in order to generate pico-second pulses (or less). Oki et al. have demonstrated a solid state device operating with this principle [102].

Another example of further developments is to form a set of twin lasers and control the wavelengths, for example via the local temperature. Combining the light signal from the two lasers will form a beating intensity, the frequency of which will depend on the wavelength difference and thereby the local surroundings of the lasers, which could be used for sensing purposes.

At the time of writing several projects at MIC are building on experience in part developed through the work presented in this thesis.

Bibliography

[1] DARPA Center for Optofluidic Integration, California Institute of Technology.

[2] J. Hübner, K. B. Mogensen, A. M. Jorgensen, P. Friis, P. Telleman and J. P. Kutter, "Integrated optical measurement system for fluorescence spectroscopy in microfluidic channel", *Review of Scientific Instruments*, 2001, **72**, 229

[3] K. B. Mogensen, J. El-Ali, A. Wolff and J. P. Kutter,"Integration of polymer waveguides for optical detection in microfabricted chemical analysis systems", *Appl. Opt.*, 2003, **89**(19), 4072

[4] H. Lorenz, M. Despont, N. Fahrni, N. LaBianca, P. Renaudy and P. Vettiger, "SU-8: a low-cost negative resist for MEMS", *J. Micromech. Microeng*, 1997, **7**, 121

[5] L. Eldada, K. M. T. Stengel, L. W. Shacklette, R. A. Norwood, C. Xu, C. Wu and J. Yardley, "Advanced polymer systems for optoelectronic integrated circuit applications", Optoelectronic Integrated Circuits, Y. S. Park and R. V. Ramaswamy, eds., *Proc. SPIE*, 1997, **3006**, 344

[6] B. Bilenberg, M. Hansen, D. Johansen, V.Özkapici, C. Jeppesen, P. Szabo, I. M. Obieta, O.Arroyo, J. O.Tegendfeldt, and A. Kristensen "Topas Based Lab-on-a-chip Microsystems Fabricated by Thermal Nanoimprint Lithography", Journal of Vacuum Science and Technolgy B, Vol. 23, pp. 2944-2949 (2005)

[7] A. Manz, N. Graber and H. M. Widmer, "Miniaturized total chemical analysis systems: a novel concept for chemical sensing", *Sens. Actuators B*, 1990, **1**, 244-248

[8] Chia-Yen Lee; Jr-Lung Lin; Chia-Sheng Liao; Fu-Chun Huang; Gwo-Bin Lee, "Integrated Microfluidic Systems for DNA Analysis", Conference on Robotics and Biomimetics, 2004. ROBIO 2004. IEEE International. Proceedings pp. 284-289

[9] B. Helbo, A. Kristensen, and A. Menon, "A Micro-Cavity Fluidic Dye Laser", Journal of Micromechanics and Microengineering, vol. 13, Issue 2, pp. 307-311 (2003)

[10] S. Kragh, M. Sc. thesis, "A Solid State Micro Cavity Dye Laser", MIC, Technical University of Denmark (DTU), 2003

[11] B. Bilenberg, T. Nielsen, B. Clausen, and A. Kristensen, "PMMA to SU-8 bonding for polymer based lab-on-a-chip systems with integrated optics", Journal of Micromechanics and Microengineering, vol.14, pp. 814-818 (2004)

[12] T. H. Maiman, "Stimulated optical radiation in ruby", Nature vol 187, pp. 493-494, 1960

[13] P. P. Sorokin, J. R. Lankard, "Stimulated emission observed from an organic dye, chloro-aluminium phthalocyanine", IBM Journal of Research and Development, vol. 10 No. 2, pp. 162-163, 1966

[14] P. P. Sorokin, J. R. Lankard, "Flashlamp excitation of organic dye lasers. A short communication.", IBM Journal of Research and Development, vol. 11, p. 148, 1967

[15] B. H. Soffer, B. B. McFarland, "Continuously tunable, narrow-band organic dye lasers", Appl. Phys. Letters, vol. 10, p. 266, 1967

[16] O. G. Peterson, B. B. Snavely, "Experimental measurement of the critical population inversion for the dye solution laser" Appl. Phys. Letters, vol. 12, No. 7, pp. 238-240, 1968

[17] C. Hu, S. Kim, "Thin-film dye laser with etched cavity", Appl. Phys. Lett., Vol. 29, No. 9, pp. 582-585, 1976

[18] M. Sasaki, Y. Li, Y. Akatu, T. Fujii, K. Hane, "Anisotropically etched Si mold for solid polymer dye microcavity laser", Jpn. J. Appl. Phys, Vol. 39, pp. 7145-7149, 2000

[19] Y. Li, M. Sasaki, K. Hane, "Fabrication and testing of solid polymer dye microcavity lasers based on PMMA micromolding", Journal of Micromechanics and Microengineering, Vol. 11, No. 3, pp. 234-238, 2001

[20] H. Kogelnik, C. V. Shank, "Stimulated emission in a periodic structure", Appl. Phys. Lett. Vol. 18, No. 4, pp. 152-154, 1971

[21] C. V. Shank, J. E. Bjorkholm, H. Kogelnik, "Tunable distributed-feedback dye laser", Appl. Phys. Lett., Vol. 18, No. 9, pp. 396-396, 1971

[22] S. L. McCall and P. M. Platzman,"An optimized pi/2 distributed feedback laser", IEEE J. Quantum Electron. **21**, 1899 (1985)

[23] H. Kogelnik, "Coupled Wave Theory for Thick Hologram Gratings", The Bell System Technical Journal, vol 48 nr. 9, pp. 2909-2947, 1969

[24] H. Kogelnik and C. V. Shank, "Coupled-Wave theory of Distributed feedback lasers", J. Appl. Phys., vol 43, nr 5, 1972

[25] S. Balslev, T. Rasmussen, P.Shi, and A. Kristensen, "Single mode solid state distributed feedback dye laser fabricated by grey scale electron beam lithography on dye doped SU-8 resist", Journal of Micromechanics and Microengineering, Vol. 15, pp. 2456-2460, 2005

[26] K. Y. Lee, N. LaBianca, S. A. Rishton, S. Zolgharnain, J. D. Gelorme, J. Shaw, and T. H.-P. Chang, Micromachining applications of a high resolution ultrathick photoresist, J. Vac. Sci. Technol. B 13, 3012-3016, 1995

[27] MicroChem Corp., Newton, Massachusetts, USA. www.microchem.com

[28] Microchem Corp. technical data sheet on SU-8, available at http://www.microchem.com

[29] K. B. Mogensen, Ja. El-Ali, A. Wolff, and J. P. Kutter, "Integration of polymer waveguides for optical detection in microfabricated chemical analysis systems", Applied Optics Vol. 42, No. 19, pp 4072-4079, July 2003

[30] B. Bilenberg, T. Nielsen, B. Clausen and A. Kristensen, "PMMA to SU-8 bonding for polymer based lab-on-a-chip systems with integrated optics", J. Micromech. Microeng. Vol. 14, pp. 814818, 2004

[31] K. K. Tung, W.H. Wong, E. Y. B. Pun, "Polymeric optical waveguides using direct ultraviolet photolithography process", Appl. Phys. A 80, pp. 621626, 2005

[32] T. C. Sum, A. A. Bettiol, J. A. van Kan, F. Watt, E. Y. B. Pun, K. K. Tung, "Proton beam writing of low-loss polymer optical waveguides", Appl. Phys. Lett., Vol. 83, No. 9, pp. 1707 to 1709, 2003

[33] B. Y. Shew, C. H. Kuo, Y. C. Huang, Y. H. Tsai, "UV-LIGA interferometer biosensor based on the SU-8 optical waveguide", Proceedings of Sensors and Actuators A 120 pp. 383389, 2005

[34] A. Borreman, S. Musa, A.A.M. Kok, M. B. J. Diemeer and A. Driessen, "Fabrication of Polymeric Multimode Waveguides and Devices in SU-8 Photoresist Using Selective Polymerization" Proceedings Symposium IEEE/LEOS Benelux Chapter, 2002, Amsterdam

[35] L. J. Guo, "Recent progress in nanoimprint technology and its applications", Journal of Applied Physics, 37:123141, 2004

[36] D. Heukelbach, Medical Plastics Conference, Copenhagen, 2003

[37] http://www.pofto.com/downloads/WP-TIA-POFTO.pdf

[38] D. M. Johansen, M. Sc. thesis, "Investigation of Topas for use in optical components", MIC, Technical University of Denmark (DTU), 2005

[39] G. Khanarian, H. Celanese, "Optical properties of cyclic olefin copolymers", Optical Engineering, Vol. 40, No. 6, pp. 1024-1029, 2001

[40] F. P. Schäfer, "Dye Lasers" (Springer Verlag, 1973)

[41] B. H. Bransden, C. J. Joachain, "Physics of atoms and molecules", Longman Scientific and Technical, 1994

[42] http://www.iom-berlin.de/pdfs/Farbstofftabelle.pdf

[43] O. Svelto, "Principles of lasers", Plenum Press, New York, fourth edition, 1998

[44] PhotochemCAD (H. Du, R. A. Fuh, J. Li, A. Corkan, J. S. Lindsey, "PhotochemCAD: A computer-aided design and research tool in photochemistry," Photochemistry and Photobiology, 68, 141-142, 1998)

[45] PhotochemCAD

(http://omlc.ogi.edu/spectra/PhotochemCAD/ems_txt/rhodamine6G.ems.txt)

[46] http://www.technology.niagarac.on.ca/staff/mcsele/lasers/LasersFLP.htm

[47] F. Aussenegg, J. Schubert, "Fast rise air spark pump for organic dye lasers", Physics Letters, vol. 30A, no. 9, pp. 488-489, 1969

[48] D. Nilsson, T. Nielsen, and A. Kristensen "Solid State Micro-cavity Dye Lasers Fabricated by Nanoimprint Lithography", Review of Scientific Instruments vol. 75, pp. 4481-4486, 2004

[49] F. López Arbeloa, P. Ruiz Ojeda, and I. López Arbeloa. "The fluorescence quenching mechanisms of rhodamine 6g in concentrated ethanolic solution", J. Photochem. Photobiol. A, 45(3), pp. 313-323, 1988

[50] E. Hecht, "Optics", Addison-Wesley Publishing Company, Reading, second edition, 1987

[51] http://en.wikipedia.org/wiki/Waveguide

[52] R. G, Hunsperger, "Integrated Optics: Theory and Technology", Third edition, Springer Series in Optical Sciences, Springer-Verlag, 1991

[53] F. M. White "Viscous Fluid Flow", McGraw-Hill Book Company, 1974

[54] A. Yariv, "Coupled-Mode Theory for Guided-Wave Optics", Journal of Quantum Electronics, vol. QE-9, No. 9, pp. 919-933, 1973

[55] J. Hübner, Ph.D. thesis, MIC, Technical University of Denmark (DTU), 1998

[56] L. A. Coldren and S. W. Corzine, "Diode Lasers and Photonic Integrated Circuits", Wiley, New York (1995)

[57] G. Strang and G. J. Fix, "An Analysis of the Finite Element Method", Prentice Hall 1973

[58] F. L. Pedrotti, L. S. Pedrotti, "Introduction to optics", second edition, Prentice Hall, 1987

[59] http://www.okotech.com/software/lightpipes/

[60] http://www.freebpm.com/

[61] H. J. W. M. Hoekstra, G. J. M. Krijnen, P. V. Lambeck, "Efficient Interface Conditions for the Finite Difference Beam Propagation Method", Journal of Lightwave Technology, Vol. 10, No. 10, 1992

[62] D. Yevick, B. Hermansson, "Efficient Beam Propagation Techniques", IEEE Journal of Quantum Electronics, Vol. 26, No. 1, 1990

[63] Y. Chung, N. Dagli, "An Assessment of Finite Difference Beam Propagation Method", IEEE Journal of Quantum Electronics, Vol. 26, No. 8, 1990

[64] http://wn7.enseeiht.fr/hmf/travaux/CD0001/travaux/optmfn/hi/01pa/hyb74/node24.html

[65] M. Koshiba, Y. Tsuji, "Finite Element Beam Propagation Method with Perfectly Matched Layer Boundary Conditions", IEEE Transactions on Magnetics, Vol. 35, No. 3, pp. 1482-1485, 1999

[66] D. Jimenez, F. Perez-Murano, " Implementation of Berenger layers as boundary conditions for the beam propagation method: applications to integrated waveguides", Optics Communications, Vol. 159, No. 1-3, pp. 43-48, 1999

[67] S. Blit, U. Ganiel, "Distribution of absorbed pump power in flashlamp-pumped dye lasers", Optical and Quantum Electronics, vol. 7, pp. 87-93, 1975

[68] http://www.geocities.com/guerinlj/

[69] http://www.elettra.trieste.it/index.php

[70] S. Balslev, F. Romanato, "Fuctionalized SU-8 patterned with x-ray lithography", J. Vac. Sci. Technol B 23(6), pp. 2910-2913, 2005

[71] D. Nilsson, S. Balslev , and A. Kristensen "A microfluidic dye laser fabricated by nanoimprint lithography in a highly transparent and chemically resistant cyclo-olefin copolymer (COC)" Journal of Micromechanics and Microengineering Vol. 15, pp. 296-300, 2005

[72] M. B. Christiansen, "Quantum Dot Based Light Sources for Lab-on-a-chip", M. Sc. thesis, MIC, Technical University of Denmark (DTU), 2005

[73] B. Bilenberg, T. Rasmussen, S. Balslev, A. Kristensen "Real-time tunability of chip-based light source enabled by micro-fluidic mixing", Journal of Applied Physics, Vol. 99, 023102, 2006

[74] D. Nilsson, S. Balslev, M. M. Gregersen, and A. Kristensen "Micro-fabricated solid state dye lasers based on a photo-definable polymer", Applied Optics, Vol. 44, pp. 4965-4971, 2005

[75] S. Balslev and A. Kristensen "Microfluidic Single Mode Laser Using High Order Bragg Grating and Antiguiding Segments", Opt. Express, Vol. 13, 344-351, 2005

[76] D. Nilsson, S. Balslev , and A. Kristensen "A microfluidic dye laser fabricated by nanoimprint lithography in a highly transparent and chemically resistant cyclo-olefin copolymer (COC)", Journal of Micromechanics and Microengineering Vol. 15, pp. 296-300, 2005

[77] S. Balslev, A. Mironov, D. Nilsson, A. Kristensen, "Micro-fabricated single mode polymer dye laser" - submitted for publication.

[78] D. J. M. Stothard, I. D. Lindsay and M. H. Dunn, "Continuous-wave pump-enhanced optical parametric oscillator with ring resonator for wide and continuous tuning of single-frequency radiation", Optics Express, Vol. 12, No. 3, p. 502, 2004

[79] E. D. Palik, "Handbook of Optical Constants of Solids", Academic Press, 1998

[80] M. A. Ali, J. Moghaddasi, S .A. Ahmed, "Optical properties of cooled rhodamine B in ethanol", J. Opt. Soc. Am. B. Vol. 8, 1991

[81] Kragh and A. Kristensen, "Miniaturized solid state lasers based on a photodefinable polymer", Proc. Eurosensors 2003, 2003

[82] A. W. Poon, F. Courvoisier, R. K. Chang, "Multimode resonances in square-shaped optical microcavities", Optics Letters, Vol. 26, No. 9, 2001

[83] F. Laerner, S. Schilp of Robert Bosch GmbH US-Patent No. 5501893

[84] *CRC Handbook og Chemistry and Physics* 1987 67th ed. CRC Press Boca Raton FL USA

[85] Y. Oki, T. Yoshiura, Y. Chisaki, M. Maeda, "Fabrication of a distributed-feedback dye laser with a grating structure in its plastic waveguide", Applied optics, Vol. 41, No. 24, 2002

[86] P. Friis, K. hoppe, O. Leistiko, K. B. Mogensen, J. Hbner and J. p. Kutter, *Appl. Opt.*, 2001, **40**, 6246

[87] T. T. Veenstra, T. S. J. Lammerink, M. C. Elwenspoek and A. van den Berg, *J. Micromech. Microeng.* , 1999, **9**, 199

[88] B. R. Clemesha, *Journal of Physics E*, 1972, **5**, 859

[89] C. Gay, J. Collins and J. M. Gebicki, *Analytical Biochemistry*, 1999, **273**(2), 143

[90] N. Roxhed et al., Proceedings of 17th IEEE International Conference on Micro Electro Mechanical Systems (MEMS), pp. 326-329, 2004

[91] S. Balslev, N. Roxhed, P. Griss, G. Stemme, and A. Kristensen "Microfluidic dye laser with compact, low-cost liquid dye dispenser" Proceedings of Micro-TAS 2004, the eigth international Conference on Miniaturised Systems for Chemistry and Life Sciences, Malm, Sweden, 26-30 September 2004, T. Laurell, J. Nilsson, K. Jensen, D.J. Harrison and J.P. Kutter eds., Royal Society of Chemistry, Cambridge, United Kingdom (2004), Vol. 2, pp. 375-377.

[92] C. Gmachl, F. Capasso, E. E. Narimanov, J. U. Nöckel, A. D. Stone, J. Faist, D. L. Sivco, A. Y. Cho, "High-Power Directional Emission from Microlasers with Chaotic Resonators", Science, Vol. 208, pp. 1556-1564, 1998

[93] M. S. Kurdoglyan, S-Y Lee, S. Rim, C-M Kim, "Unidirectional lasing from a microcavity with a rounded esosceles triangle shape", Optics Letters, Vol. 29, No. 24, 2004

[94] G. D. Chern, H. E. Tureci, A. D. Stone, R. K. Chang, M. Kneissl, N. M. Johnson, "Unidierctional lasing from InGaN muliple-quantum-well spiral-shaped micropillars", Applied Optics Letters, Vol. 83, No. 9, pp. 1710-1712, 2003

[95] M. Kneissl, M. Teepe, N. Miyashita, N. M. Johnson, G. D. Chern, R. K. Chang, "Current-injection spiral-shaped microcavity disk laser diodes with unidirectional emission", Applied Physics Letters, Vol 84, No. 14, pp. 2485-2487, 2004

[96] S-Y Lee, S. Rim, J-W Ryu, T-Y Kwon, M. Choi, C-M Kim, "Quasiscarred Resonances in a Spiral-Shaped Microcavity", Physical Review Letters, Vol. 93, No. 16, pp. 164102-1 – 164102-4, 2004

[97] F. Courvoisier, V. Boutou, J. P. Wolf, R. K. Chang, J. Zyss, "Deciphering output coupling mechanisms in spiral microcavities with femtosecond light bullets", Optics Letters, Vol. 30, No. 7, pp. 738-740, 2005

[98] T. Ben-Messaoud, J. Zyss, "Unidirectional laser emission from polymer-based spiral microdisks", Applied Physics Letters, Vol 86, pp. 241110-1 – 241110-3, 2005

[99] G. D. Chern, A. W. Poon, R. K. Chang, S-Y Kuo, T. B. Messaoud, O. Alloschery, E. Toussaere, J. Zyss, "Directional Laser Emission from Square, Spiral and Mismatched Semi-Circular Dye-Doped Polymer Based Miropillar Cavities", Proceedings QELS, QMG4 p. 25, 2002

[100] F. Romanato, E. Di Fabrizio, L. Vaccari, M. Altissimo, D. Cojoc, L. Businaro, S. Cabrini, "LILIT beamline for soft and deep X-ray lithography at Elettra" Microelectronic Engineering 5758, pp. 101107, 2001

[101] T. Mappes, S. Achenbach, A. Last, J. Mohr and R. Truckenmller, "Evaluation of optical qualities of a LIGA-spectrometer in SU-8", Microsystem Technologies vol 10, p. 560, 2004

[102] Y. Oki, K. Ohno, M. Maeda, "Tunable Ultrashort Pulse Generation from a Waveguided Laser with Premixed-Dye-Doped Plastic Film", Jpn. J. Appl. Phys, Vol. 37, pp. 6403-6407, 1998

Appendix A

Publication list of papers published in peer reviewed journals

- S. Balslev and A. Kristensen "Microfluidic Single Mode Laser Using High Order Bragg Grating and Antiguiding Segments", Opt. Express, Vol. 13, 344-351 (2005)

- D. Nilsson, S. Balslev , and A. Kristensen "A microfluidic dye laser fabricated by nanoimprint lithography in a highly transparent and chemically resistant cyclo-olefin copolymer (COC)", Journal of Micromechanics and Microengineering Vol. 15, pp. 296-300 (2005)

- M. Gersborg-Hansen, S. Balslev, N. A. Mortensen, and A. Kristensen "A coupled cavity micro fluidic dye ring laser", Microelectronic Engineering, Vol. 78-79, pp. 185-189 (2005)

- D. Nilsson, S. Balslev, M. M. Gregersen, and A. Kristensen "Micro-fabricated solid state dye lasers based on a photo-definable polymer", Applied Optics, Vol. 44, pp. 4965-4971 (2005)

- S. Balslev and F. Romanato "Functionalized SU-8 patterned with X-ray Lithography", Journal of Vacuum Science and Technology B, Vol. 23, pp. 2963-2966 (2005)

- S. Balslev, T. Rasmussen, P.Shi, and A. Kristensen "Single mode solid state distributed feedback dye laser fabricated by grey scale electron beam lithography on dye doped SU-8 resist", Journal of Micromechanics and Microengineering, Vol. 15, pp. 2456-2460 (2005)

- M. Gersborg-Hansen, S. Balslev, and N. A. Mortensen "Finite-element simulation of cavity modes in a micro-fluidic dye ring laser", J. Opt. A: Pure Appl. Opt. 8, 17 (2006)

- B. Bilenberg, T. Rasmussen, S. Balslev, and A. Kristensen "Real-time tunability of chip-based light source enabled by micro-fluidic mixing", Journal of Applied Physics, Vol. 99, 023102 (2006)

- S. Balslev, A. M. Jorgensen, B. Bilenberg, K. B. Mogensen, D. Snakenborg, O. Geschke, J. P. Kutter, and A. Kristensen "Lab-on-a-chip with integrated optical transducers", Lab on a Chip, accepted for publication (2006)